Breaking for 2D and 3D gravity wave groups in deep and transitional water

Arvin Saket

A thesis in fulfilment of the requirements for the degree of

Doctor of Philosophy

School of Civil and Environmental Engineering

Faculty of Engineering

UNSW Sydney

April 2017

THE UNIVERSITY OF NEW SOUTH WALES

Thesis/Dissertation Sheet

Surname: SAKET

First name: ARVIN Other names:

Abbreviation for degree as given in the University calendar: PhD

School: Civil and Environmental Engineering Faculty: Engineering

Title: Breaking for 2D and 3D gravity wave groups in deep and transitional water

Abstract 350 words maximum

Water wave breaking is a dominant dynamical process of the upper ocean, inducing strong flow-turbulence-wave interactions and air-sea exchanges. A fundamental and long-standing gap in the understanding of wave breaking is how to characterise and predict the onset of breaking.

The threshold for the onset of breaking proposed by Barthelemy *et al*. (arXiv:1508.06002v1, 2015) has been investigated intensively in the laboratory for different classes of two- and three-dimensional wave groups in deep and transitional water in the absence and presence of wind. Thermal Image Velocimetry was used to compare measurements of the wave crest surface water particle velocity with the wave crest speed determined by an array of closely-spaced wave gauges.

For the first time, a threshold crest point surface energy flux ratio (B_x) that distinguishes maximum group recurrence from marginal group breaking has been established for gravity waves. The critical value of B_x was found to be 0.835 ± 0.005 with an experimental uncertainty of each data point of ±0.020. The breaking threshold is robust for different types of unidirectional and directional wave groups. Very weak dependence on wind forcing and group bandwidth is demonstrated. No dependence on relative water depth was observed. If there is a dependence on peak spectral wavenumber, it is weak and negligible for the scales achievable in a large-scale laboratory.

This study provides more robust and universal characterisation of breaking in transitional water than the empirical non-dimensionalisation of Nelson (1994). The effect of wave grouping can generate marginally breaking waves in shallower water that are at least 30 % greater than the limit proposed by Nelson. The study supports use of a limit at least that recommended by McCowan (1894)/Miche (1944) for coastal engineering design in transitional and shallow water until it is demonstrated that there is negligible risk of strongly breaking group waves achieving higher breaker indices.

ORIGINALITY STATEMENT

I hereby declare that this submission is my own work and to the best of my knowledge it contains no materials previously published or written by another person, or substantial proportions of material which have been accepted for the award of any other degree or diploma at UNSW or any other educational institution, except where due acknowledgment is made in the thesis. Any contribution made to the research by others, with whom I have worked at UNSW or elsewhere, is explicitly acknowledged in the thesis. I also declare that the intellectual content of this thesis is the product of my own work, except to the extent that assistance from others in the project's design and conception or in style, presentation and linguistic expression is acknowledged.

Signed ……..

Date ……..

COPYRIGHT STATEMENT

Signed ……..

Date ……..

AUTHENTICITY STATEMENT

I certify that the Library deposit digital copy is a direct equivalent of the final officially approved version of my thesis. No emendation of content has occurred and if there are any minor variations in formatting, they are the result of the conversion to digital format.

Signed ……..

Date ……..

ACKNOWLEDGMENTS

First and foremost, I would like to express my sincere gratitude and appreciation to my supervisor, Associate Professor William Peirson for his invaluable support, encouragement and generosity of knowledge throughout this journey. Bill, all your help and advice on my research, as well as on my career, has been a constant source of motivation for me and is greatly appreciated. I would like to extend my special thanks to my co-supervisor, Professor Michael Banner for his enthusiasm and encouragement, and for sharing his vast knowledge during this project.

I would like to acknowledge the Australian Research Council under Discovery Project DP120101701 for funding this project and extend my appreciation to my colleagues at the Water Research Laboratory for their support and friendship. It has been a pleasure to work with Dr. Xavier Barthelemy. Xavier, I appreciate all your help from the early to the final stages of this research and your perpetual laughter during these several years. My thanks are also extended to Dr. Michael Allis and Dr. Daniel Howe for their help during this study. I would also like to gratefully acknowledge the expert technical assistance at WRL provided by Larry Paice, Rob Jenkins and Mark Whelan.

I am very grateful to have found new friends from all around the world over the course of this study. I would like to thank my friends in the WRL student room Armaghan, Bec, Josh, Laura, Mahmudul, Matt and Zaizatul, for being so supportive and encouraging.

I am forever indebted to my parents, brother and sisters for their endless love, immense support and encouragement throughout my entire life. I would like to express my special thanks to my sister, Rezvan and my brother-in-law, Jalal. Without their encouragement and support, it would not have been possible for me to finish this project.

ABSTRACT

Water wave breaking is a dominant dynamical process of the upper ocean, inducing strong flow-turbulence-wave interactions and air-sea exchanges. A fundamental and long-standing gap in the understanding of wave breaking is how to characterise and predict the onset of breaking.

The threshold for the onset of breaking proposed by Barthelemy *et al*. (arXiv:1508.06002v1, 2015) has been investigated intensively in the laboratory for different classes of two- and three-dimensional wave groups in deep and transitional water in the absence and presence of wind. Thermal Image Velocimetry was used to compare measurements of the wave crest surface water particle velocity with the wave crest speed determined by an array of closely-spaced wave gauges.

For the first time, a threshold crest point surface energy flux ratio (B_x) that distinguishes maximum group recurrence from marginal group breaking has been established for gravity waves. The critical value of B_x was found to be 0.835 ± 0.005 with an experimental uncertainty of each data point of ±0.020. The breaking threshold is robust for different types of unidirectional and directional wave groups. Very weak dependence on wind forcing and group bandwidth is demonstrated. No dependence on relative water depth was observed. If there is a dependence on peak spectral wavenumber, it is weak and negligible for the scales achievable in a large-scale laboratory.

This study provides more robust and universal characterisation of breaking in transitional water than the empirical non-dimensionalisation of Nelson (1994). The effect of wave grouping can generate marginally breaking waves in shallower water that are at least 30 % greater than the limit proposed by Nelson. The study supports use of a limit at least that recommended by McCowan (1894)/Miche (1944) for coastal engineering design in transitional and shallow water until it is demonstrated that there is negligible risk of strongly breaking group waves achieving higher breaker indices.

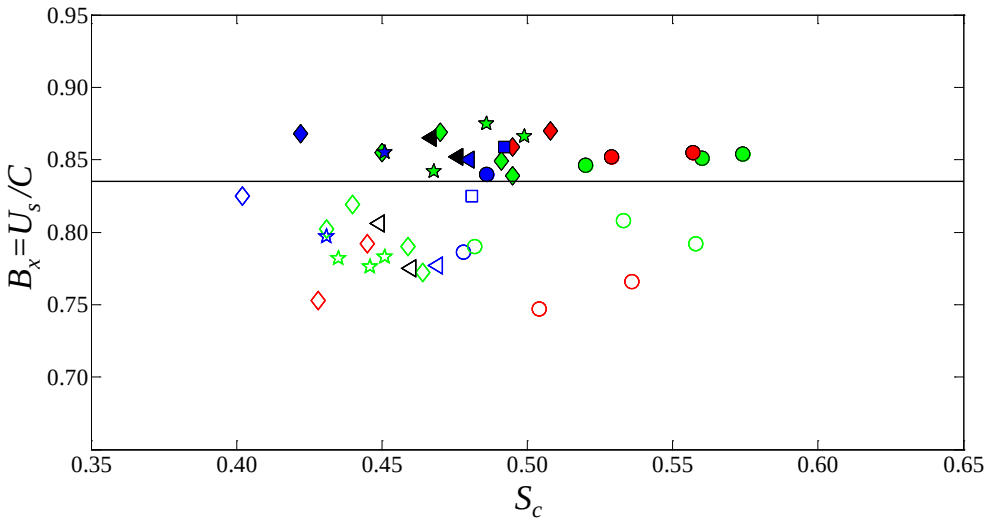

Local wave steepness S_c versus crest and surface water speed ratio at the wave crest point $B_x = U_s/C$ for C2N3 (◇), C2N5 (☆), C3N5 (□), C3N7 (◁), C3N9 (○), with maximum recurrence waves (hollow shapes) and marginal breaking waves (solid shapes). The 2D deep water waves are in blue, 2D transitional water depth waves are in green and 2D waves under wind-forcing are in black and 3D waves are in red. The horizontal line at B_x = 0.835 is the breaking threshold.

CONTENT

ORIGINALITY STATEMENT III

COPYRIGHT STATEMENT IV

AUTHENTICITY STATEMENT V

ACKNOWLEDGMENTS VI

ABSTRACT VII

CONTENT I

LIST OF FIGURES V

LIST OF TABLES IX

LIST OF SYMBOLS XI

RESEARCH OUTPUTS XIII

Peer-reviewed journal articles XIII

Conference papers XIII

Chapter *1* 1

1. INTRODUCTION 1

1.1 Overview and motivation 1

1.2 Study objectives 4

1.3 Thesis structure 4

Chapter *2* 6

2. LITERATURE REVIEW 6

2.1 Introduction 6

2.2 Wave breaking onset in deep water 7

2.2.1 Geometric criteria 8

2.2.2 Kinematic criteria 11

2.2.3 Dynamic criteria 14
2.3 Wave breaking onset in transitional and shallow water 16
2.4 Summary 19
Chapter *3* 21
3. METHODOLOGY 21
3.1 Experimental overview 21
3.2 Laboratory facilities 21
3.2.1 0.6 m wave flume 21
3.2.2 Wave Basin 24
3.2.3 Wave probes 29
3.2.4 Laser system 32
3.2.5 Thermal imaging camera 34
3.2.6 Ultrasonic sensor 35
3.3 Initial wave group conditions 36
3.4 TIV techniques 38
3.4.1 TIV system using hot water 39
3.4.2 TIV system using CO_2 laser 42
3.5 Method 46
3.5.1 Experimental setup 47
3.5.2 Local wave crest point speed (C) measurement 49
3.5.3 Horizontal water surface velocity (U_s) measurement 50
3.5.4 Measurement of B_x parameter 52
3.5.5 Local wave steepness measurement (S_c) 53
3.6 Conclusion 53
Chapter *4* 55
4. TWO-DIMENSIONAL DEEP WATER WAVES 55

4.1 Wave conditions 55
4.2 Geometric characteristics 56
4.3 Threshold of the onset of breaking 58
4.3.1 Waves in the absence of wind 60
4.3.2 Waves in the presence of wind 62
4.3.3 Wave group bandwidth 64
4.4 Conclusion 65
Chapter *5* 67
5. TWO-DIMENSIONAL TRANSITIONAL DEPTH WAVES 67
5.1 Wave conditions 67
5.2 Threshold of the onset of breaking 68
5.3 Depth limited wave heights 72
5.4 Conclusion 74
Chapter *6* 76
6. DIRECTIONAL DEEP WATER WAVES 76
6.1 Wave conditions 76
6.2 Threshold of the onset of breaking 77
6.3 Conclusion 81
Chapter *7* 82
7. CONCLUSIONS AND RECOMMENDATIONS 82
7.1 Overview 82
7.2 Methodology (chapter 3) 82
7.3 2D deep water wave groups (chapter 4) 83
7.4 2D transitional water depth wave groups (chapter 5) 84
7.5 3D deep water wave groups (chapter 6) 85
7.6 Closing remarks and recommendations 85

REFERENCES 87

APPENDIX A 97

LIST OF FIGURES

Figure 2.1- Local wave crest parameters following Kjeldsen & Myhuang (1979), H is wave height and λ is wavelength. Wave is propagating from right to left. 10

Figure 2.2- Wave height (H) to water depth (h) ratio Versus F_c (Nelson, 1994, Figure 1). 18

Figure 3.1- Sketch of the experimental setup (not to scale) used in deep-water wave study. The details of the dimensions and distances are given in the text 22

Figure 3.2- The fan and adjustable honeycomb flow guide used to establish a uniform air flow in the 0.6 m flume. 23

Figure 3.3- Sketch of the experimental setup (not to scale) used in shallow-water wave study. 24

Figure 3.4- Plan view of the wave basin and experimental setup used in directional deep-water wave study. 25

Figure 3.5- Cross section a-a showing the sketch of wave paddle units in the wave basin. 26

Figure 3.6- The cross section of the dissipation beach in the wave basin (Figure 3.4, section c-c). 27

Figure 3.7- The cross section of the trolley and measurement apparatus (Figure 3.4, section b-b). 28

Figure 3.8- The trolley used to hold and move the measurement apparatus in the wave basin. 28

Figure 3.9- Capacitance wave probes used to record water surface elevations. 29

Figure 3.10- The wave probe calibration for five gauges. The symbols indicate the observed voltages at relative elevations for each wave probe with dashed lines to linear regression slope. 30

Figure 3.11- Example of raw surface elevation time series for a bimodal wave group (red line) and filtered signals using a low pass order Chebyshev Type I filter (black line). The inset on the right indicates the detail of unfiltered and filtered signal at the wave crest. 31

Figure 3.12- The RF supply, CO_2 laser head and the mirror holder used to irradiate the water surface. 32

Figure 3.13- The enclosed room to control the TIV system remotely while the laser was operating in the wave basin. 33

Figure 3.14- Flir T420 thermal imaging camera for to acquiring images of heated patches on the water surface. 34

Figure 3.15- Microsonic mic +35 ultrasonic sensor for tracking the shutter located underneath the infrared camera. 35

Figure 3.16- The ultrasonic sensor in front of the board connected to the shutter. 35

Figure 3.17- Schematic of 13 component wave paddle for convergent wave focusing (Allis, 2013). 38

Figure 3.18- Laboratory deployment of instrumentation: thermos, wave probes and aluminium mesh to calibrate camera images 39

Figure 3.19- Tracking the heated spot on the wave crests of a monochromatic wave for two successive frames using infrared imagery to measure the surface particle velocity. The stationary white features at the right side are images of the nozzle head used to locate hot droplets on the water surface. . 40

Figure 3.20- Tracking the heated spot on the wave crests of a non-breaking C3N7 wave packet for two successive frames using infrared imagery to measure the surface particle velocity. 42

Figure 3.21- Laboratory deployment of instrumentation: CO_2 laser system, adjustable IR mirror, infrared imaging camera and computer-controlled shutter mounted on the wind tunnel. Note that the Thermos and calibration mesh were removed once the laser system was deployed. 43

Figure 3.22- Tracking the heated patch on the crest of a breaking wave at the location of crest maximum elevation for three successive frames. 46

Figure 3.23- Surface elevation time series at the location of group maximum for unforced non-breaking (— — —) and marginal breaking (——) 2D C2N3 and C3N7 waves and wind-forced non-breaking (— · —) and marginal breaking (·····) 2D C3N7 waves. C2N3 are of smaller amplitudes and the crest detail is shown by the left inset; C3N7 crest detail is on to the right inset. Time (t) is referenced to the instant of the crest maximum elevation. Note the implied steeper forward face of the marginally breaking wave in comparison with its corresponding maximally recurrent wave and the differences of the mean steepness at breaking onset between the two classes of waves. 49

Figure 3.24- Surface water velocity (m/s) for two-dimensional marginal breaking C3N7 wave group. The arrows represent the surface water velocity where $X_{cr\text{-}max}$ is the position of each point referenced to the location of crest maximum elevation of the transiting group. 51

Figure 3.25- Polynomial curve fitted to water surface velocities and the interpolated velocity at the crest maximum elevation for a marginal breaking 2D C3N7 wave group. The error bars indicate the uncertainty arising from synchronisation of the TIV measurements with the wave probes. Note that the maximum velocity occurs at the wave crest point. 52

Figure 4.1- Local wave steepness S_c versus crest and surface wave speed ratio at the wave crest point $B_x=U_s/C$ for unforced waves, showing C2N3 (◇), C2N5 (☆), C3N5 (□), C3N7 (◁), C3N9 (○), with maximum recurrence waves (hollow shapes) and marginal breaking waves (solid shapes). Error bars indicate the standard deviation of the repeat measurement set (6 to 8 replicates) and the horizontal line at B_x = 0.835 is the breaking threshold.....60

Figure 4.2- PIV measured velocities with their standard deviations along with the fitted velocities extrapolated to the positions of the fluid surface for Wave 3 by Stansell and MacFarlane (2002). 62

Figure 4.3- Wind forcing $U_{\lambda/4}/C_0$ versus crest and surface speeds ratio at the crest point $B_x=U_s/C$ for wind-forced waves, showing C3N7 (◁), C3N7U1.4 (▽), C3N7U2.0 (△), with maximum recurrence waves (hollow shapes) and marginal breaking waves (solid shapes). Error bars indicate the standard deviation of the repeat measurement set (6 to 8 replicates). 63

Figure 4.4- Benjamin-Feir Index *BFI* versus crest and surface speeds ratio at the wave crest point $B_x=U_s/C$ for unforced waves. The shapes are as defined in Figure 4.1. Error bars indicate the standard deviation of the repeat measurement set (6 to 8 replicates) and the horizontal line at B_x = 0.835 is the breaking threshold. 65

Figure 5.1- The deep water wavelength to water depth ratio versus the crest surface water velocities difference form maximum recurrence to marginal breaking over the marginal breaker crest point speeds for C2N3 (⧫), scaled C2N3 (▼), C2N5 (★) and C3N9 (●) wave packets from deep to shallow water. 70

Figure 5.2- Local wave steepness S_c versus crest and surface speeds ratio at the wave crest point $B_x=U_s/C$, showing C2N3 (◇), scaled C2N3 (▽), C2N5 (☆), C3N9 (○), with maximum recurrence waves (hollow shapes) and marginal breaking waves (solid shapes). Error bars indicate the standard deviation of the repeat measurement set (6 to 8 replicates) and the horizontal line at B_x = 0.835 is the breaking threshold. 71

Figure 5.3- Non-dimensional parameter ($\lambda\sqrt{\rho g/\sigma}$) versus crest and surface speeds ratio at the wave crest point $B_x = U_s/C$. The shapes are as defined in Figure 5.2. Error bars indicate the standard deviation of the repeat measurement set (6 to 8 replicates) and the horizontal line at $B_x = 0.835$ is the breaking threshold. 72

Figure 5.4- F_c versus H/d for waves on horizontal beds from deep to shallow water for C2N3 (◇), scaled C2N3 (▽), 3D C2N3 (Δ), C2N5 (☆), C3N9 (○), 3D C3N9 (▷) wave groups in the present study, Barthelemy *et al.* (Class 3 waves, 2013) (◁), Riedel & Byrnes (random waves, 1986) (✡), Dack & Peirson (Class 2 waves, 2005) (□) with maximum recurrence waves (hollow shapes) and breaking waves (solid shapes), Nelson's characterisation (monochromatic, 1994) (——), Miche (1944) theoretical limit (— - —) and McCowan (1894) theoretical limit of 0.78 (— — —). 73

Figure 6.1- Local wave steepness S_c versus crest point to horizontal water surface speeds at the wave crest point ratio $B_x = U_s/C$ for two-dimensional C2N3 (◇) wave groups and three-dimensional wave groups, showing C2N3 $\theta_f = 17.6°$ (▽), C2N3 $\theta_f = 42.4°$ (Δ), C3N9 $\theta_f = 17.6°$ (◁) and C3N9 $\theta_f = 42.4°$ (▷) with maximum recurrence waves (hollow shapes) and marginal breaking waves (solid shapes). Error bars indicate the standard deviation of the repeat measurement set (6 to 8 replicates) and the horizontal line at $B_x = 0.835$ is the breaking threshold. 80

LIST OF TABLES

Table 2.1- Comparison of the local geometry parameters at deep water breaking onset of different studies. 11

Table 3.1- Example calibration parameters for five wave probes. 31

Table 3.2- The locally measuring wave steepness (ak), linear wave crest speed (C_L) and water surface velocity (U_{sL}) were estimated using linear wave theory for a monochromatic paddle frequency $\omega_p = 8.976$ rad s^{-1}. These are compared with the water surface velocity (U_s) measured using the TIV technique and crest speed (C) obtained from the wave probe records. 41

Table 3.3- Measurements verifying the TIV technique. Using a monochromatic paddle frequency $\omega_p = 10.472$ rad s^{-1} and the locally measuring wave steepness (ak), linear wave crest speed (C_L) and water surface velocity (U_{sL}) were estimated using linear wave theory. The water surface velocity (U_s) was measured using the TIV technique and crest speed (C) obtained from the wave probe records. 44

Table 4.1- Wind speed at the elevation of one quarter of the dominant wavelength above SWL ($U_{\lambda/4}$) and wave paddle amplitude (A_p) for maximum recurrence and marginal breaking wave groups. 56

Table 4.2- Wind speed at the elevation of one quarter of the dominant wave length above SWL ($U_{\lambda/4}$), the average and standard deviation of measured crest steepness (S_c), crest-front steepness (ε), crest-rear steepness (δ) and horizontal asymmetry parameter (λ') for maximum recurrence and marginal breaking wave groups. The last row indicates the Kjeldsen & Myrhaug (1979) breaking threshold for each geometric parameter. 57

Table 4.3- Wind forcing ($U_{\lambda/4}/C_0$) and the average and standard deviation of measured crest point speed (C), crest point water surface particle velocity (U_s), energy flux ratio at the crest point U_s/C, peak frequency (f_0), frequency bandwidth (Δf) and Benjamin-Feir Index (BFI) for maximum recurrence and marginal breaking waves. 59

Table 5.1- The ratio of linear deep-water wavelength and water depth λ_0/d, wave paddle amplitude (A_p), the average and standard deviation of measured crest steepness (S_c), crest point speed (C), crest point water surface particle velocity (U_s), ratio of the velocities at the crest point U_s/C, non-dimensional parameter F_c, wave height to water depth ratio H/d and non-dimensional parameter $\lambda\, \rho^{0.5}\, g^{0.5}\, \sigma^{-0.5}$ for maximum recurrence and marginal breaking waves. 69

Table 6.1- Summary of the results: geometric focal length (x_f), focal angle (θ_f), wave paddle amplitude (A_p), fetch of the crest point (X_0), the average and standard deviation of measured crest steepness (S_c), crest point speed (C), crest point water surface particle velocity (U_s), ratio of the velocities at the crest point U_s/C for maximum recurrence and marginal breaking waves. 79

LIST OF SYMBOLS

a	wave amplitude (m)
A_p	wave paddle amplitude (m)
B	breaking onset variable
B_x	breaking onset variable in the wave propagation direction
BFI	Benjamin-Feir index
C	wave crest point speed (m/s)
C_0	wave phase speed (m/s)
C_{t2}	chirp rate of the linear modulation
d	water depth (m)
d_b	water depth at breaking point (m)
E	energy density (J/m^2)
f	wave crest fetch (m)
f_0	peak frequency (Hz)
F	energy flux (W/m)
g	acceleration due to gravity (m/s^2)
H	wave height (m)
H_b	breaking wave height (m)
k	wavenumber (m^{-1})
k_0	wavenumber associated with the peak frequency (m^{-1})
L'	horizontal distance from the wave crest to zero-upcross
L''	horizontal distance from the wave crest to zero-downcross
n	probe number
N	number of waves in an individual wave group
P	pressure (N/m^2)
S_c	local wave steepness
SWL	still water level
t	time (s)
T	wave period (s)
U_s	horizontal water particle velocity (m/s)
$U_{\lambda/4}$	wind speed at the elevation of one quarter of the dominant wavelength above SWL (m/s)
W	Weber number

x_f	geometric focal length in the wave propagation direction (m)
x_p	paddle motion (m)
X_0	crest point fetch (m)
Δf	frequency bandwidth (Hz)
δ	crest-rear steepness
ε	crest-front steepness
η	local surface elevation in relation to the still water level (m)
θ_f	geometric focal angle
λ	wavelength (m)
λ'	vertical asymmetry
μ	horizontal asymmetry
ρ	fluid density (kg/m^3)
σ	surface tension (N/m)
Φ_m	paddle phase component for each wave paddle
ω_p	wave paddle angular frequency (rad/s)

RESEARCH OUTPUTS

Peer-reviewed journal articles

SAKET, A., PEIRSON, W. L., BANNER, M. L. & BARTHELEMY, X. 2017 Wave breaking threshold for directional waves. *J. Fluid Mech*. (in preparation)

SAKET, A., PEIRSON, W. L., BANNER, M. L. & ALLIS, M. J. 2017 Wave breaking onset of two-dimensional wave groups in uniform intermediate depth water. *J. Fluid Mech*. (submitted)

SAKET, A., PEIRSON, W. L., BANNER, M. L., BARTHELEMY, X. & ALLIS, M. J. 2017 On the threshold for wave breaking of two-dimensional deep water wave groups in the absence and presence of wind. *J. Fluid Mech.* **811**, 642-658.

SAKET, A., PEIRSON, W. L., BANNER, M. L. & BARTHELEMY, X. 2016 Development of a particle image velocimetry technique to measure the water surface velocity. *IOP Conf. Series: Earth and Environmental Science.* **35**, 012021.

Conference papers

SAKET, A., PEIRSON, W. L., BANNER, M. L. & BARTHELEMY, X. 2016 Determining the onset of breaking: laboratory investigations. *2nd International Workshop on Air-Sea Gas Fluxes.* Brest, France.

SAKET, A., PEIRSON, W. L., BANNER, M. L. & BARTHELEMY, X. 2015 An experimental investigation of extreme water velocities and deep water wave breaking. *Australasian Coasts & Ports Conference: 22nd Australasian Coastal and Ocean Engineering Conference and the 15th Australasian Port and Harbour Conference.* Auckland, New Zealand: Engineers Australia and IPENZ. 785-89.

BARTHELEMY, X., BANNER, M. L., PEIRSON, W. L., FEDELE, F., ALLIS, M. J. & **SAKET, A.** 2015 The dance of highly nonlinear unsteady surface waves-kinematic properties and slowdown. *Australasian Coasts & Ports Conference: 22nd Australasian Coastal and Ocean Engineering Conference and the 15th Australasian Port and Harbour Conference.* Auckland, New Zealand: Engineers Australia and IPENZ. 36 – 41.

SAKET, A., PEIRSON, W. L., BANNER, M. L., BARTHELEMY, X. 2015 Development of a particle image velocimetry technique to measure the water surface velocity. *7th International Symposium on Gas Transfer at Water Surfaces.* Seattle, Washington, USA.

BARTHELEMY, X., BANNER, M. L., PEIRSON, W. L., ALLIS, M. J., **SAKET, A.** & DIAS, F. 2014 Highly non-linear unsteady surface waves properties: kinematics and slowdown. *KOZWaves, Kiwi-Oz Waves Conference*. Newcastle, NSW, Australia.

Chapter 1

INTRODUCTION

1.1 Overview and motivation

Water wave breaking is a dominant dynamical process of the upper ocean, inducing strong flow-turbulence-wave interactions and air-sea exchanges (Banner & Peregrine, 1993; Melville, 1996; Perlin & Schultz, 2000; Perlin *et al*., 2013; Peirson *et al.*, 2014). Moreover, wave breaking is a central importance in the study of beach dynamics, coastal and offshore engineering and air-sea fluxes. Phillips (1977, § 3.9) provides a very insightful characterisation of wave breaking and its historical developments at that time. The above references highlight the heightened interest in wave breaking and its consequences in the ensuing decades. However, as Holthuijsen (2007, p.188) points out "*A complicating factor is that there is no generally accepted, precise definition of breaking*". Despite the high visibility of whitecaps at sea and wave breaking at coastlines and beaches, there remains a fundamental and long-standing gap as to how to characterise and predict the onset of wave breaking.

The current design guidelines for coastal engineering are based on extensive monochromatic wave testing and the effects of wave grouping have been generally ignored or neglected in the manuals. Whilst it has been shown numerically and experimentally that nonlinear wave interaction plays a major role in the breaking process (e.g. Dold & Peregrine, 1986; Stansberg, 1997; Banner & Tian, 1998; Tulin & Wadesa, 1999; Banner & Song, 2002; Banner *et al*., 2002). Recent studies show the strong effects of wave groups

on the onset of wave breaking (Svendsen & Veeramony, 2001; Song & Banner, 2002; Banner & Peirson, 2007).

The quest to determine a reliable means of determining the onset of wave breaking has spanned 135 years since Stokes (1880) developed the first theoretical prediction of wave breaking. Over the past half century, many criteria have been proposed to determine the onset of wave breaking, e.g. Galvin (1969), Kjeldsen & Myrhaug (1979), Rapp & Melville (1990), Easson (1997), Nepf *et al*. (1998) and Diorio *et al*. (2009). Based on local wave properties, these criteria can be segregated into three categories: geometric, dynamic and kinematic criteria (Wu & Nepf, 2002). Although the kinematic breaking criterion or geometric wave properties which will be discussed in Chapter 1 have been traditionally used as indicators of breaking onset in deep or shallow water, these criteria have largely failed and are not universally applicable (Melville, 1994; Banner & Peirson, 2007; Perlin *et al.*, 2013).

Song & Banner (2002) developed a more recent genre of breaking onset criteria based on energy flux rates at steep crests, which appear to provide a more robust basis for quantifying breaking onset (Banner & Peirson, 2007; Tian *et al*., 2008). A significant refinement of this approach was published very recently by Derakhti & Kirby (2016). The interested reader is referred to Perlin *et al*. (2013) for a comprehensive overview of the status of the various proposed breaking onset criteria.

Very recently, Barthelemy *et al*. (arXiv:1508.06002v1, 2015) proposed a breaking onset threshold based on a local threshold of wave energy flux in the crest region of a steep wave through an ensemble of boundary element numerical simulations of fully-nonlinear 2D and 3D wave packets in deep and finite depth water. They found that the onset of breaking occurs once the water surface particle speed at the wave crest point exceeds 0.855±0.005 of the speed of the slowing crest point as it passes through the maximum of a

wave group. This criterion was observed to be robust, for both long-crested and short-crested waves.

This present study is motivated by the recent numerical study of Barthelemy *et al*. (arXiv:1508.06002v1, 2015) and the primary goal of the study is to investigate the threshold in the laboratory intensively for 2D and 3D wave groups in deep, transitional and shallow water. This study aims to extend the numerical study of Barthelemy *et al*. (arXiv:1508.06002v1, 2015) to include different classes of wave groups in the absence and presence of wind using moderate wind forcing.

To avoid the uncertainty associated with capturing wave breaking onset events with their attendant very short time scales (Duncan *et al*., 1999), this present study identified the threshold for wave breaking as follows. Using the approach of Rapp & Melville (1990) and Banner & Peirson (2007), the rate of energy convergence at the point of initial wave breaking was systematically increased. Repeat observations of the wave groups transitioning through the point of initial breaking revealed that two conditions could be clearly defined.

Up to a certain wave paddle forcing level, dominant waves of successive groups were observed to progress through the group envelope maximum with no observable residual disturbance of the water surface. This condition was termed the maximum recurrent or maximum non-breaking threshold, and indicated a *lower bound* to the breaking threshold. Further slight but sufficient augmentation of paddle forcing level triggered a significant change in dominant wave behaviour at the initial break point. For each successive group, a disturbance in the wave surface was observed to occur at the same fetch, characterised by a visible bulge just ahead of the wave crest (Duncan *et al*., 1999), accompanied by surface irregularity and trailing patches of capillary ripples. This condition was termed the marginal breaking condition and used to identify the *upper bound* of the breaking threshold. Based on this definition of the breaking threshold, this present contribution critically examines the proposal of Barthelemy *et al*. (arXiv:1508.06002v1, 2015).

1.2 Study objectives

The objectives of this study are to investigate the robustness of a threshold for the onset of wave breaking. To achieve this goal the following approach has been adopted:

(1) Development of a laboratory method to generate wave groups and measure the wave crest velocity and wave characteristics.
(2) Development of an accurate Thermal Image Velocimetry (TIV) technique for observing and measuring the horizontal water particle velocities at the crests of waves transitioning through the group maximum.
(3) Test the breaking threshold (geometry and the ratio of local energy flux velocity to the crest point speed) for uni-directional (2D) wave groups in deep and transitional water.
(4) Test the breaking threshold for directional (3D) wave groups in deep water.
(5) Explore the implications for understanding the breaking onset for uni-directional (2D) and directional (3D) water waves in both deep and shallow water.

1.3 Thesis structure

The present dissertation consists of 7 chapters. The introduction, motivation and the study aims were presented in Chapter 1. Review of the previous research on the onset of wave breaking and the advances as well as the current gaps on the knowledge of wave breaking is presented in Chapter 2.

In Chapter 3, the facilities and the measurement apparatus are described. Data analysis, filtration, calibration methods and a state-of- the-art thermal image velocimetry technique are described. The initial wave group conditions are defined and finally, the methodology for measuring the wave

crest point and horizontal water surface speeds as well as the local wave geometry is described.

In Chapter 4, 2D deep water wave groups are examined to investigate the robustness of the crest point surface energy flux ratio $B_x = U_s/C$ in the laboratory with different group classes and the sensitivity of the threshold is evaluated for different spectral bandwidths and degrees of wind forcing.

In Chapter 5, uni-directional waves in three different transitional wave depths are considered and the threshold for the onset of breaking B_x is investigated for different wave group structures. The influence of scaling is accessed for one case. The breaker index for deep to shallow water waves is compared with the limiting wave heights proposed by Nelson (1994).

In Chapter 6, the effect of directionality convergent waves is investigated for deep water 3D waves in a wide wave basin and the results as compared with 2D waves. The robustness of the breaking threshold is discussed and the sensitivity of the threshold is evaluated for different focal angles.

In Chapter 7, the conclusions of this study are drawn and some recommendations for future studies are presented.

Chapter 2

LITERATURE REVIEW

2.1 Introduction

Breaking waves play an importance role in the dynamics of the upper ocean, air-sea and turbulence-wave interactions and have influence on climate change by reducing carbon dioxide fluxes into the ocean (Banner & Peregrine, 1993; Melville, 1996). Wave breaking can be observed in deep water as well as beaches and shallow water and it is one of the important factors in the safety of vessels in the ocean. Since hydrodynamic load parameters of waves i.e. velocity and acceleration in breaking waves are far larger than non-breaking waves with the same height (Melville & Rapp, 1998; Grue *et al.*, 2003), breaking waves are the critical design condition for marine and coastal structures.

Wave breaking is one of the key factors in oil slick dispersant and transport of oil droplets into upper layers of the water column (Tkalich & Chan, 2002). Surface particle transport is a combination of wave (Phillips, 1977) and wind drift (Phillips & Banner, 1974; Peirson & Banner, 2003) imposed on the underlying, large-scale circulation. Breaking waves inject bubbles and turbulence into the water column and have significant impact on dispersing of oil spilled on the sea surface. Critically, the occurrence of wave breaking coincides with the subduction of surface fluid and floating particles (Peirson & Banner, 2003). The intense fluid stresses induced by wave breaking (Peirson & Banner, 2003) generate turbulence which, in turn, mixes the near

surface water layers and transport bubbles to depth (Boettcher *et al*., 2000; Terrill *et al.*, 2001; Melville & Matusov, 2002).

Despite the importance of wave breaking to understanding the behaviour of open water surfaces, the central question in the determination of wave breaking onset has remained unresolved.

Stokes (1880) developed his theoretical approach culminating in his steady irrotational wave of maximum steepness, beyond which breaking was assumed to occur. During the subsequent 135 years, a number of other strategies have been proposed for determining a robust threshold for breaking of freely-propagating water waves. For example, Banner & Phillips (1974) refined Stokes' approach to account for the effects of wind drift, investigating its impact via the kinematic criterion in which breaking onset is linked directly to fluid at the crest point exceeding the speed of the crest. Other criteria based on a limiting fluid particle acceleration for stability of the crest point have also been proposed and investigated (e.g. Longuet-Higgins, 1963, Appendix). Comprehensive overviews of the significance of wave breaking can be found in the review articles by Banner & Peregrine (1993), Thorpe (1995), Melville (1996), Duncan (2001) and Perlin *et al*. (2013).

2.2 Wave breaking onset in deep water

The characterisation and prediction of the breaking onset have remained a fundamental and long-standing gap in our understanding of wave breaking in spite of its importance in air-sea interactions and structural loads. A breaking wave has an irregular crest shape which starts very quickly and evolves rapidly. Over the past few decades, many criteria have been proposed using numerical models, experimental investigations and field studies with the aim of determining a threshold for breaking of freely-propagating water waves, involving geometric, kinematic and dynamic criteria (Rapp & Melville, 1990; Banner & Tian, 1998; Nepf *et al*., 1998). Very recently, Barthelemy *et al*. (arXiv:1508.06002v1, 2015) proposed a threshold which is described with

reference to energy flux considerations and distinguishes maximum recurrence from marginal breaking waves. In the following sections, these parameters and a summary of the previous studies are presented.

2.2.1 Geometric criteria

Geometric criteria based on the limiting steepness and local crest geometry has been proposed as indicators of wave breaking initiation (Stokes, 1880; Miche, 1944; Rapp & Melville, 1990; Kjeldsen & Myrhaug, 1979). The wave steepness is formed by two important geometric parameters i.e. wave amplitude (a) and wavelength (λ). Wavelength is defined by linear wave theory as:

$$\lambda = \frac{gT^2}{2\pi} \tag{2-1}$$

where g is the gravity acceleration (m s^{-2}) and T is wave period (s). These parameters can be used to define the global wave steepness (ak), where $k=2\pi/\lambda$ is the wavenumber. Stokes (1880) theoretical approach showed that beyond the global steepness of 0.443 with a limiting crest angle of 120°, breaking will occur. Laboratory experiments show that the limiting steepness for onset of breaking is typically smaller than Stokes limit.

Duncan (1981, 1983) studied steady wave breaking and measured the local wave height H (the vertical distance between the crest and the following trough in his studies) and wavelength (λ) at breaking. He found H/λ=0.1 for breaking waves and a corresponding symmetric wave would have a limiting steepness of approximately 0.31. Ramberg & Griffin (1987) studied deep water quasi-steady breakers in a convergent channel and found H/λ=0.132 (ak = 0.41). Rapp & Melville (1990) conducted laboratory experiments for unsteady deep water waves and described the onset of breaking considering a global spectrum-based steepness. They found that the incipient of breaking can be occurred at a much lower steepness ($ak \simeq 0.25$).

In addition, it was found that the geometric criteria are affected by wave directionality, spectral shape and wind forcing. Wu & Nepf (2002) investigated three-dimensional waves experimentally to examine the influence of directionality on wave breaking criteria and found that directionality and wave spectral shape affect the steepness at breaking and breaking onset. The experimental results of Kway *et al*. (1998) showed that the wave steepness at breaking can be affected by spectral shape. Banner & Phillips (1974) investigated the effects of wind forcing on the breaking steepness and found that surface drift due to wind forcing decreases the maximum wave height and consequently the steepness of incipient breaking.

The previous studies showed that the global wave steepness is not a robust parameter to predict the breaking onset and visualisation techniques have shown that during breaking, waves become more asymmetric. Therefore, a number of parameters were defined based on the local crest geometry. Bonmarin (1989) examined different local geometric parameters of breaking in deep water using a visualising technique and showed that the significant asymmetry at breaking onset is an element which has effect on the differences between the Stokes' limiting and experimental measurements, and should be considered in theoretical computations. It was also showed that the degree of asymmetry is more for plunging breakers. Kjeldsen and Myrhuag (1979) defined the asymmetry parameters to describe the local steepness and asymmetry (Figure 2.1).

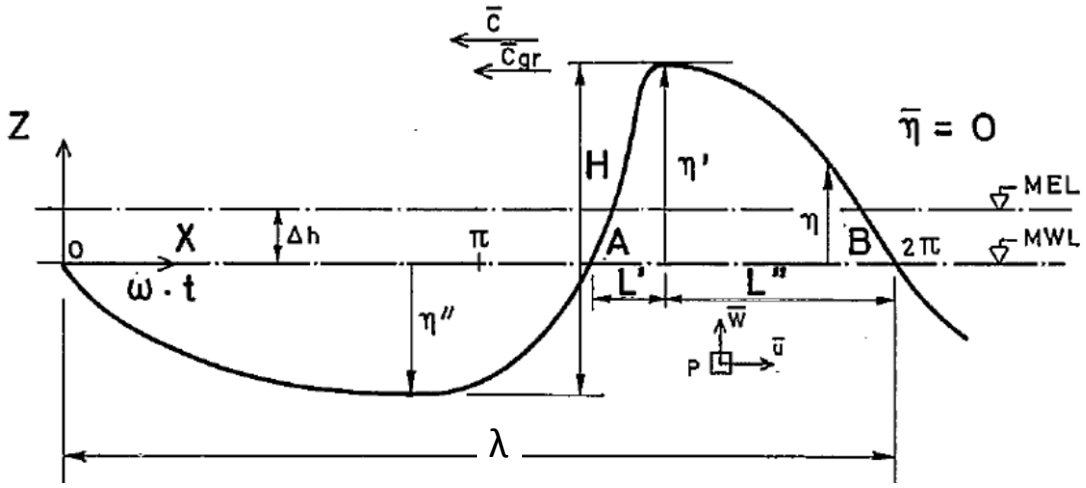

Figure 2.1- Local wave crest parameters following Kjeldsen & Myhuang (1979), H is wave height and λ is wavelength. Wave is propagating from right to left.

The local wave geometry parameters are crest-front steepness ε, crest-rear steepness δ, vertical asymmetry λ' and horizontal asymmetry μ and define as follows:

$$\varepsilon = \frac{\eta'}{L'} \tag{2-2}$$

$$\delta = \frac{\eta'}{L''} \tag{2-3}$$

$$\lambda' = \frac{L''}{L'} \tag{2-4}$$

$$\mu = \frac{\eta'}{H} \tag{2-5}$$

where η' is the wave amplitude, L' and L'' is the horizontal distance from the wave crest point to zero-upcross of crest front and zero-downcross of crest rear, respectively and H is wave height. Kjeldsen and Myrhuag (1979) and Bonmarin (1989) determined the local crest geometry parameters of spiling and plunging breakers for two-dimensional waves using visualising techniques. The summary of their results is tabulated in Table 2.1. The results show that the local crest steepnesses are more robust in comparison with limiting steepness S_c.

Table 2.1- Comparison of the local geometry parameters at deep water breaking onset of different studies.

	ε	δ	λ'	μ
Kjeldsen and Myrhuag (1979)	0.32	0.26	0.9	0.84
Bonmarin (1989)	0.31	0.26	0.81	0.6
She *et al.* (1994)				
3D- Single-frequency focusing	0.82	0.66	1.16	0.62
3D- Multifrequency focusing	0.51	0.30	1.10	0.65
Wu & Nepf (2002)				
2D	0.38	0.24	1.33	0.71
3D-diffracting	0.39	0.24	0.74	0.69
3D-focusing	0.41	0.27	1.34	0.70

She *et al.* (1994) applied focusing 3D waves to examine the local geometry of breaking and used a range of convergent angles. They found that the crest-front steepness increased from 0.51 to 1.02 by increasing the convergent angle. Wu & Nepf (2002) investigated these geometric criteria in the laboratory using 2D and diffracting and focusing 3D waves. The results of their study are summarised in Table 2.1 and show that the local steepness at the incipient of breaking is sensitive to wave directionality.

The determination of the steepness and crest's geometric parameters of breaking waves in laboratory experiments is difficult as the wave profile close to breaking has an irregular shape and evolves rapidly in time and space, which may complicate the definition and determination of incipient wave breaking.

2.2.2 Kinematic criteria

Kinematic breaking criteria assume that when the horizontal crest particle velocity U_s exceeds the wave phase speed C_0, the wave will start to break (Rankine, 1862; Kinsman, 1965). As the wave crest shape of a breaking wave changes rapidly, measuring the phase speed at the wave crest is complicated

and a range of crest speeds can be defined where the water particle velocities usually exceed these speeds (Banner & Peregrine, 1993). Accurate measurement of the surface water particle velocities is critical to testing the validity of the kinematic criterion.

Visualisation techniques play a central role in fluid mechanics in quantifying the behaviour of a flow field. One of the main non-intrusive techniques for velocity and fluid flow measurements is Particle Image Velocimetry (PIV). PIV is a state-of-the-art non-intrusive technique for velocity and fluid flow measurements. Due to ongoing improvements in image hardware and processing techniques, the diversity of applications of the PIV method continues to increase. During the last two decades, the PIV technique has been widely used in the field of wave mechanics (Peirson, 1997; Gray & Greated, 1998; Jensen *et al*., 2001, Siddiqui *et al*., 2001; Stansell & MacFarlane, 2002; Jessup & Phadnis, 2005; Muste *et al*., 2005; Garbe *et al*., 2007). Thermal imaging cameras are powerful tools for measuring the temperature distributions on the surface of open water. The velocity distribution of a water surface can also be determined by recording the motion of the water surface temperature distribution using thermal imaging cameras. Veron & Melville (2001) and Veron *et al*. (2008) developed a thermal marking velocimetry (TMV) method using infrared techniques to measure the water surface velocities, vorticity, and divergence field in the field and laboratory studies. They utilised a laser heated thermal marker instead of adding particles to visualise the flow and tracked the displacements of heated patterns on the water surface using an active technique and infrared imagery.

A number of experimental studies have been conducted to examine the kinematic breaking criterion using PIV methods to obtain the water surface velocities at the wave crest (Melville & Rapp, 1988; Perlin *et al*., 1996; Chang & Liu, 1998; Stansell & MacFarlane, 2002; Oh *et al.,* 2005; Shemer & Liberzon, 2014). Melville & Rapp (1988) utilised a novel application of laser anemometry to measure the water particle velocities for comparing the fluid

and phase velocities of breaking waves. Assuming linear theory to define the crest speed, they found that the ratio of the horizontal water surface speed to the crest speed was less than 0.58. Perlin *et al.* (1996) captured velocity fields using PIV and particle tracking velocimetry (PTV) within the crest of a single wave transitioning from a pre-breaking to plunging state. They found that the magnitude of the horizontal velocity of the overturning crest was 30% larger than the wave phase speed C_0 defined using linear theory. However, prior to the overturning, they found that the water surface velocity at the wave crest was approximately 76 % of the linear phase speed. Chang & Liu (1998) applied a PIV technique to monochromatic waves in shallow water using linear wave theory to estimate the wave speed. They found that close to the wave breaking the ratio of the surface and phase speeds was 0.86 and when the particle velocity at the wave crest was horizontal, the ratio was increased to 1.07. Stansell & MacFarlane (2002) investigated the kinematic breaking criterion experimentally. From their measurements, they concluded that wave breaking was initiated at a ratio of crest water speed to crest point speed significantly less than unity.

Qiao & Duncan (2001) show that at the transition to spilling breaking, the maximum water velocity in the crest of the wave shifts to the forward face of the wave. They also show a systematic increase in the maximum water velocity in the crest as a proportion of the crest point speed when expressed as a function of crest propagation distance. Rapp & Melville (1990), Stansell & MacFarlane (2002), Jessup & Phadnis (2005), Banner & Peirson (2007), Tian *et al*. (2010) and Banner *et al*. (2014) found that the crest point speed C of breaking waves is approximately 10 % to 20 % slower than linear phase speed. Oh *et al.* (2005) found that breaking of strongly-forced wind waves is observed when the crest point surface velocities are substantially less than the crest point speed. However, their observations do not distinguish when individual waves were actually breaking. Consequently, their data does not permit a robust assessment of whether there is a systematic difference

between crest water speed to crest speed ratios of non-breaking waves in comparison with those of breaking waves.

The numerical, experimental and field studies of Banner *et al*. (2014) for deep water wave groups showed that the wave crests systematically slow down while they approach to their maximum elevation and reaccelerate afterwards. Shemer & Liberzon (2014) performed PTV measurements for the breaking onset of Peregrine breather-type wave trains and found that the crest speed of the steepest wave slows down and becomes significantly slower than the linear wave phase speed. They modified the kinematic criterion to conclude that the onset of breaking is induced by the slowdown of the crest.

2.2.3 Dynamic criteria

The dynamic criteria have been determined based on downward acceleration at the crest (Longuet-Higgins, 1969), wave energy flux rates (Schultz *et al*., 1994; Banner & Tian, 1998) and higher harmonic energy evolution (Rapp & Melville, 1990; Kway *et al*., 1998).

Song & Banner (2002) proposed a dynamic criterion for two-dimensional waves based on a dimensionless diagnostic group growth rate function δ_{th} as an indicator to predict the onset of wave breaking. They found that the threshold of δ_{th} in the range of 1.3×10^{-3} to 1.5×10^{-3} can be used to determine the breaking or recurrence. This was confirmed experimentally by Banner & Peirson (2007) in deep water, Tian *et al*. (2008) and Tian *et al*. (2010) in transitional water depth. A significant refinement of this approach was published lately by Derakhti & Kirby (2016).

Very recently, Barthelemy *et al*. (arXiv:1508.06002v1, 2015) proposed a breaking onset threshold based on a local threshold of wave energy flux in the crest region of a steep wave through an ensemble of boundary element numerical simulations of fully-nonlinear 2D and 3D wave packets in deep and finite depth water. They found that predicting the subsequent local onset of

breaking can be described with reference to energy flux considerations. For nonlinear wave groups, the local energy flux vector is defined as:

$$\underline{F} = \underline{U}(P + \rho g z + 0.5\rho U^2) \tag{2-6}$$

where $\underline{U}$ is velocity and $U=|\underline{U}|$, P is pressure, ρ is the fluid density and z is the elevation). The energy density per unit volume is defined as:

$$E = P + \rho g z + 0.5\rho U^2 \tag{2-7}$$

When the local energy flux normalised by the local energy density, it can be considered as a local energy flux velocity. At the wave surface and under the *specific conditions* of zero surface pressure, this local energy flux velocity reduces to the water surface particle velocity, which maximises at the wave crest point. At the wave crest point (used interchangeably with the 'crest maximum elevation' throughout this paper), the water surface particle velocity is denoted by U_s. Based on the local energy flux velocity ($\underline{F}/E$) and the local (horizontal) crest point speed (C), Barthelemy *et al*. (arXiv:1508.06002v1, 2015) define a new breaking onset variable, which is the ratio of the local energy flux velocity and the local crest point speed.

$$\underline{B} = \frac{\underline{F}/E}{C} \tag{2-8}$$

On the unforced water surface and in the wave propagation direction (taken as the x direction), this reduces to $B_x = (U_s/C)$. They found that the onset of breaking occurs once the water surface particle speed at the wave crest point exceeds a critical proportion of the speed of the slowing crest point as it passes through the maximum of a wave group. The critical threshold was observed to be robust, for both long-crested and short-crested waves.

Seiffert & Ducrozet (2016) investigated the breaking parameter propose by Barthelemy *et al*. (arXiv:1508.06002v1, 2015) and Saket *et al*. (2017) using numerical models for modulated, chirped and random waves in deep water.

They found that the onset of breaking threshold is robust for different wave types and this threshold is ranged between 0.84 and 0.86.

The perspective of the current study is that the critical transition in energy convergence rate from maximum recurrence to the weakest spilling breaking defines a breaking threshold. Above this threshold, the wave will break. Apart from this latest work, the interested reader is referred to Allis (2013) for a comprehensive overview of the status of the various proposed dynamic criteria of breaking.

2.3 Wave breaking onset in transitional and shallow water

Accurate determination of the maximum wave height H is a fundamental requirement for designing the marine structures in the nearshore coastal regions and on offshore coral reefs. The breaker index is the ratio of wave height to water depth at breaking $(H/d)_b$ (CERC, 1984). The subscript b denotes the value at breaking. The investigations have been conducted for waves on horizontal bed and on beds of finite slope. Miche (1944) theoretically showed that the limiting wave steepness at breaking $(H/\lambda)_b$ in transitional water depth could be approximated using:

$$\frac{H_b}{\lambda_b} = 0.142 \ \tanh\left(\frac{2\pi d_b}{\lambda_b}\right) \tag{2-9}$$

where beyond this limit wave breaking will occur. Theoretical calculation by McCowan (1894) showed that the maximum value of H/d prior to breaking of solitary wave in shallow water is 0.78 which is commonly used in coastal engineering design for horizontal and very gentle bed slopes. Yamada *et al*. (1968) revised the value determined by McCowan (1894) and proposed revised value of 0.8261 (Goda, 2010). Weggel (1972) used monochromatic waves to investigate the wave breaking for a series of wave steepness and beach slopes and proposed a number of design curves. He found a breaker index of 0.78 for horizontal slope. The laboratory studies and field observations on steeper slope showed that in shallow water the breaker

index depends on the steepness and beach slope (Galvin, 1969; Iversen, 1952; Goda, 1970; Weggel, 1972; Nelson, 1994).

Extensive further work in the laboratory and in the field by Nelson (1985, 1994) found that the maximum wave height to water depth ratio for shallow water waves propagating on a horizontal bed could not exceed the value of 0.55 (Figure 2.2). Based on the experimental results, Nelson (1994) proposed a relationship to predict the limiting wave heights using a non-dimensional parameter F_c as follows:

$$(H/d)_{\max} = \frac{F_c}{22 + 1.82F_c} \tag{2-10}$$

where F_c was adopted from Swart & Loubser (1979) and is defined as:

$$F_c = \frac{g^{1.25} H^{0.5} T^{2.5}}{d^{1.75}} \tag{2-11}$$

where g is the gravity acceleration (m s^{-2}), H is wave height (m), T is wave period (s) and d is water depth (m).

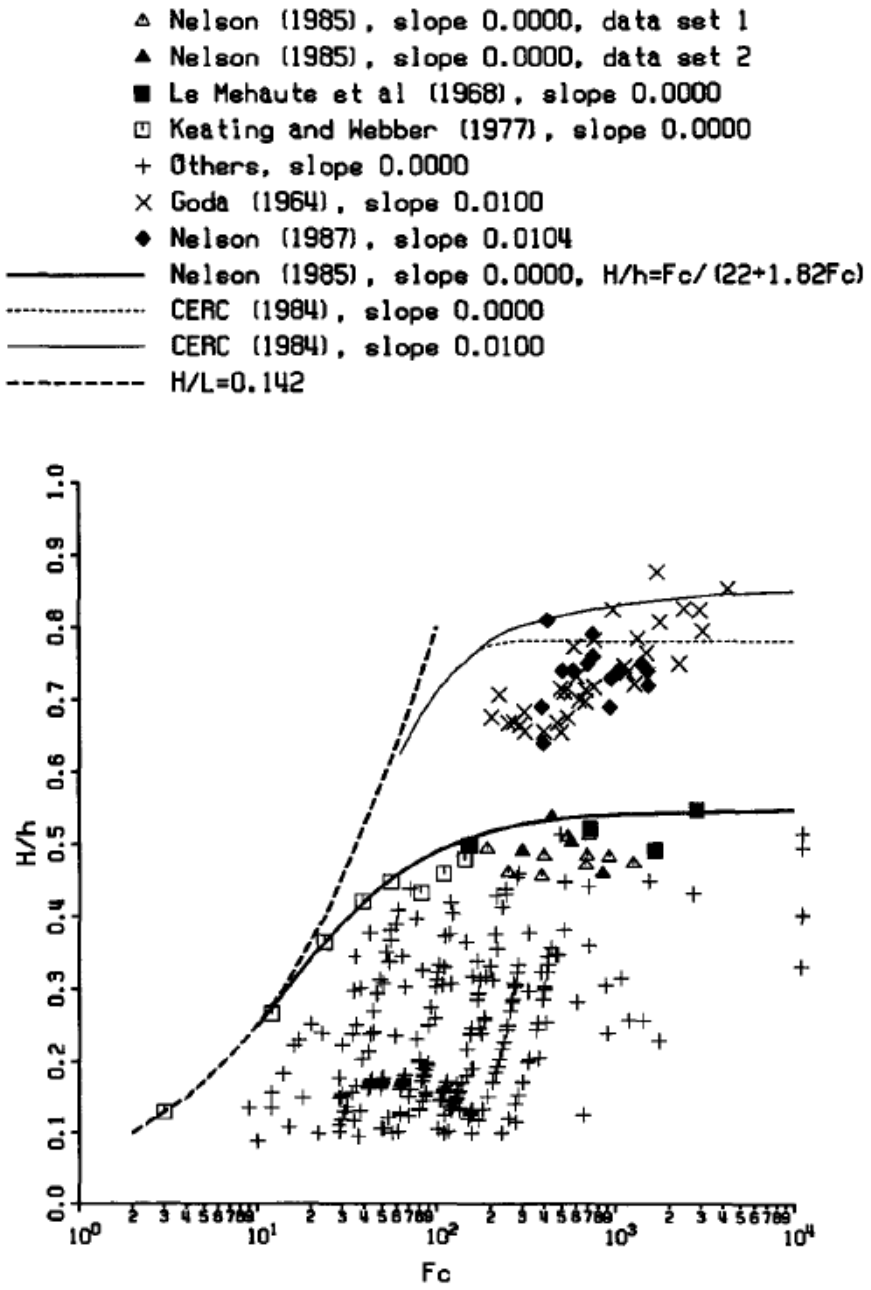

Figure 2.2- Wave height (H) to water depth (h) ratio Versus F_c (Nelson, 1994, Figure 1).

The differences between the recommendations of Weggel (1972) and Nelson (1994) are perplexing.

Riedel & Byrne (1986) carried out a laboratory investigation using monochromatic and random trains over a horizontal bed flume. Their experimental study showed that the values of H_b/d_b ranged from 0.44 to 0.54 with F_c between 49 and 150 for random waves and the largest value was 0.54

with F_c=150. They concluded that the limiting ratio of 0.55 proposed by Nelson (1985) applies equally well to random waves. However, it should be noted that, despite the ratio not exceeding the limit of 0.55, their experiments were conducted in the transitional water depth and their measured value of H/d exceeded Nelson's curve by up to 15 %. Gourlay (1994) measured the transformation of regular waves over a laboratory model of a coral reef. It was found that the largest wave height to water depth ratio never exceeds 0.55 for shallow water waves and the limiting wave height increases by increasing F_c or the bed slope. Massel (1996) evaluated the maximum possible wave height limit over a horizontal bed theoretically in transitional water depths using monochromatic waves. The maximum wave height was found to be less than 0.6 d which is in agreement with the limit proposed by Nelson (1994).

Dack & Peirson (2005) investigated whether the spatial development of wave groups can influence the breaker index. They carried out a laboratory experiment to investigate the effect of uni-directional bimodal initial spectrum wave groups on breaker index of shoaling waves when propagating onto a horizontal bed. They found a maximum breaking wave height to water depth ratio of exceeding Nelson's curve by 22 %. They concluded that the intra-wave group interactions can play a key role in determining the initiation of wave breaking in transitional water. Recently, Barthelemy *et al.* (2013) extended numerically this work using focussed wave groups propagating over a flat bed and found the value of $(H/d)_{max}$ = 0.605.

2.4 Summary

In deep water, the kinematic and geometric criteria have been shown to be unreliable predictors of the onset of wave breaking. Dynamic criteria based on energy flux rate show more promising ability to characterise the onset of wave breaking.

In transitional and shallow water, investigations have focussed on the use of breaker indices to determine breaking onset index. Extensive investigations have yielded significantly different results of the breaker index. Recent work has shown that wave grouping plays an important role in the determination of the breaker index for water waves in transitional water.

In the present dissertation, the threshold for the onset of breaking proposed by Barthelemy *et al.* (arXiv:1508.06002v1, 2015) is systematically investigated for the first time in the laboratory. The impact of wave groups on the breaker index is also examined using both spatially-focussed and bimodal wave groups propagating over a horizontal bed.

In the next chapter, the details of the experimental facilities and instrumentation as well as the methodology used to conduct this study are provided.

Chapter 3

METHODOLOGY

3.1 Experimental overview

Numerical models based on inviscid flows have a number of limitations in modelling breaking waves, particularly after the breaking onset (Barthelemy *et al.*, arXiv:1508.06002v1, 2015). Consequently, systematic and precise physical measurements of wave breaking play a crucial role in understanding wave breaking mechanisms. Since the wave breaking event is a very complex phenomenon, accurately measuring the breaking behaviour in the field is difficult. Therefore, during this study, a systematic laboratory investigation was conducted to attain precise measurements of deep and transitional water waves.

3.2 Laboratory facilities

The experiments were carried out at UNSW Sydney, Water Research Laboratory (WRL) in the Northern Beaches Campus, Manly Vale, Australia. The laboratories are located near Manly Dam and the water was supplied from a reservoir adjacent the dam. A 0.6 m wide flume and a wide wave basin were used for generating waves and data collection.

3.2.1 0.6 m wave flume

The 0.6 m wave flume is 30 m long, 0.6 m wide and 0.6 m deep with glass side walls and a solid floor. The glass sidewalls minimise the friction along the

flume sidewalls and allow observation of the waves from the sides of the tank. The flume was used to investigate the 2D waves in deep and transitional water in the presence and absence of wind. The waves propagating along the tank were two-dimensional for both deep and transitional water waves.

3.1.1.1 Deep-water waves

A computer-controlled, flexible cantilevered wave paddle fronted by synthetic damping mat was used to generate deep-water waves. A National Instruments Data Acquisition (NIDAQ) PCI6221 card was used for sending the signal to the actuator using LabVIEW software. A perforated sloping bed and flexible reticulated polyester-urethane foam absorbent beach was installed at the other end of the tank to minimise reflections of the generated waves. This beach was tested by Banner and Peirson (2007) and could damp the low-frequency waves to less than approximately 2 % of wave amplitudes. The water depth was 0.460 m and an automatic point-gauge and solenoid valve system were used to keep the water level within ±1 mm of the set level during the experiment. The sketch of the experimental setup for deep-water waves is shown in Figure 3.1. The tank configuration was identical to that used by Banner and Peirson (2007) except that a movable wind tunnel was mounted on the tank to generate wind on deep-water waves.

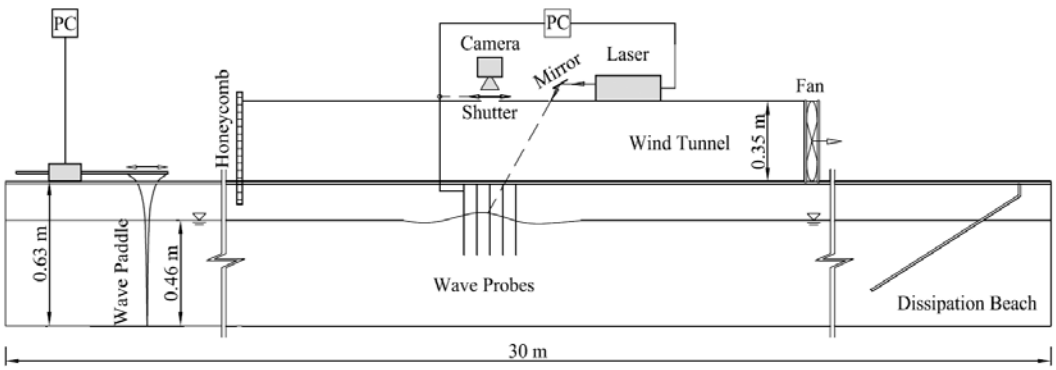

Figure 3.1- Sketch of the experimental setup (not to scale) used in deep-water wave study. The details of the dimensions and distances are given in the text.

The length of the wind tunnel was 7.5 m and the roof of the tunnel was 0.5 m above the still water surface. At the upwind end of the tunnel, an adjustable honeycomb flow guide of 50 mm thickness and composed of 8 mm diameter tubes was installed to establish a uniform air flow within the wind tunnel when air was drawn through the tunnel by a fan at its downstream end. Wind intensity was controlled by varying the fan input voltage using a metered Variac (Figure 3.2). The wind speed was measured on the centreline of the tunnel approximately 4.8 m downwind of the inlet and 0.25 m above the still water level using a pre-calibrated hot probe air velocity meter (Velocicalc model 8347). Paddle-generated waves under wind forcing were investigated for different wind speeds in the range of 1.0 m s^{-1} to 2.2 m s^{-1}.

Figure 3.2- The fan and adjustable honeycomb flow guide used to establish a uniform air flow in the 0.6 m flume.

3.1.1.2 Transitional depth waves

The flexible wave paddle was replaced with a piston paddle system for transitional depth conditions. Three water depths d = 0.35 m, d = 0.22 m and d = 0.19 m were selected to generate transitional to shallow water waves. The change in depth created the possibility of reflections from a sluice gate behind the paddle. To minimise the reflections from the sluice gate behind the paddle, flexible reticulated polyester-urethane foam was positioned between the paddle and the gate. The sketch of the experimental setup for

shallow-water experiment is shown in Figure 3.3. The tunnel roof height was reduced to 0.12 m for optical reasons. No wind was used during the transitional depth testing. The fan and the honeycomb flow guide were removed from the wind tunnel.

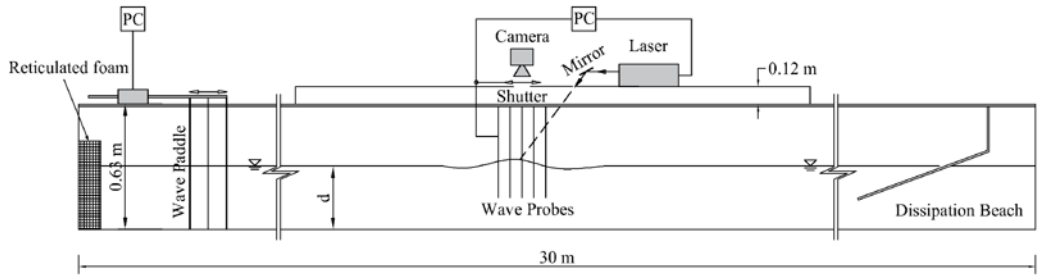

Figure 3.3- Sketch of the experimental setup (not to scale) used in shallow-water wave study.

3.2.2 Wave Basin

The wave basin was used to investigate the directional (3D) waves in deep-water in the absence of wind. The Wave basin is 29 m long, 16 m wide and 0.7 m deep with rendered walls and a solid concrete floor. For the testing described in this thesis, the basin was separated into two sections by a concrete wall 7.75 m from and parallel to one of the basin sidewalls. Also, another concrete wall was constructed across the basin 2.8 m from and parallel to the basin endwall. The dimensions of the wave basin which was used for the current study were 26.2 m long by 7.75 m wide. The plan of the wave basin and general experimental layout are shown in Figure 3.4. The wave basin width was identical to that used by Allis (2013). Also, a movable trolley was located in the wave basin to mount the measurement equipment at the centre of the trolley. The water depth was maintained at 0.550 m ±2 mm by an automatic point-gauge and solenoid valve system. A platform and an enclosed control room were mounted over the 2.8 m wide channel behind the paddle units.

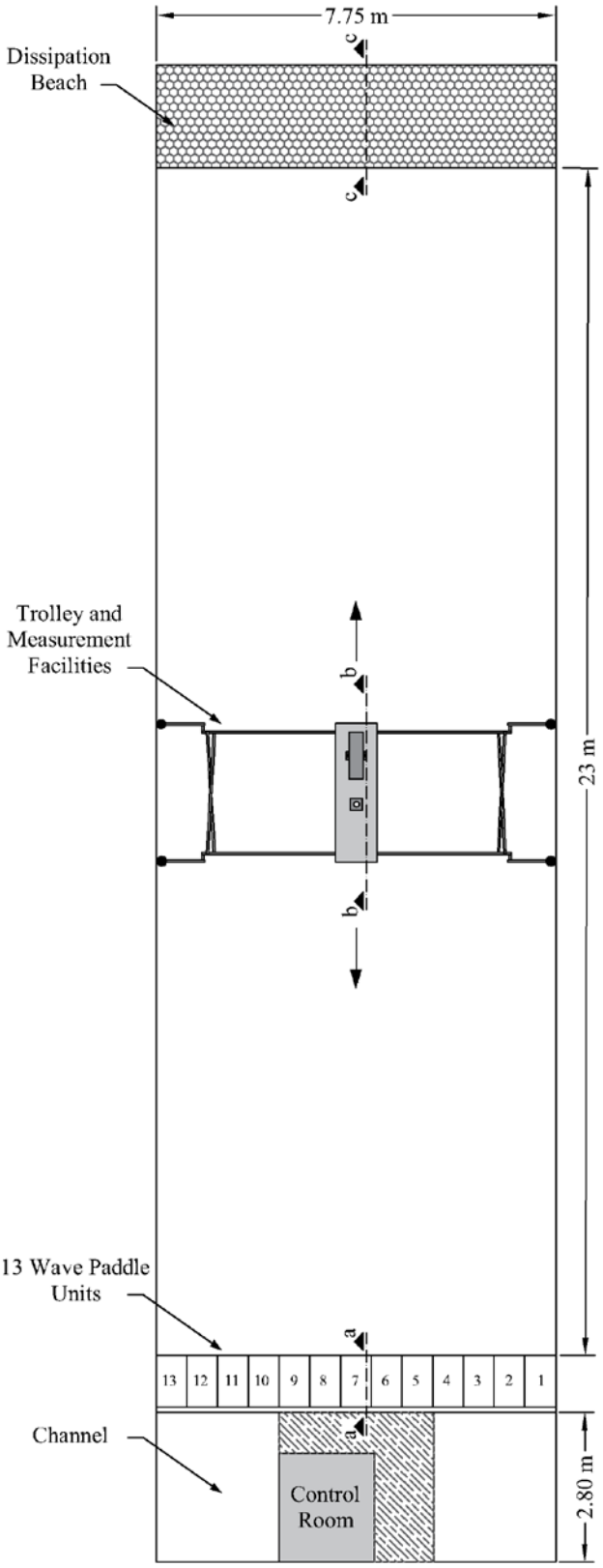

Figure 3.4- Plan view of the wave basin and experimental setup used in directional deep-water wave study.

A wave paddle system containing 13 wave paddle units was installed at one end of the wave basin to generate directional waves (Allis, 2013, § 3.2.1). This directional wave generator is called 'Snake Paddle'. The wave paddles were cantilevered flexible plates and controlled by a computer using a custom LabVIEW development. The National Instruments Data Acquisition PCI6221 card was used to send the signals to the actuator. The cross section a-a of Figure 3.4 shows the paddle unit cross section and the wave basin wall behind the paddle units (Figure 3.5). As shown in the figure, the flexible reticulated foam with the thickness of 0.1 m was located between the wall and the paddle units to reduce the reflections from the wall behind the wave paddles.

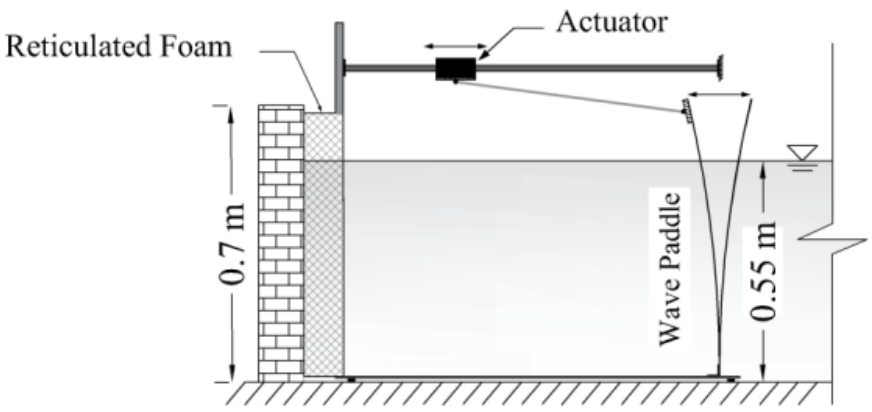

Figure 3.5- Cross section a-a showing the sketch of wave paddle units in the wave basin.

An absorbent beach was installed at the other end of the wave basin to minimise the wave reflections. The beach was constructed using perforated curved metal plates with the radius of approximately five meters. One end of the panel was located on the wave basin floor and the other end was located on the braces. The height of the braces was 0.57 m such that the top part of the beach was 0.03 m out of the water and near horizontal. The cross section of the dissipation beach is shown in Figure 3.6. The 0.1 m thick flexible reticulated foam was also positioned between the wall and the braces to control the possible reflections from the wall behind the beach.

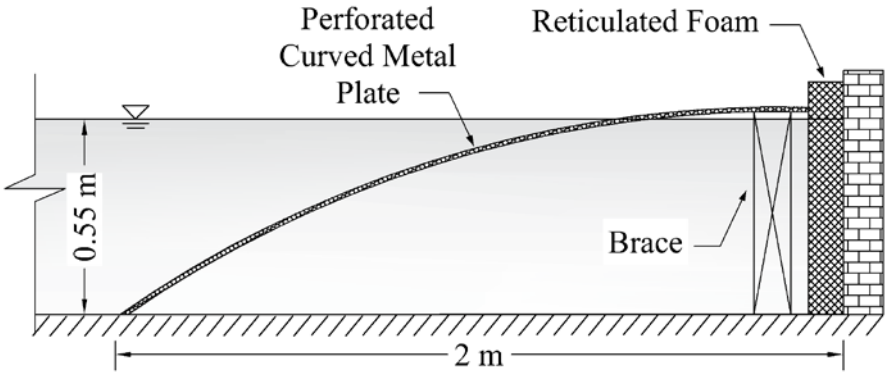

Figure 3.6- The cross section of the dissipation beach in the wave basin (Figure 3.4, section c-c).

One of the challenging parts of the experimental setup was installing the measurement equipment in the middle of the wave basin without having any impact on the wave profiles. For this purpose, we designed a movable trolley comprised of a rigid scaffolding frame mounted on four adjustable height jockey wheels with narrow poles. The width of the trolley across the basin was 6 m and the wheels were located at approximately 0.9 m from each sidewall (Figure 3.4). The length of the trolley (in the wave propagation direction) was 2.3 m and the middle section of the wind tunnel with the length of 2.4 m was positioned on the trolley at the centre of the wave basin. The cross section of the trolley and the general measurement apparatus layout are shown in Figure 3.7.

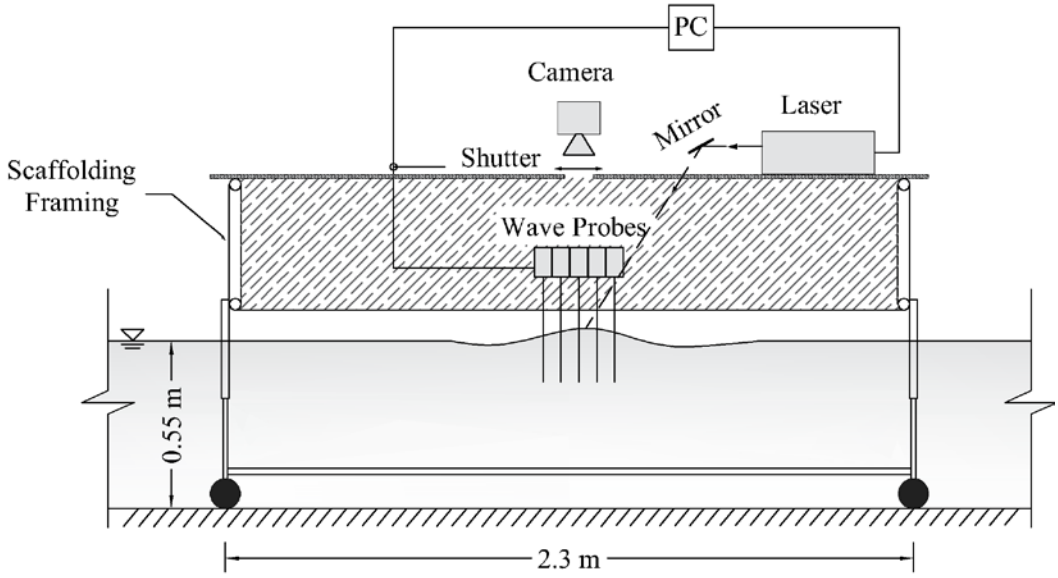

Figure 3.7- The cross section of the trolley and measurement apparatus (Figure 3.4, section b-b).

The trolley was able to move along the wave basin using stainless steel wire ropes and two hand wire rope winches. In order to move the trolley on an exact line along the basin, two jockey wheels were installed between the trolley and sidewalls at both sides of the trolley (Figure 3.4). A platform was also installed on the trolley to make an access to the measurement apparatus while the experiment was running. The photo of the trolley, horizontal jockey wheels and the platform is shown in Figure 3.8. The only elements penetration the open basin water surface were the four jockey wheel stems, 50 mm diameter, 3 m either side of the basin centreline.

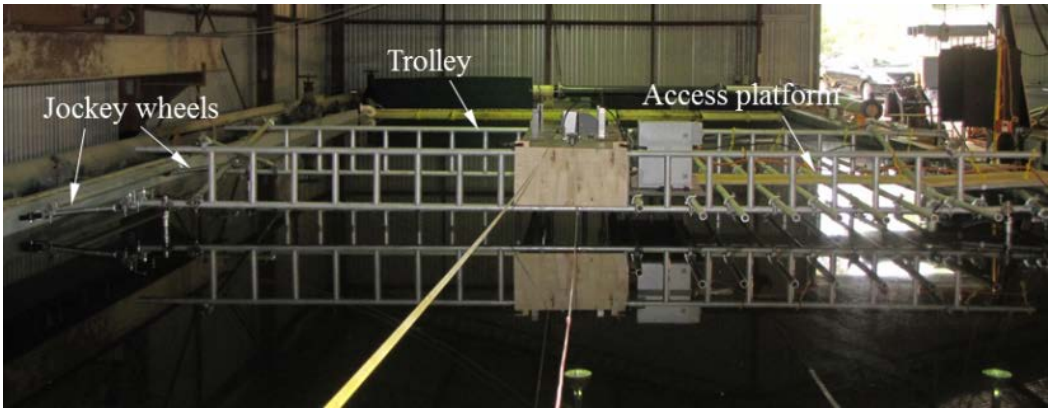

Figure 3.8- The trolley used to hold and move the measurement apparatus in the wave basin.

3.2.3 Wave probes

Capacitance wave probes were used to capture the water surface motion along the flume and wave basin. The probes were manufactured by Manly Hydraulics Laboratory in Sydney and were fitted with a 200 mm long, 0.2 mm diameter dielectric coated wire suspended within a metal frame (Figure 3.9). When the wire is partially immersed in the water, the probe produces an analogue signal in the range of ±10 volts. This signal is captured digitally using a National Instruments PCI-6225 data acquisition card at 1 kHz sample rate per channel. Probe resolution is 0.1 mm with the linearity of ±0.2 mm over the 200 mm length.

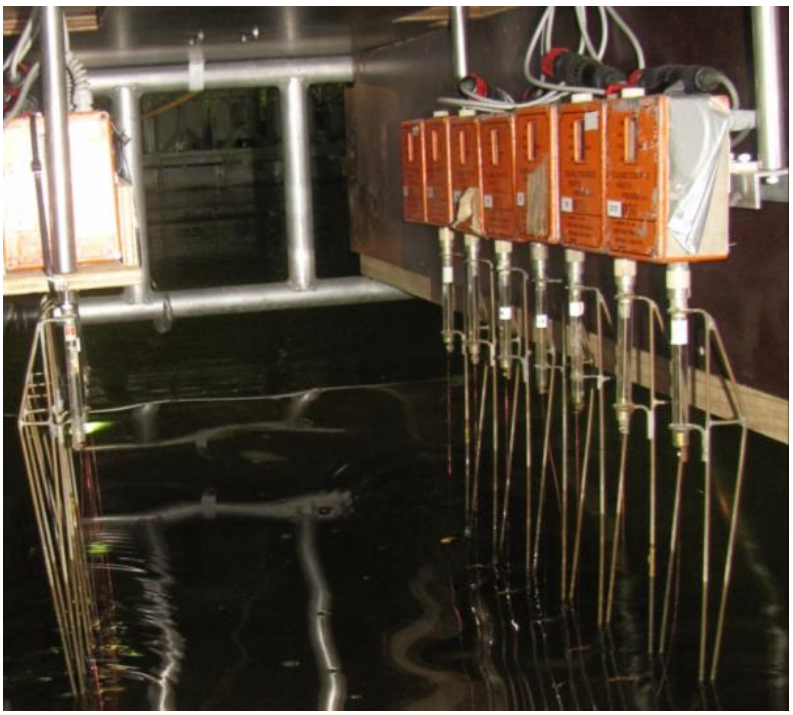

Figure 3.9- Capacitance wave probes used to record water surface elevations.

During the flume testing under wind forcing, the wave probe signal conditioning boxes were mounted outside of the tunnel with 6 mm diameter cables connecting the boxes to the 3 mm diameter, 250 mm long probe frames. This was to minimise any effect of the probes on the wind flow.

All the probes were re-calibrated at least once a week and checked before each experiment as follows. The still water level was incrementally changed by approximately 25 mm and 50 mm either side of the test SWL. Probe voltages were recorded at 1 kHz for 10 seconds for the calibration five water levels. The averaged voltages for each water surface elevation were plotted versus the water surface elevations and a linear regression line fitted. The slope of the line corresponded to the calibration factor. Figure 3.10 shows the calibration process for five of the wave probes used to capture water surface elevations in this study.

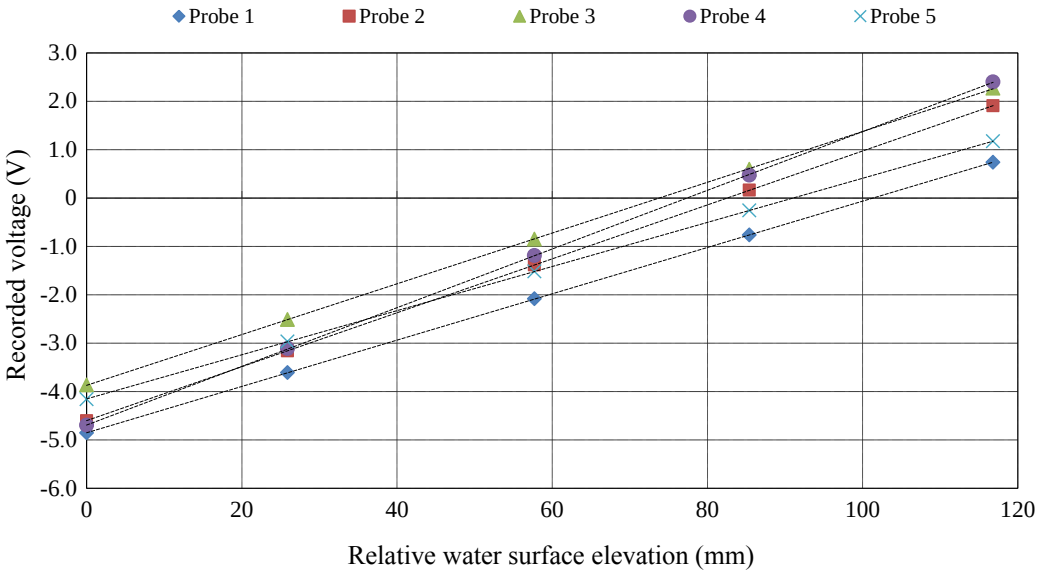

Figure 3.10- The wave probe calibration for five gauges. The symbols indicate the observed voltages at relative elevations for each wave probe with dashed lines to linear regression slope.

To verify the wave probe linearity, the R^2 value for each wave probe was checked and the probes with R^2 less than 0.999 were re-wired and recalibrated. The representative results of the calibration parameters are presented in Table 3.1 for five wave probes.

Table 3.1- Example calibration parameters for five wave probes.

Probe number	Slope (mm/V)	R^2
Probe 1	20.892	0.999998
Probe 2	17.931	0.999998
Probe 3	19.056	0.999977
Probe 4	16.490	0.999985
Probe 5	21.924	0.999995

The probes were subject to environmental laboratory noise as shown in the inset of Figure 3.11. A zero-phase 9th order low pass Chebyshev Type I filter with 0.05 dB of passband ripple and a passband edge frequency of 25 Hz was applied to remove noise. A MATLAB code was used for the post-processing filtration of measured water elevation time series. An example of raw and filtered water elevation time series measured by wave for a bimodal wave group is illustrated in Figure 3.11.

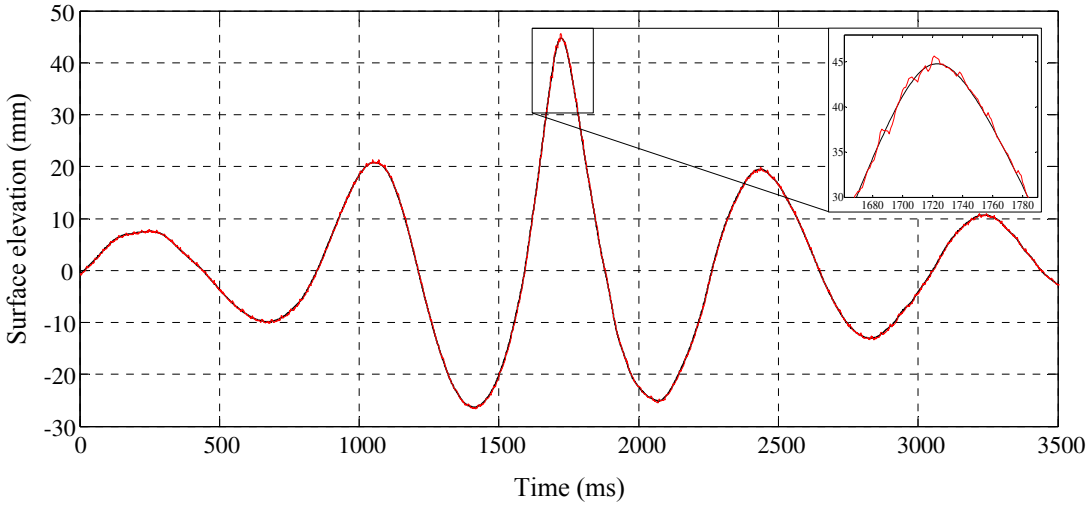

Figure 3.11- Example of raw surface elevation time series for a bimodal wave group (red line) and filtered signals using a low pass order Chebyshev Type I filter (black line). The inset on the right indicates the detail of unfiltered and filtered signal at the wave crest.

3.2.4 Laser system

An air-cooled pulsed CO_2 laser (Synrad Firestar T100) system was used to spot the water surface. A RF Power Supply converts the DC input voltage to a radio frequency (RF) output which can drive the Laser head. The laser produces an infrared light beam with the output wavelength of approximately 10.6 μm. The beam dimeter is 3.5 mm at the laser output aperture and diverges due to diffraction at an angle of 4 milliradians. The Laser head and the RF Power Supply are shown in Figure 3.12.

Synrad's UC-2000 Laser Controller was used to control and vary the Pulse width Modulation (PMW) to vary the laser output power. A National Instruments Data Acquisition (NIDAQ) PCI6221 card was applied for sending the signal to the laser using LabVIEW and the laser controller was set on the manual mode.

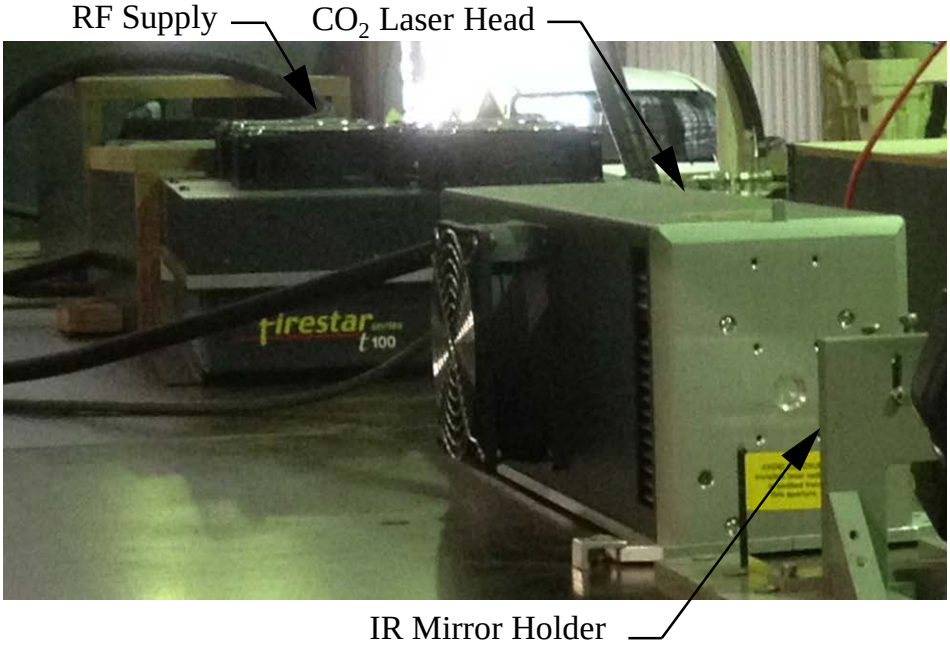

Figure 3.12- The RF supply, CO_2 laser head and the mirror holder used to irradiate the water surface.

The laser was mounted at the centre of the wind tunnel roof and aligned using an adjustable infrared range flat mirror (Figure 3.12). Pulses triggered by the controlling computer were timed to create a sequence of circular heat patches of approximately 4 mm diameter at locations just upstream of the group maximum location.

As the laser light reflections could potentially damage the camera, a computer-controlled shutter was installed underneath the camera to protect the lens and during surface irradiation, the shutter remained close. Also these reflections could cause physical or eye injuries so that before operating the laser all the uncovered area around the flume and wind tunnel were covered.

One of the challenges during the measurements in the wave basin was controlling the laser reflections as it was not possible to cover the wave basin to block the invisible lights. Therefore, when the laser was powered on, all the laboratory's doors were locked and all the TIV system was controlled remotely from an enclosed control room (Figure 3.13).

Figure 3.13- The enclosed room to control the TIV system remotely while the laser was operating in the wave basin.

3.2.5 Thermal imaging camera

A thermal (infrared) imaging camera (Flir T420) was used to acquire images of heated patches on the tank water surface through a shuttered window with the 25°×19° field of view at 30 frames per second (Figure 3.14). The IR resolution of the camera is 320 × 240 pixel.

Figure 3.14- Flir T420 thermal imaging camera for to acquiring images of heated patches on the water surface.

The camera detects the infrared energy and converts the energy to electrical signals and then converts the signals into a thermal image which shows the temperature of an object. Warmer objects are brighter as they generate more heat and more infrared light.

For the TIV system using hot water, the camera was mounted on the trolley at the centre line of the tank and central to the wave probe arrays and for CO_2 system, it was mounted looking down at the centre of the wind tunnel roof. The thermal images were calibrated using a metal grids placed within the field of view. The physical resolution of the thermal imager was approximately 0.66 mm per pixel at still water level.

3.2.6 Ultrasonic sensor

An ultrasonic sensor (Microsonic mic +35) was employed in the TIV system to track the movement of the shutter (Figure 3.15). Ultrasonic sensors transmit the sound waves to a target object and then receive the reflection of the waves from the object. The distance from the head of the sensor to the target is calculated by measuring the time which takes for echo of the sound to reflect back to the sensor.

Figure 3.15- Microsonic mic +35 ultrasonic sensor for tracking the shutter located underneath the infrared camera.

The sensor was installed in front of a board attached to the shutter and the movement of the shutter was recorded using the ultrasonic sensor (Figure 3.16). The sensor was synchronised with the wave probes and they were recorded data exactly at the same time.

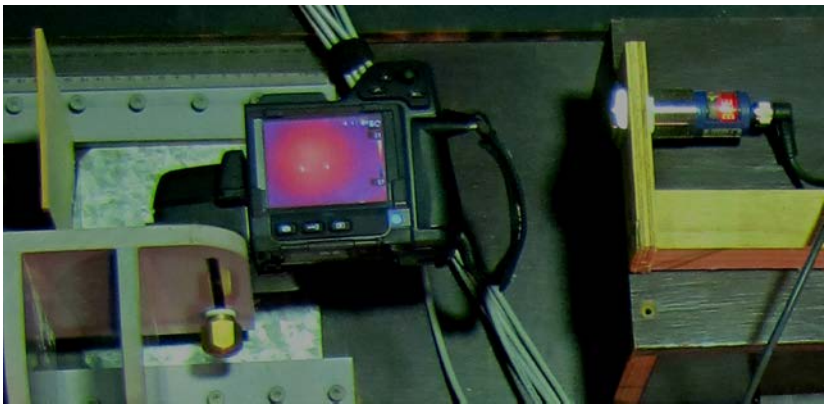

Figure 3.16- The ultrasonic sensor in front of the board connected to the shutter.

3.3 Initial wave group conditions

This experimental study was primarily carried out to investigate the breaking processes of wave groups. However, monochromatic wave structures were used to validate the thermal image velocimetry techniques which are detailed in § 3.4. The monochromatic waves were generated for low and moderate steepness 2D waves using:

$$x_p(t) = A_p \sin(\omega_p t) \tag{3-1}$$

where,

x_p: paddle motion

t: time

A_p: proportional to the piston amplitude

$\omega_p = (gk \quad \tanh(kd))^{1/2}$: paddle angular frequency

$k=2\pi/\lambda$: wavenumber

λ: wavelength

d: still water depth.

The wave packets generated by the paddle were selected to correspond to the cases used by Banner & Peirson (2007). Both a bimodal spectrum with developing Benjamin-Fier side bands instabilities around the peak frequency (called here Class 2, Benjamin & Feir, 1967) and frequency modulation wave packets (called here Class 3; Longuet-Higgins, 1974) were considered in the present study for unidirectional and directional waves.

The bimodal initial spectrum (Class 2) wave packets are defined by two superimposed frequency components as follows:

$$x_p(t) = A_p\left(a_0 \cos(\omega_{p0} t + \phi_{m0}) + a_1 \cos(\omega_{p1} t - \frac{\pi}{18} + \phi_{m1})\right) \tag{3-2}$$

where a_0 and a_1 are dimensionless amplitudes corresponding to the two frequency components and Φ_m is the paddle phase component for each wave paddle (m).

In this experimental investigation, two cases were selected for Class 2 wave packets where ω_{p0} was specified as 9.383 rad s^{-1} with ω_{p1} taking values of 8.043 rad s^{-1} and 8.530 rad s^{-1} for $N = 3$ (C2N3) and $N = 5$ (C2N5) waves, respectively.

The chirped (Class 3) wave packets were generated using:

$$x_p = -0.25A_p\left(1+\tanh\frac{4\omega_p t}{N\pi}\right)\left(1-\tanh\frac{4(\omega_p t-2N\pi)}{N\pi}\right)\times\sin\left(\omega_p(t-\frac{\omega_p C_{t2}t^2}{2})+\phi_m\right) \tag{3-3}$$

where

N: number of waves in a wave group produced by the wave paddle

C_{t2}: the chirp rate of the linear modulation.

In this study, the non-dimensional chirp rate of $C_{t2} = 0.0101$ was used for three Class 3 wave packets with $N = 5$, 7 and 9 (denoted hereafter as C3N5, C3N7 and C3N9).

The paddle phase for 2D waves was $\Phi = 0$ and for 3D waves in the wave basin it was determined using linear wave theory for directional waves as follows:

$$\phi_m = k_p(x_f\cos\theta_{fm} + y_f\sin\theta_{fm} + y_m\sin\theta_{fm}) \tag{3-4}$$

where $k_p = \omega_p/g$ is the wavenumber at the paddle, x_f and y_f are the position of the focal point and y_m is the position of each wave paddle (Figure 3.17). θ_f is the focal angle for each paddle (m) and defined as:

$$\theta_{fm} = \tan^{-1}\left(\frac{y_m - y_f}{x_f}\right) \tag{3-5}$$

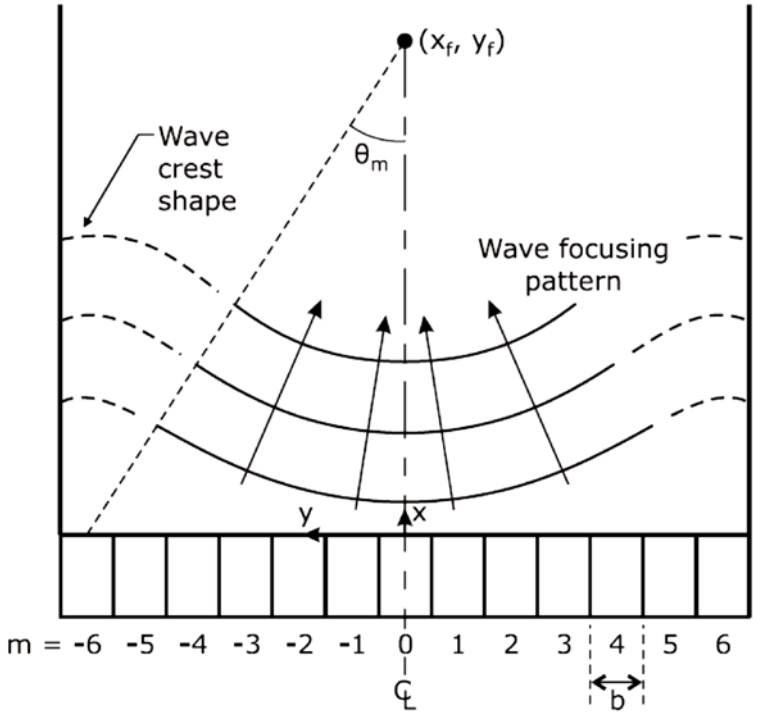

Figure 3.17- Schematic of 13 component wave paddle for convergent wave focusing (Allis, 2013).

The experiment for directional waves was conducted for θ_f= 42.4° and θ_f= 17.6° based on two focal lengths along the wave basin centreline (y_f=0) i.e. x_f= 10 m and x_f= 25 m, respectively.

3.4 TIV techniques

The most challenging aspect of the measurements was capturing the horizontal water particle velocities at the wave crest point. The thermal image velocimetry (TIV) techniques were developed to measure the surface wave particle velocity using infrared imagery using two sources of heat: hot water droplets and a CO_2 laser. The system consisted of heat sources, an infrared imaging camera, a computer-controlled shutter, an acoustic sensor, synchroniser and a computer controlling the system components.

3.4.1 TIV system using hot water

Initially a thermos flask was used to deposit hot water droplets on the water surface in the 0.6 m flume with low (<10) Weber number which is defined as:

$$W = \rho u^2 D/\sigma \tag{3-6}$$

where ρ is the droplet density, u is the mean droplet impact velocity, D is the droplet diameter and σ is the surface tension.

A trolley was used to move all the apparatus along the tank. A thermos was mounted at the centre line of the flume with two linear arrays of wave probes just inside each of the tank side walls on the trolley (Figure 3.18). Five wave probes were located at each side of the tank with the spacing of 100 mm. To adjust the time interval between droplets and the dimension of the droplets, a valve and nozzle were installed on the thermos. For group waves, hot droplets were laid down upstream of the group maximum location.

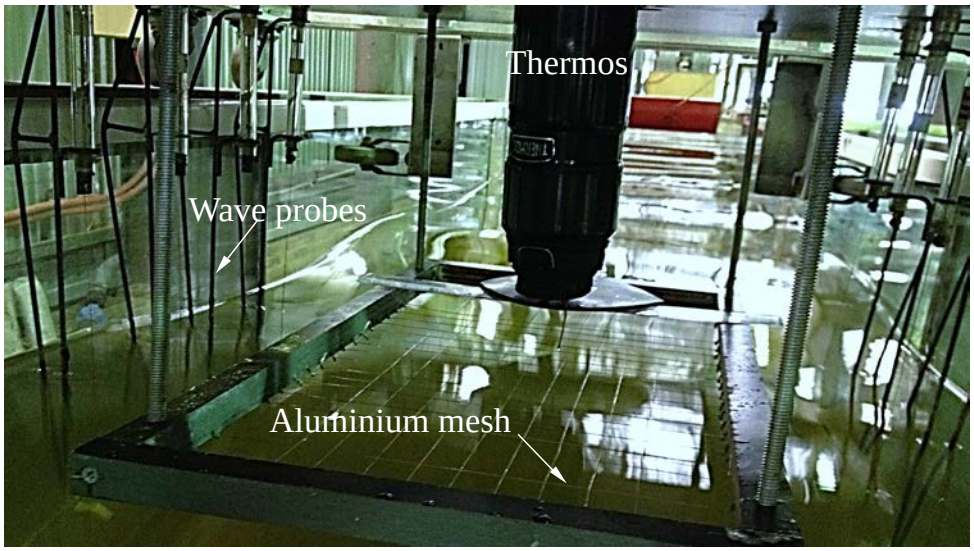

Figure 3.18- Laboratory deployment of instrumentation: thermos, wave probes and aluminium mesh to calibrate camera images

The thermal camera was mounted looking down on the trolley at the centre line of the tank and central to the wave probe arrays to observe the tank surface. An aluminium mesh was installed in the field of view of the camera

(Figure 3.18). To adjust the level of the grids for calibrating the images, the mesh frame was connected to the trolley using four adjustable bars.

The water surface velocity was determined by tracking the leading edge of the heated patch in successive video frames. Low steepness monochromatic waves with the paddle frequency and water depth of $\omega_p = 8.976$ rad s^{-1} and $d = 0.46$ m were used to validate the TIV technique. An exemplary displacement of the heated patch at the crest of monochromatic waves for two successive frames is shown in Figure 3.19. The images of the surface were captured at the rate of 30 frames per second. By differentiating the heated patch positions with time, a sequence of surface water velocities could be determined.

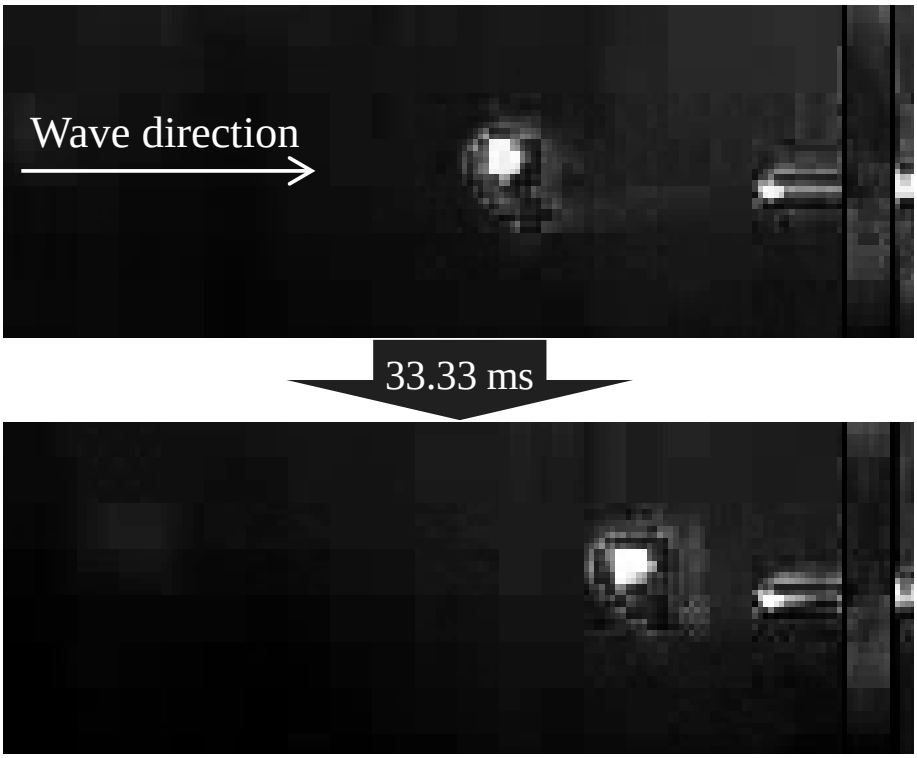

Figure 3.19- Tracking the heated spot on the wave crests of a monochromatic wave for two successive frames using infrared imagery to measure the surface particle velocity. The stationary white features at the right side are images of the nozzle head used to locate hot droplets on the water surface.

The wave parameters were measured using the two arrays of wave probes and linear wave theory was used to calculate the corresponding wavenumber k. Measured wave characteristics were compared with linear wave theory predictions of the surface water velocity (u_{sL}) at the wave crest and crest speed (C_L) obtained based on the wave frequency and have been presented in Table 3.2.

Table 3.2- The locally measuring wave steepness (ak), linear wave crest speed (C_L) and water surface velocity (U_{sL}) were estimated using linear wave theory for a monochromatic paddle frequency ω_p = 8.976 rad s^{-1}. These are compared with the water surface velocity (U_s) measured using the TIV technique and crest speed (C) obtained from the wave probe records.

	$a.k$	C (m/s)	C_L (m/s)	U_{sL}=$a.k.C$ (m/s)	U_s (m/s)
Average	0.0743	1.121	1.092	0.083	0.085
Standard Deviation	0.0005	0.014	-	0.001	0.002

The results of this measurements showed that this TIV technique can be used to measure the water surface velocity with an accuracy better than ±2.5 %.

A Class 3 wave packet (N = 7) was selected for the preliminary tests. As the droplets lost their thermal signatures quickly, it was necessary to deposit each droplet just before arrival of the wave crest. The investigation indicated that the heated patch was trackable for non-breaking waves and the surface water velocity could be measured at the wave crest point. Figure 3.20 shows the displacement of the heated spot at the crest of a non-breaking C3N7 wave packet for two successive frames.

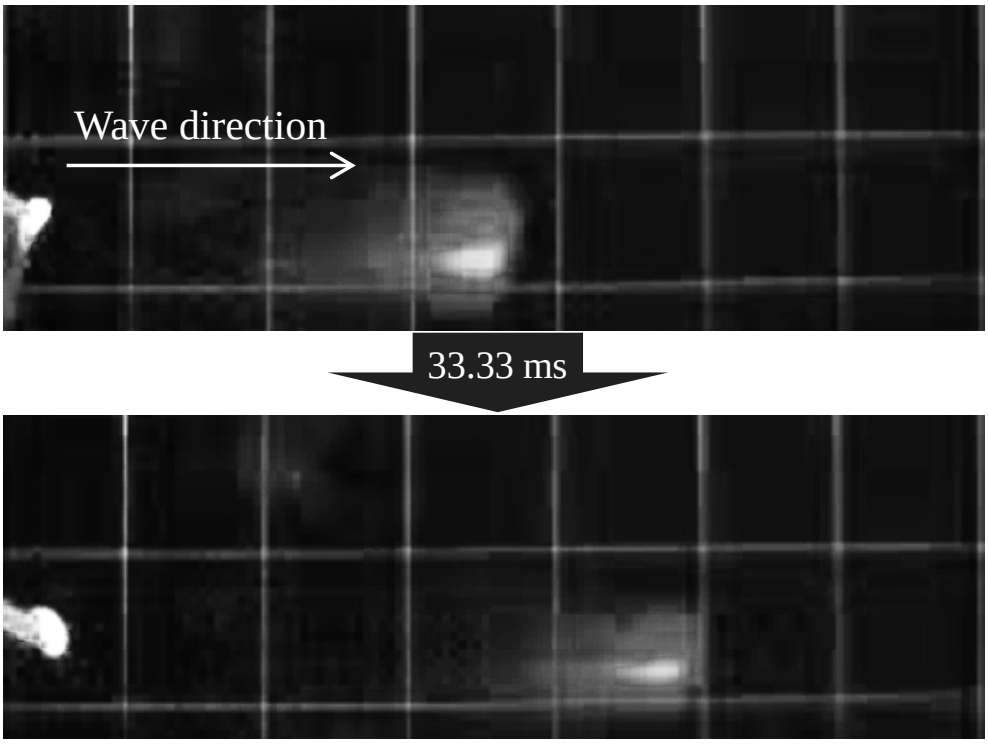

Figure 3.20- Tracking the heated spot on the wave crests of a non-breaking C3N7 wave packet for two successive frames using infrared imagery to measure the surface particle velocity.

The experiment was conducted for breaking waves and it was found that the droplets were subducted by the spilling region and it was not possible to track those spots on the water surface. Further, in the presence of wind-forcing, the hot droplets were not trackable as they had lost their heat before reaching the water surface. The TIV method using the Thermos was not able to synchronise the droplets with crest point arrival making it impossible to reliably capture the crest surface velocities for grouped waves. Therefore, the CO_2 laser and a synchronising system were adopted.

3.4.2 TIV system using CO_2 laser

A CO_2 laser (Synrad Firestar T100) system was developed to irradiate the water surface. The laser was mounted at the centre of the wind tunnel roof to produce heated circular patches with a diameter of approximately 4 mm upstream of the group maximum location (Figure 3.21). The IR flat mirror

was installed on an adjustable holder in front of the laser head to reflect the laser light on to the water surface.

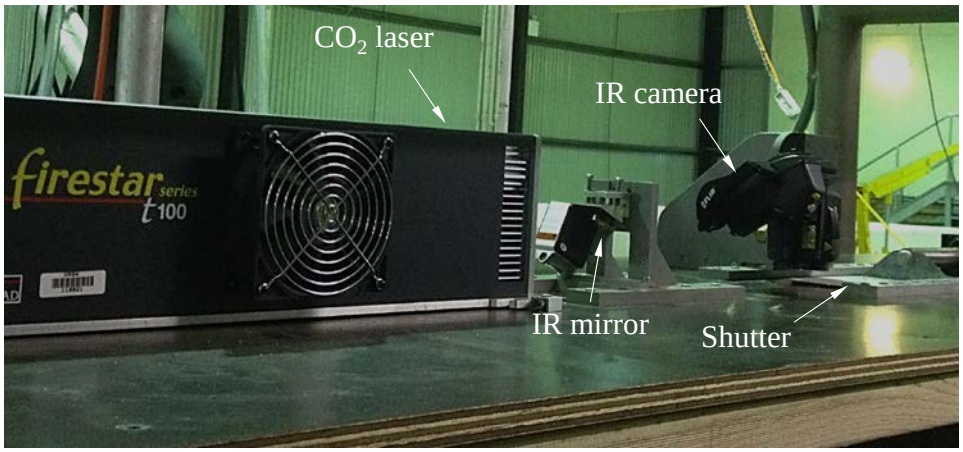

Figure 3.21- Laboratory deployment of instrumentation: CO_2 laser system, adjustable IR mirror, infrared imaging camera and computer-controlled shutter mounted on the wind tunnel. Note that the Thermos and calibration mesh were removed once the laser system was deployed.

Pulses triggered by the controlling computer were timed to create a sequence of circular heat patches at locations just upstream of the wave crest for group maximum location and wave crest for monochromatic waves. Surface reflections could potentially damage the thermal imaging camera used to acquire images of the moving heat patches. Consequently, the computer-controlled shutter remained closed during surface irradiation.

Validation was undertaken by applying the TIV technique to monochromatic waves of modest steepness and frequency 10.472 rad s^{-1}. The water depth and the paddle amplitude for the validation case were d = 0.23 m and A_p = 0.0052 m. Measured wave characteristics were compared with linear wave theory predictions of the surface water velocity (u_{sL}) at the wave crest and crest speed (C_L) obtained based on the wave frequency. The comparison is presented in Table 3.3. As shown, the measurements and linear theory agree within 1 %.

Table 3.3- Measurements verifying the TIV technique. Using a monochromatic paddle frequency ω_p = 10.472 rad s^{-1} and the locally measuring wave steepness (ak), linear wave crest speed (C_L) and water surface velocity (U_{sL}) were estimated using linear wave theory. The water surface velocity (U_s) was measured using the TIV technique and crest speed (C) obtained from the wave probe records.

	ak	$C\ (m/s)$	$C_L\ (m/s)$	$U_{sL}\ (m/s)$	$U_s\ (m/s)$
Average	0.1337	0.9235	0.9265	0.1430	0.1440
Standard Deviation	0.0034	0.0104	-	0.0041	0.0033

The most challenging measurements were determining the crest surface velocities at the crest points. This required ensuring that the position of heat patches coincided with the crest maximum concomitant with group maximum occurrence. Consequently, the sequence of heat patches had to be initially positioned on the surface, allowing for their subsequent wave orbital transport to the immediately vicinity of group maximum. Trial and error was used to achieve this.

Also, the temperature of the heat patches decreased with time. This required careful minimisation of the measurement duty cycle and careful selection of those thermal image sequences in which the thermal patches remained clearly defined. The range of laser duty cycles for different wave packets was selected between 5 to 10 ms in this study.

The TIV technique using the CO_2 laser improved the technique significantly for both breaking waves and wind-forced waves. Nonetheless, trial and error iteration was required to ensure that the position of heat patches coincided with a crest maximum event. The heated patches produced by the laser remained on the water surface longer than the droplets and were much more compact (approximately 4 mm in diameter). This allowed us to measure the water surface velocities before and after a crest maximum event as well as crest surface water velocity. The movement of a single heated patch on a

C3N7 breaking wave is presented in Figure 3.22. In the figure, the location of the crest maximum is at the centre of the image and during the measurement, the camera was stationary.

In Figure 3.22, the first image shows the heated patch just before the breaking onset. Images (*b*) and (*c*) present the patch 33.33 ms and 66.66 ms thereafter. By leading edge of the patches in successive frames and having the time between each frame, the water surface velocities could be calculated. After measuring the fluid velocities at the wave surface during the transit of a crest maximum event, these velocities could be interpolated in time to obtain a velocity at the crest that was immediately local in space to the crest maximum location.

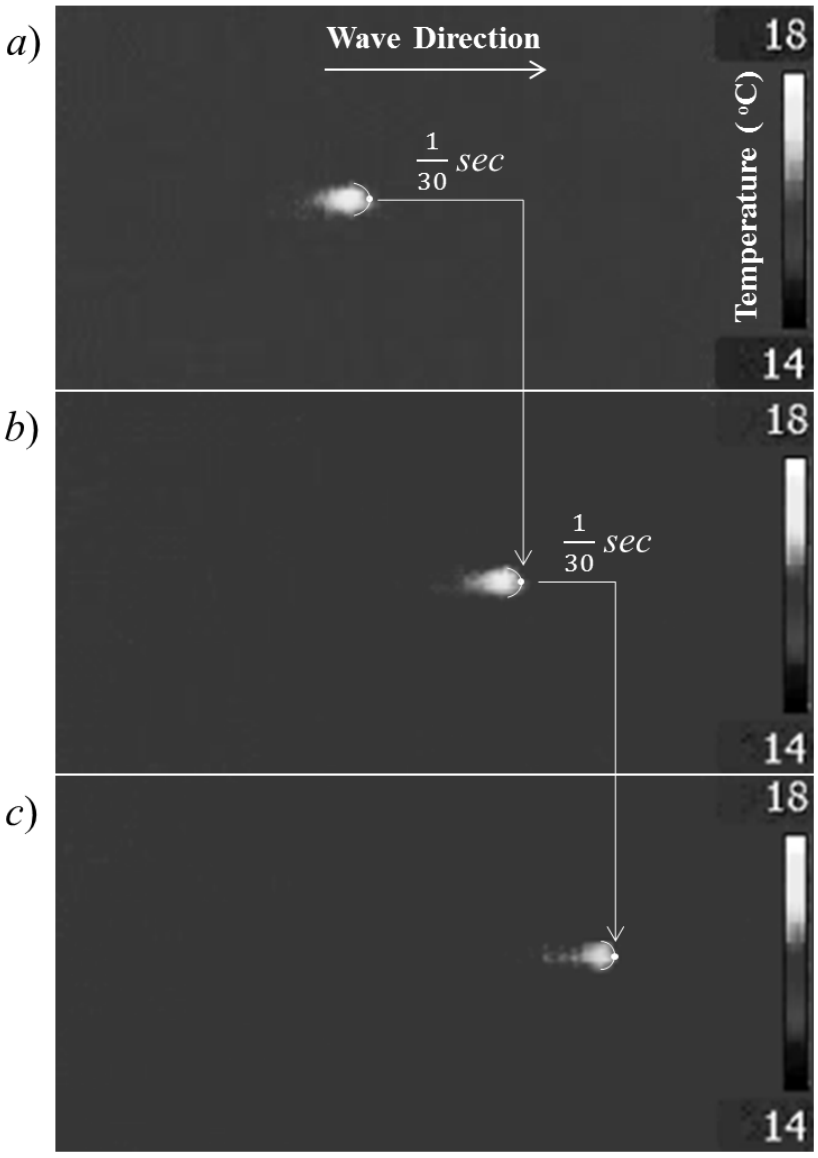

Figure 3.22- Tracking the heated patch on the crest of a breaking wave at the location of crest maximum elevation for three successive frames.

3.5 Method

Prior to each experiment, the tank water surface was cleaned by generating waves for approximately 1 hour at the beginning of each day. Any surface slick material was transported to the dissipating beach at the far end from the wave generator. Once the water surface had been cleaned, the wave probes were immersed into the tank for approximately 1 hour to ensure that

their signals were stable. The tank surface was inspected regularly to ensure that it was not contaminated with any slick material. Tank water temperatures were recorded before and after each experiment.

To avoid the uncertainty associated with capturing wave breaking onset events with their attendant very short time scales (Duncan *et al*., 1999), this present study identified the threshold for wave breaking as follows. Using the approach of Rapp and Melville (1990) and Banner and Peirson (2007), the rate of energy convergence at the point of initial wave breaking was systematically increased. Repeat observations of the wave groups transitioning through the point of initial breaking revealed that two conditions could be clearly defined.

Up to a certain wave paddle forcing level, dominant waves of successive groups were observed to progress through the group envelope maximum with no observable residual disturbance of the water surface. This condition was termed the maximum recurrent or maximum non-breaking threshold, and indicated a *lower bound* to the breaking threshold. Further slight but sufficient augmentation of paddle forcing level triggered a significant change in dominant wave behaviour at the initial break point. For each successive group, a disturbance in the wave surface was observed to occur at the same fetch, characterised by a visible bulge just ahead of the wave crest (Duncan *et al*., 1999), accompanied by surface irregularity and trailing patches of capillary ripples. This condition was termed the marginal breaking condition and used to identify the *upper bound* of the breaking threshold.

3.5.1 Experimental setup

The threshold amplitudes for breaking for the wave packets described in § 3.3 were determined in the absence of wind. In addition, the thresholds for deep water 2D C3N7 wave packets were determined with wind forcing applied. The wind conditions were selected as a perturbation on the no-wind condition. To minimise possible wind-induced growth or attenuation effects,

the wind speeds were selected to match the wave speeds as closely as possible (Mastenbroek, 1996, Figure 4.5).

In each case, paddle amplitudes were incrementally increased to determine the conditions of maximum recurrence (that is, the maximum paddle amplitude at which no surface rupture was observed anywhere on the water surface) and marginal breaking (the minimum paddle amplitude at which consistent breaking was observed at the point of maximum wave group amplitude) in each case. For the wind-forced waves, as the entire system had to be completely closed while the fan was generating wind on waves, the paddle amplitudes corresponding to maximum group recurrence and marginal group breaking were determined by illuminating the tunnel and observing waves through the glass walls.

Wave motion was monitored by two linear arrays of capacitance wave probes mounted 50 mm in from each of the wind tunnel side walls. To minimise any effect of the probes on the wind flow, the wave probe signal conditioning boxes were mounted outside of the tunnel for wind-forced wave experiments using 6 mm diameter cables connecting the boxes to the 3 mm diameter, 250 mm long probe frames.

The fetches of the group maximum were carefully recorded. The fetch is the horizontal distance from the wave generator to the observation point. Group maximum fetches (and therefore the fetch of marginal breaking) increased systematically with the number of waves in each group. Once the group maximum fetch had been determined, the measurement equipment was located over this point. So that, the central probe of each set of wave probes was positioned at the same fetch as group maximum fetch and the centre of the thermal imaging area, then the measurement of the local wave characteristics and surface current proceeded.

The time series of surface elevation at the location of the group maximum for maximum recurrence and marginal breaking 2D C2N3 and C3N7 wave packets in the absence of wind as well as wind-forced 2D C3N7 wave packets

in deep water are shown in Figure 3.23. The figure shows the differences of the mean steepness at breaking onset between the two classes of waves. As can be seen, only small differences can be observed in the time water level records obtained at the location of the crest maximum elevation. As shown in the insets, the implied forward face steepnesses of the marginally breaking waves are significantly higher than their corresponding maximally recurrent waves.

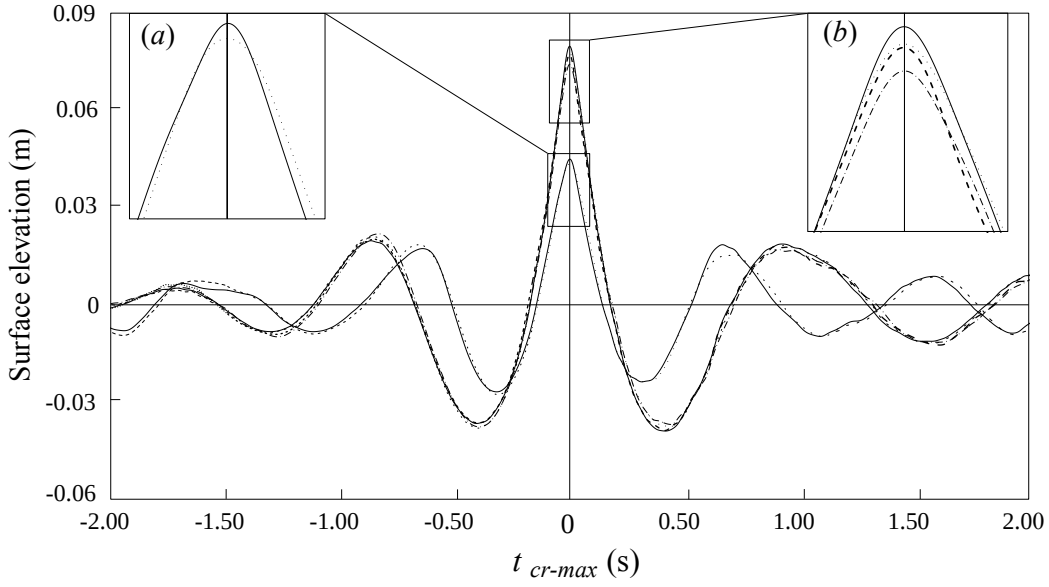

Figure 3.23- Surface elevation time series at the location of group maximum for unforced non-breaking (— — —) and marginal breaking (——) 2D C2N3 and C3N7 waves and wind-forced non-breaking (— · —) and marginal breaking (·····) 2D C3N7 waves. C2N3 are of smaller amplitudes and the crest detail is shown by the left inset; C3N7 crest detail is on to the right inset. Time (t) is referenced to the instant of the crest maximum elevation. Note the implied steeper forward face of the marginally breaking wave in comparison with its corresponding maximally recurrent wave and the differences of the mean steepness at breaking onset between the two classes of waves.

3.5.2 Local wave crest point speed (C) measurement

One of the wave probe arrays were used to measure the local crest point speeds. 5 wave probes were installed along the wave propagation with the spacing of 60 mm and 50 mm in the absence and presence of wind, respectively. Using the time-series recorded by wave probes, the time of the

dominant crest arrival at each wave probe was determined. The crests speed can be determined by knowing the space between the crests and time of each crest.

First order central differences was applied to measure the wave crest point speed at the central probe using the time derivative of the crest displacement at the location of each wave probe.

$$C_n = \frac{f_{n+1} - f_{n-1}}{t_{n+1} - t_{n-1}} \tag{3-7}$$

In order to find the wave crest speed for the upstream and downstream wave probes, 2nd order forward (3-8) and backward (3-9) differences were used, respectively:

$$C_n = \frac{f_{n+2} - 4f_{n+1} + 3f_n}{t_{n+2} - t_n} \tag{3-8}$$

$$C_n = \frac{3f_2 - 4f_{n-1} + f_{n-2}}{t_n - t_{n-2}} \tag{3-9}$$

where

C: local wave crest point speed

f: the identified wave crest fetch

n: the probe number

t: the identified wave crest time.

3.5.3 Horizontal water surface velocity (U_s) measurement

Thermal Image Velocimetry (TIV) technique was used to measure the water surface particle speeds at the crests of waves transitioning through a group maximum. By differentiating the heat patch positions with time, a sequence of surface water velocities in the vicinity of the group maximum was determined. An exemplary sequence for 2D C3N7 wave packets in the absence of wind is shown in Figure 3.24. In this figure, *X* is the position of

each point referenced to the location of crest maximum elevation (the centre of the image) and t is time, referenced to the crest maximum elevation event.

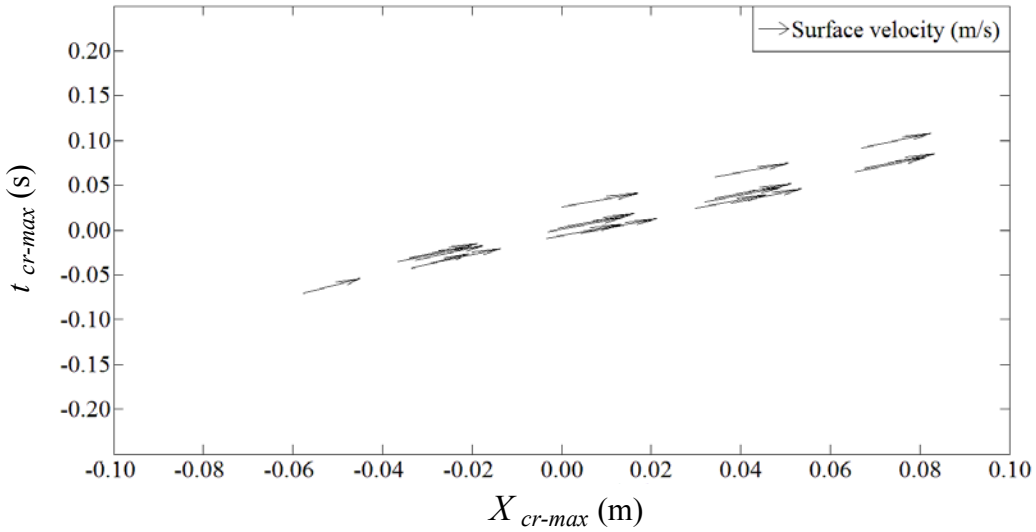

Figure 3.24- Surface water velocity (m/s) for two-dimensional marginal breaking C3N7 wave group. The arrows represent the surface water velocity where $X_{cr\text{-}max}$ is the position of each point referenced to the location of crest maximum elevation of the transiting group.

To obtain a measurement of velocity localised at the time and location of a crest maximum elevation event, the synchronised thermal imagery and wave probe records were processed as follows. First, thermal patch velocities in immediate spatial proximity of the crest maximum elevation were determined at the time of the crest maximum elevation event. It was found that the duty cycle of the coupled laser/shutter/camera/wave probe system could be synchronised to achieve five velocity measurements surrounding the crest maximum elevation location at the time of the crest maximum elevation.

These five velocities were plotted as a function of distance referenced to the crest maximum elevation position as shown in Figure 3.25. The results indicated that the maximum surface velocity coincided with the location of crest maxima in each case. A polynomial curve was fitted as shown in Figure 6 to determine the maximum water velocity U_s.

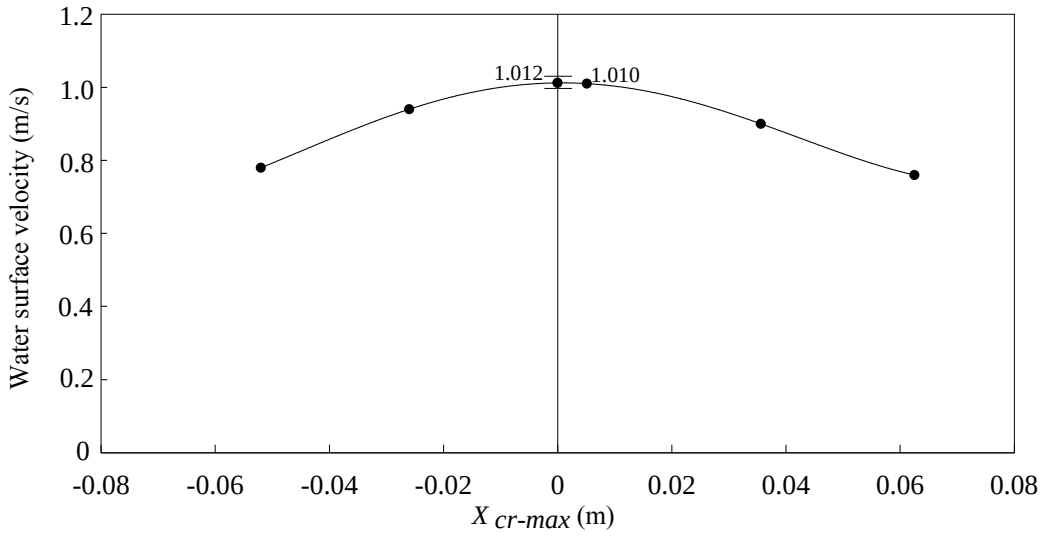

Figure 3.25- Polynomial curve fitted to water surface velocities and the interpolated velocity at the crest maximum elevation for a marginal breaking 2D C3N7 wave group. The error bars indicate the uncertainty arising from synchronisation of the TIV measurements with the wave probes. Note that the maximum velocity occurs at the wave crest point.

Due to the framing rate, the absolute time reference of the thermal imagery can only be synchronised with the wave probes with an accuracy of ±17 ms. This uncertainty in synchronisation determines an uncertainty in the wave crest point velocity determined by this process. This uncertainty was evaluated using polynomial fits to the data obtained in the vicinity of crest maximum elevation events and is indicated in Figure 3.25.

3.5.4 Measurement of B_x parameter

The ratio of the local energy flux velocity *F/E* and the local crest point speed *C* at the wave surface in the wave propagation direction (taken as the *x* direction) reduces to B_x. The breaking onset variable B_x is defined as the ratio of the horizontal water surface particle velocity U_s at the crest maximum elevation (crest point) and the local crest point speed (refer § 2.2.3).

$$B_x = \frac{U_s}{C} \tag{3-10}$$

As described in § 3.5.3, the horizontal water surface velocity at the crest point can be measured using TIV method and the array of closely-spaced wave probes was used to measure the crest point speed (§ 3.5.2). Having these two speeds at the direction of wave propagation, the variable B_x was determined for maximum recurrence and marginal breaking wave groups at their crest maximum elevation.

3.5.5 Local wave steepness measurement (S_c)

The geometry of waves was determined using an array of wave probes consists of seven wave gauges with the spacing of 100 mm along the wave propagation. The water level time series captured by the wave probes were interpolated in space to obtain the zero-crossing locations at the time of the wave group maximum. The elevation of the wave group maximum was defined as the local wave amplitude (a) and the horizontal distance between zero-upcross of crest front and zero-downcross of crest rear was used to determine the local crest half-wavelength (λ_c) and, thereby, the local wavenumber was calculated from $k = \pi \lambda_c^{-1}$. The local wave steepness (S_c) was determined as follows:

$$S_c = ak \tag{3-11}$$

The local wave steepness was measured as well as the parameter B_x for all of the cases in the present study.

3.6 Conclusion

In this chapter, the experimental instrumentation and the operation of the equipment were presented and the design of the apparatus in the 0.6 m flume and wave basin was described. The initial wave group conditions for different wave structures i.e. bimodal and chirped waves for two- and three-dimensional waves were presented.

An accurate TIV technique using a CO_2 laser and an infrared imagery which was developed for measuring the horizontal water surface velocity at the wave crest point (U_s) was described. The methods for measuring the wave crest point speed (C), the breaking onset variable (B_x) and local wave steepness (S_c) were discussed in this chapter.

In Chapter 4 to Chapter 6, the described facilities and methods are used to measure the breaking parameters for 2D and 3D waves in the absence and presence of wind.

Chapter 4

TWO-DIMENSIONAL DEEP WATER WAVES

The experimental facilities and the data acquisition equipment for two-dimensional deep-water waves were presented in chapter 3. The TIV technique where used to measure the water surface speeds at the crests of waves transitioning through a group maximum was explained in § 3.4.2 and the methodology was described in § 3.5. In this chapter, using Thermal Image Velocimetry technique the robustness of the breaking threshold is critically examined for two-dimensional grouped waves in deep-water with different group classes, spectral bandwidths and degrees of wind forcing.

4.1 Wave conditions

The threshold amplitudes were determined for five different wave packets described in § 3.3 in the absence of wind. The water depth was 0.46 m and the waves propagating along the tank were two-dimensional. For the two Class 2 cases, ω_{p0} was specified as 9.383 rad s^{-1} with ω_{p1} taking values of 8.043 rad s^{-1} and 8.530 rad s^{-1} for $N = 3$ (C2N3) and $N = 5$ (C2N5) waves, respectively. The dimensionless amplitudes corresponding to the two frequency components were defined as $a_0 = 0.473$ and $a_1 = 0.530$. The paddle frequency ω_p of 8.18 rad s^{-1} and the non-dimensional chirp rate of $C_{t2} = 0.0101$ were used for three Class 3 wave packets with $N = 5$, 7 and 9 (denoted hereafter as C3N5, C3N7 and C3N9). In addition, the thresholds for the C3N7 wave packet were determined with wind forcing applied.

The maximum wind speed investigated was 2.0 m s^{-1}. Above this speed, the thermal patches created by the laser could no longer be clearly identified and tracked within five thermal image frames captured through a group maximum occurrence event. Measurements were also undertaken at a wind speed of 1.4 m s^{-1} to verify that any observed trends were consistent. In the absence of forced waves, the TIV technique was used to measure the water surface velocities at a fetch of 3.6 m. These water surface velocities were found to be 0.065 m s^{-1} and 0.078 m s^{-1} at the wind speeds of 1.4 m s^{-1} and 2.0 m s^{-1}, respectively.

In each case as described in § 3.5.1, paddle amplitudes were incrementally increased to determine the conditions of maximum recurrence and marginal breaking. The paddle amplitude (A_p) for the different group classes and wind forcing conditions are presented in Table 4.1.

Table 4.1- Wind speed at the elevation of one quarter of the dominant wavelength above SWL ($U_{\lambda/4}$) and wave paddle amplitude (A_p) for maximum recurrence and marginal breaking wave groups.

Case	$U_{\lambda/4}$ (m/s)	A_p $(\times 10^{-2}\, m)$	
		Maximum recurrence	Marginal Breaking
C2N3	-	1.032	1.067
C2N5	-	0.846	0.863
C3N5	-	1.763	1.784
C3N7	-	1.744	1.773
C3N9	-	1.733	1.756
C3N7	1.4	1.680	1.740
C3N7	2.0	1.611	1.663

4.2 Geometric characteristics

The wave probe arrays were positioned at the fetch of wave group maximum such that the central probe was at the wave crest point. The geometric characterisations of Kjeldsen & Myrhaug (1979) local steepness S_c, crest-

front steepness ε, crest-rear steepness δ and vertical asymmetry λ' were determined at the instant of the wave group maximum for each case using the equations presented in § 2.2.1. These geometric parameters were measured for the different group classes and wind forcing conditions using seven wave probes located at one side of the tank with the spacing of 100 mm (refer § 3.5.5) and the results are summarised in Table 4.2. The table shows the averaged values obtained from each data set, with uncertainty expressed as standard error.

Table 4.2- Wind speed at the elevation of one quarter of the dominant wave length above SWL ($U_{\lambda/4}$), the average and standard deviation of measured crest steepness (S_c), crest-front steepness (ε), crest-rear steepness (δ) and horizontal asymmetry parameter (λ') for maximum recurrence and marginal breaking wave groups. The last row indicates the Kjeldsen & Myrhaug (1979) breaking threshold for each geometric parameter.

Case	$U_{\lambda/4}$ (m/s)	Maximum recurrence				Marginal breaking			
		S_c ±0.016	ε ±0.010	δ ±0.010	λ' ±0.012	S_c ±0.014	ε ±0.011	δ ±0.010	λ' ±0.031
C2N3	-	0.402	0.261	0.252	1.037	0.422	0.287	0.252	1.136
C2N5	-	0.431	0.271	0.288	0.977	0.451	0.303	0.273	1.110
C3N5	-	0.481	0.341	0.278	1.228	0.492	0.353	0.281	1.253
C3N7	-	0.469	0.324	0.277	1.171	0.480	0.327	0.287	1.142
C3N9	-	0.478	0.328	0.284	1.154	0.486	0.333	0.288	1.158
C3N7	1.4	0.460	0.286	0.299	0.957	0.476	0.304	0.301	1.011
C3N7	2.0	0.449	0.282	0.288	0.977	0.467	0.300	0.295	1.018
Kjeldsen & Myrhaug (1979)		-	<0.320	<0.260	<0.900	-	>0.320	>0.260	>0.900

The degree of the asymmetry of the crest for each wave packet in the present study has been compared with the breaking threshold of Kjeldsen & Myrhaug (1979) for different types of breaking waves in Table 4.2. As shown in the table, characterising wave steepness in this way does not yield a robust breaking criterion that distinguishes all non-breaking and breaking waves.

4.3 Threshold of the onset of breaking

The measurements of group waves showed that the wave crest points systematically slow down as they approach their crest maximum and subsequently reaccelerate thereafter, as described by Banner *et al.* (2014).

The measured crest point speeds and crest surface water velocities at the instant of the wave group maximum are summarised in Table 4.3 for each experimental case. The table shows averaged values obtained from each data set, with uncertainty expressed as standard error.

The results show a robust global threshold for the onset of wave breaking of $B_x = U_s/C = 0.835 \pm 0.005$ with an experimental uncertainty of each data point of ±0.02. This compares favourably with the value of 0.855±0.005 determined numerically by Barthelemy *et al.* (arXiv:1508.06002v1, 2015). None of the recurrent groups reach the threshold, while all marginal breaking cases exceed the threshold. This threshold is robust for different types of wave groups and shows no dependence on peak spectral wave numbers. Barthelemy *et al*. (arXiv:1508.06002v1, 2015, Figures 5 and 6) show the localisation of critical values of B_x in the context of the background levels.

Table 4.3- Wind forcing ($U_{\lambda/4}/C_0$) and the average and standard deviation of measured crest point speed (C), crest point water surface particle velocity (U_s), energy flux ratio at the crest point U_s/C, peak frequency (f_0), frequency bandwidth (Δf) and Benjamin-Feir Index (BFI) for maximum recurrence and marginal breaking waves.

Case	$U_{\lambda/4}$ (m/s)	$U_{\lambda/4}/C_0$	Maximum Recurrence							Marginal Breaking						
			C (m/s) ±0.014	U_s (m/s) ±0.017	U_s/C ±0.014	f_0 (Hz) ±0.001	Δf (Hz) ±0.004	$\Delta f/f_0$ ±0.003	BFI ±0.004	C (m/s) ±0.014	U_s (m/s) ±0.019	U_s/C ±0.016	f_0 (Hz) ±0.002	Δf (Hz) ±0.004	$\Delta f/f_0$ ±0.003	BFI ±0.004
C2N3	—	—	0.959	0.791	0.825	1.375	0.482	0.351	0.379	0.964	0.837	0.868	1.382	0.518	0.375	0.388
C2N5	—	—	0.944	0.753	0.797	1.431	0.545	0.381	0.320	0.963	0.824	0.855	1.445	0.58	0.402	0.347
C3N5	—	—	1.098	0.906	0.825	1.164	0.425	0.365	0.358	1.145	0.983	0.859	1.179	0.436	0.370	0.362
C3N7	—	—	1.187	0.922	0.777	1.106	0.412	0.373	0.347	1.224	1.040	0.850	1.108	0.433	0.390	0.350
C3N9	—	—	1.191	0.936	0.786	1.041	0.414	0.398	0.298	1.240	1.041	0.840	1.047	0.441	0.421	0.302
C3N7	1.4	0.99	1.237	0.959	0.775	—	—	—	—	1.239	1.056	0.852	—	—	—	—
C3N7	2.0	1.42	1.255	1.011	0.806	—	—	—	—	1.254	1.085	0.865	—	—	—	—

4.3.1 Waves in the absence of wind

Sample values at both maximum recurrence and marginal breaking define the bounds on the onset threshold and are shown in Figure 4.1 for waves in the absence of wind. As shown in figure, the characteristic local steepness levels at the threshold of breaking between the Class 2 and Class 3 groups are distinct.

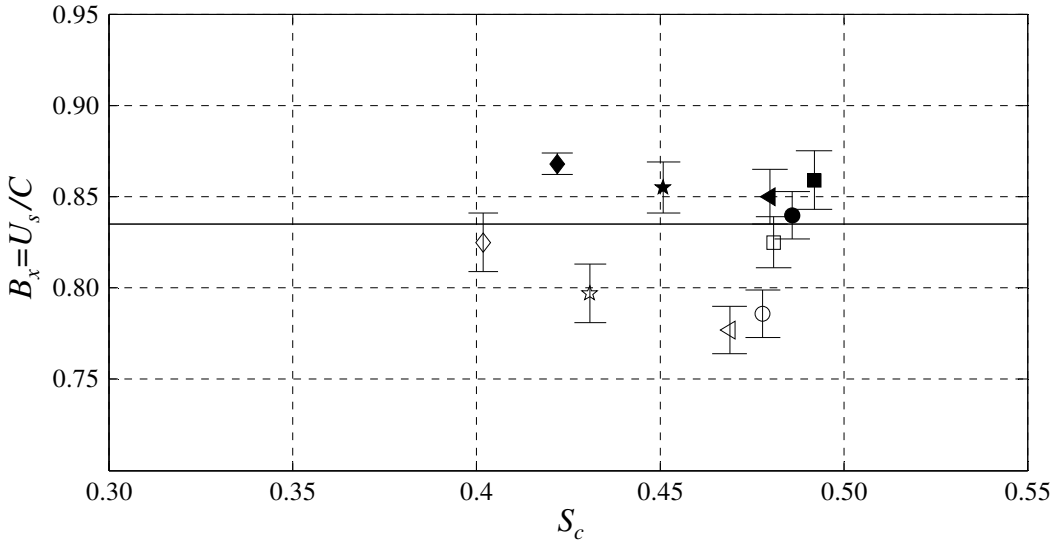

Figure 4.1- Local wave steepness S_c versus crest and surface wave speed ratio at the wave crest point $B_x=U_s/C$ for unforced waves, showing C2N3 (◇), C2N5 (☆), C3N5 (□), C3N7 (◁), C3N9 (○), with maximum recurrence waves (hollow shapes) and marginal breaking waves (solid shapes). Error bars indicate the standard deviation of the repeat measurement set (6 to 8 replicates) and the horizontal line at B_x = 0.835 is the breaking threshold.

In each case, it is the crest surface water velocity that plays the dominant role in determining the overall value of this parameter. For all wave groups, across the threshold the crest point speed remained almost unchanged between the recurrent to marginal breaking wave condition. In contrast, the surface water velocity increased significantly across the threshold.

Stansell and MacFarlane (2002) gathered similar data but without a direct method of measuring the surface velocity. They used Particle Image

Velocimetry (PIV) to capture the near-surface velocity profiles beneath waves approaching breaking onset. Smooth extrapolations of 10 points of data gathered at 5 mm grid points below the surface were used to estimate the surface velocity.

The findings of their study support this present investigation except in one aspect. Stansell and MacFarlane (2002) found that for a single case of a wave (their Wave 1) captured just before the onset of plunging breaking, the ratio of crest point water speed to crest point speed was 0.81. This is 5 % less than the breaking onset threshold reported by Barthelemy *et al.* (arXiv:1508.06002v1, 2015) and the present measurements.

Figure 4.2 illustrates the technique which Stansell and MacFarlane (2002) used to extrapolate the surface velocity for another experimental case (Wave 3). If the two velocity measurements most proximate to the surface of Wave 3 are linearly extrapolated to the surface, the estimated surface velocity would be approximately 1.66 m s^{-1}, as opposed to the value of 1.51 m s^{-1} determined by their extrapolation technique. Consequently, an extrapolation technique using the data in closest proximity to the surface may yield values more than 10% higher than they report. If a similar correction is applicable to their more extreme plunging case (Case 1, referred to above), their data would be entirely consistent with the finding of this present investigation.

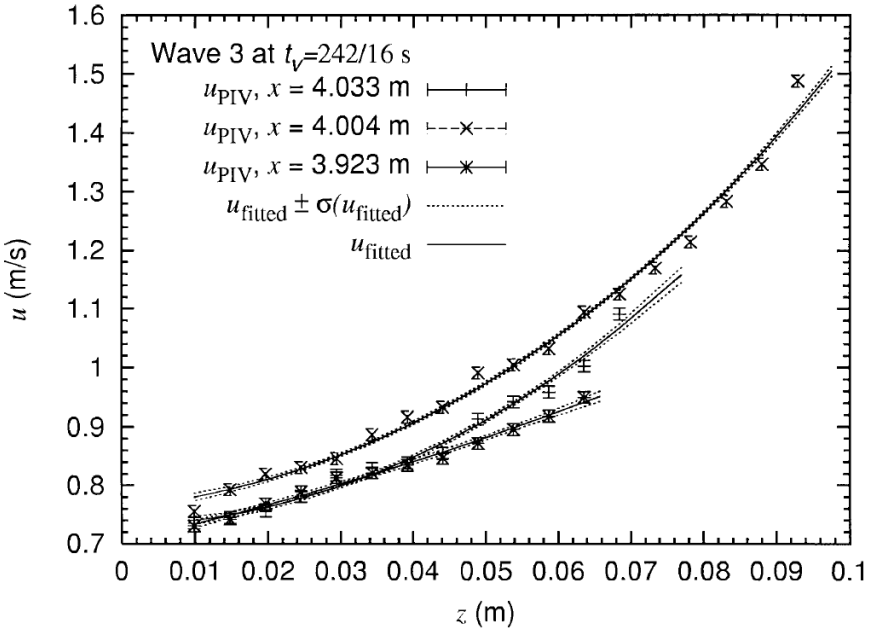

Figure 4.2- PIV measured velocities with their standard deviations along with the fitted velocities extrapolated to the positions of the fluid surface for Wave 3 by Stansell and MacFarlane (2002).

4.3.2 Waves in the presence of wind

The sensitivity of the threshold was investigated in relation to wind forcing. As shown in Table 4.3, the degree of wind forcing has been characterised in terms of the wind speed at an elevation of one quarter of the dominant wavelength ($U_{\lambda/4}$) above the mean water surface. For wind forcing $U_{\lambda/4}/C_0$ less than 1.42, the determined breaking threshold remains robust as shown in Figure 4.3.

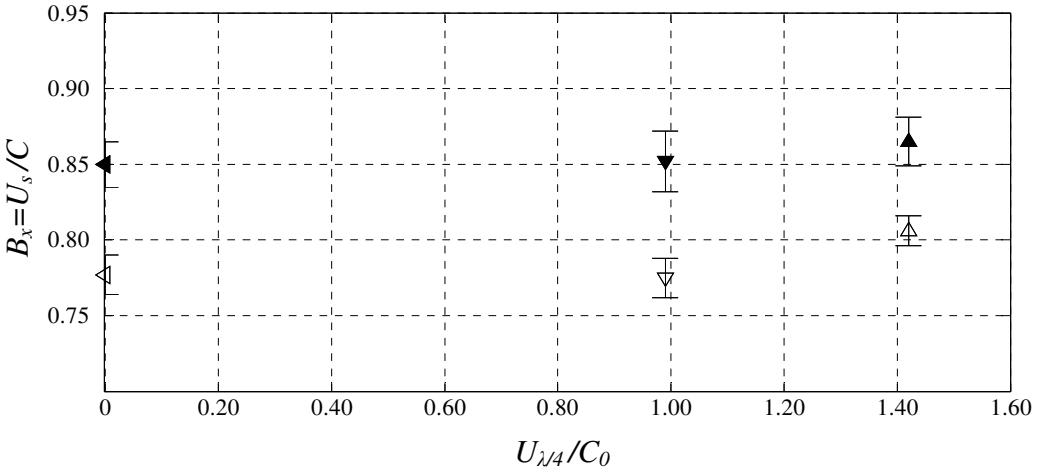

Figure 4.3- Wind forcing $U_{\lambda/4}/C_0$ versus crest and surface speeds ratio at the crest point $B_x=U_s/C$ for wind-forced waves, showing C3N7 (◁), C3N7U1.4 (▽), C3N7U2.0 (△), with maximum recurrence waves (hollow shapes) and marginal breaking waves (solid shapes). Error bars indicate the standard deviation of the repeat measurement set (6 to 8 replicates).

However, more careful examination of the C3N7 data presented in Figure 4.3 and Table 4.3 shows that as $U_{\lambda/4}/C_0$ increases from zero to 1.42, there is a slight systematic increase in the threshold in U_s/C of approximately 2.0 %. Consequently, wind has a slightly stabilising effect on the underlying wave field.

The local energy density has no contribution from any change in the surface pressure. In view of this systematic response to wind, it is useful to review the relative contributions of the three energy flux components: pressure, elevation and water speed.

Mastenbroek (1996) showed that a wave of crest steepness S_c = 0.48 with U_λ/C = 2 has an estimated wind-induced crest surface pressure perturbation less than $15ak\rho_a u^{*2}$ where ak is the mean wave steepness, ρ_a is the density of air and u^* is the friction velocity in the air. No measurements of friction velocity were taken during this present investigation but by referring to the similar conditions investigated by Hsu and Hsu (1983), friction velocities will remain less than 0.08 m s^{-1}. Consequently, the pressure perturbation due to

the imposition of wind is estimated as less than 0.05 Pa. This is less than 0.03 % of the other contributions to the energy flux.

As shown in Table 4.3, the imposition of wind perturbs the elevation contribution to the flux by approximately 6 % and the water speed component by over 10 %. The dominant perturbation to the flux ratio arises from changes in the crest water speed due to the wind. Perturbations by the wind-induced pressure itself are negligible.

4.3.3 Wave group bandwidth

Group bandwidth has been proposed as an important factor in determining the occurrence of extreme waves and so we have assessed its influence on the threshold. Therefore, the sensitivity of the threshold was also investigated in relation to group bandwidth.

Fast Fourier Transforms were used to obtain the single-sided wave frequency spectra, the peak frequency (f_0) , the frequencies associated with the half-peak energy (f_{min} and f_{max}) and frequency bandwidth ($\Delta f = (f_{max} - f_{min}) / 2$). The Benjamin-Feir Index was used for comparison with other studies (e.g. Janssen, 2003) and defined as follows:

$$BFI = \frac{\left(k_0^2 < \eta^2 >\right)^{1/2} \sqrt{2}}{\Delta f / f_0} \qquad (4\text{-}1)$$

where k_0 is the characteristic wavenumber associated with the peak frequency and $<\eta^2>$ is the variance of the average surface elevation. Linear wave theory was used to calculate the corresponding wavenumber k_0 and linear phase speed C_0 for each wave group.

We note that spectral bandwidth can change appreciably with fetch and therefore is not a robust means of characterising group wave fields. In the context of these experiments, spectral bandwidth changed by less than ±5 % within a distance of ±3 λ_0 around the group maximum location. Therefore, the fetch to initial breaking increases as the bandwidth increases. Consequently,

there is also a correlation between bandwidth and the envelope growth rate immediately prior to breaking inception (Banner and Peirson, 2007, Figure 5).

The most systematic relationship between breaking onset threshold and spectral bandwidth that emerged from the measurements is shown in Figure 4.4. As shown, the threshold systematically increases with the *BFI*. Over the range of group bandwidths considered here, the change in the threshold is only a few per cent.

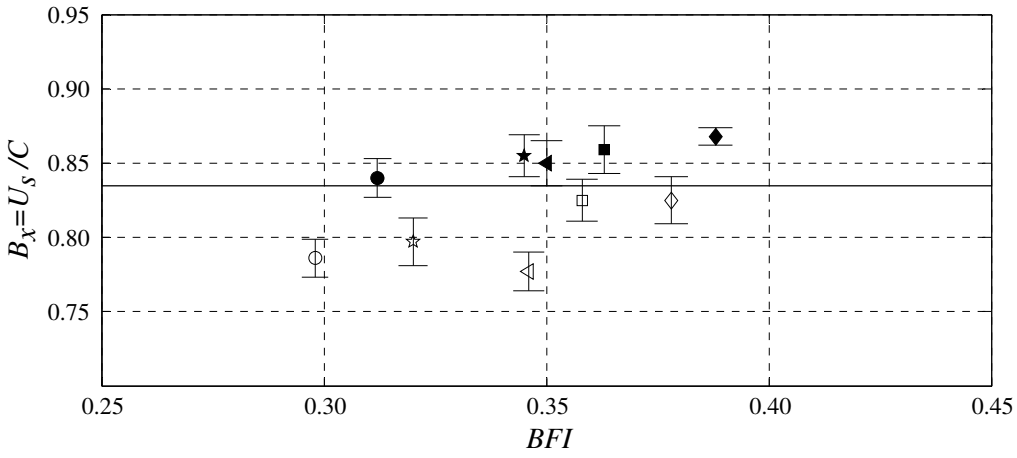

Figure 4.4- Benjamin-Feir Index *BFI* versus crest and surface speeds ratio at the wave crest point $B_x=U_s/C$ for unforced waves. The shapes are as defined in Figure 4.1. Error bars indicate the standard deviation of the repeat measurement set (6 to 8 replicates) and the horizontal line at B_x = 0.835 is the breaking threshold.

4.4 Conclusion

Thermal Image Velocimetry has been used to measure the crest surface water velocity at the crest maximum elevation of freely-propagating, unsteady deep water wave groups in the laboratory. Wave crest point speeds were determined using an array of closely-spaced wave gauges at the same instant as the crest point water velocity measurements.

A robust energy flux ratio $B_x = U_s/C = 0.835 \pm 0.005$ was found that distinguishes maximum recurrence from marginal breaking. This compares

favourably with the numerically-determined value of 0.855 ± 0.005 demonstrated by Barthelemy *et al.* (arXiv:1508.06002v1, 2015). Note that, the present experimental study encompasses different classes of wave groups exhibiting distinct characteristic steepness at the breaking threshold and was found to be robust.

It was found that increasing wind forcing from zero to $U_{\lambda/4}/C_0 = 1.42$ increased this threshold by 2.0 %. In addition, the sensitivity of the threshold in relation to group bandwidth showed that increasing the spectral bandwidth (decreasing the Benjamin-Feir index from 0.39 to 0.31) systematically reduced the threshold by 1.5 %.

These encouraging results motivated extension of this present work to shallow waters, three-dimensional breaking and field conditions. The investigations of transitional to shallow-water wave groups are presented in the next chapter.

Chapter 5

TWO-DIMENSIONAL TRANSITIONAL DEPTH WAVES

To generate water waves of transitional depth, the flexible paddle was replaced with a piston paddle system. The tunnel roof was lowered 0.23 m to improve the resolution of the TIV images. In the present chapter, the robustness of the breaking threshold which was found for deep-water waves in chapter 4 was examined for two-dimensional grouped waves in transitional to shallow water with different group classes in the absence of wind.

5.1 Wave conditions

The experiment was conducted for Class 2 waves with $N = 3$ and 5 and one Class 3 packet with $N = 9$. Three different water depths i.e. $d = 0.35$ m, $d = 0.23$ m and $d = 0.19$ m were selected for the experiment with the same paddle frequencies as deep-water waves experiment ($\omega_{p0} = 9.383$ rad s^{-1} with $\omega_{p1} = 8.043$ rad s^{-1} for C2N3 and 8.530 rad s^{-1} for C2N5 wave packets, and $\omega_p = 8.18$ rad s^{-1} and $C_{t2} = 0.0101$ for C3N9 wave packets). In addition, the sensitivity of the threshold was investigated in relation to waves of different scales. The shallowest C2N3 case with the water depth of $d = 0.19$ m was scaled using Froude scaling by changing the water depth to 0.26 m. The frequencies for the scaled waves were 8.021 rad s^{-1} and 6.875 rad s^{-1} for ω_{p0} and ω_{p1}, respectively.

The paddle amplitudes were incrementally increased to determine the conditions of the lower bound and upper bound of the breaking threshold for each experimental case. The paddle amplitudes (A_p) for the different group classes and scaled waves are presented in Table 5.1.

5.2 Threshold of the onset of breaking

The crest point speeds and crest surface water velocities at the location of the group maximum were measured for each experimental case and the summary of the results from deep to shallow water waves is tabulated in Table 5.1. The averaged values obtained from each data set, with uncertainty expressed as standard error are presented in front of the ratio of deep-water wavelength to the water depth in the second column for each case. The measured crest steepness S_c results showed that the local steepness is systematically increased from deep to transitional water. Note that the local steepness levels between the Class 2 and Class 3 groups for transitional water waves remained distinct.

The results of the measured velocities indicated that in contrast to the crest surface water velocity, the changes of the crest point speed for all wave groups from maximum recurrence to marginal breaking are insignificant. Therefore, as it was found in deep water wave experiment, the surface water velocity plays the dominant role to determine the threshold of the onset of breaking in transitional shallow water waves. The difference between crest surface velocities of marginal breaking and maximum recurrence to the crest point velocity ratio for all cases from deep to transitional water is illustrated in Figure 5.1. As seen, the changes of water surface velocity in the transition from non-breaking to marginally breaking for C2N5 waves in the transitional shallow water are greater than the others and subsequently the threshold for the breaking onset (B_x) for these cases are higher as well (Table 5.1).

Table 5.1- The ratio of linear deep-water wavelength and water depth λ_0/d, wave paddle amplitude (A_p), the average and standard deviation of measured crest steepness (S_c), crest point speed (C), crest point water surface particle velocity (U_s), ratio of the velocities at the crest point U_s/C, non-dimensional parameter F_c, wave height to water depth ratio H/d and non-dimensional parameter $\lambda \rho^{0.5} g^{0.5} \sigma^{-0.5}$ for maximum recurrence and marginal breaking waves.

		Maximum recurrence								Marginal breaking							
Case	λ_0/d	A_p	S_c	C (m/s)	U_s (m/s)	U_s/C	F_c	H/d	$\lambda\sqrt{\rho g/\sigma}$	A_p	S_c	C (m/s)	U_s (m/s)	U_s/C	F_c	H/d	$\lambda\sqrt{\rho g/\sigma}$
		(×10^{-2}m)	±0.015	±0.015	±0.021	±0.022	–	–	–	(×10-2m)	±0.018	±0.014	±0.027	±0.021	–	–	–
C2N3	1.74	1.032	0.402	0.959	0.791	0.825	5.447	0.150	245	1.067	0.422	0.964	0.837	0.868	5.703	0.158	248
	2.29	1.061	0.431	0.958	0.768	0.802	9.092	0.201	239	1.103	0.450	0.967	0.826	0.855	9.254	0.216	238
	3.48	1.175	0.440	0.887	0.726	0.819	20.866	0.303	225	1.326	0.470	0.904	0.786	0.869	22.086	0.316	226
	4.21	1.417	0.459	0.870	0.688	0.79	29.706	0.345	218	1.504	0.491	0.896	0.761	0.849	31.062	0.375	216
Scaled	4.21	2.049	0.464	1.028	0.794	0.772	29.279	0.362	300	2.094	0.495	1.055	0.886	0.839	30.844	0.373	301
C2N5	1.67	0.856	0.431	0.944	0.753	0.797	5.218	0.149	228	0.863	0.451	0.963	0.824	0.855	5.441	0.155	230
	2.20	0.885	0.435	0.95	0.743	0.782	8.146	0.190	226	0.913	0.468	0.965	0.812	0.842	8.971	0.202	227
	3.35	1.112	0.446	0.893	0.693	0.776	19.283	0.293	218	1.133	0.486	0.921	0.806	0.875	20.023	0.310	217
	4.05	1.525	0.451	0.867	0.654	0.783	28.759	0.352	213	1.564	0.499	0.903	0.782	0.866	30.076	0.378	214
C3N9	2.00	1.733	0.478	1.191	0.936	0.786	13.300	0.261	389	1.756	0.486	1.240	1.041	0.840	13.559	0.262	390
	2.63	1.762	0.482	1.209	0.955	0.790	21.084	0.322	354	1.815	0.520	1.232	1.043	0.846	21.833	0.344	360
	4.00	2.004	0.533	1.137	0.918	0.808	48.210	0.454	297	2.035	0.560	1.17	0.995	0.851	49.572	0.475	298
	4.85	2.269	0.558	1.109	0.879	0.792	67.481	0.502	266	2.274	0.574	1.123	0.963	0.854	69.188	0.515	267

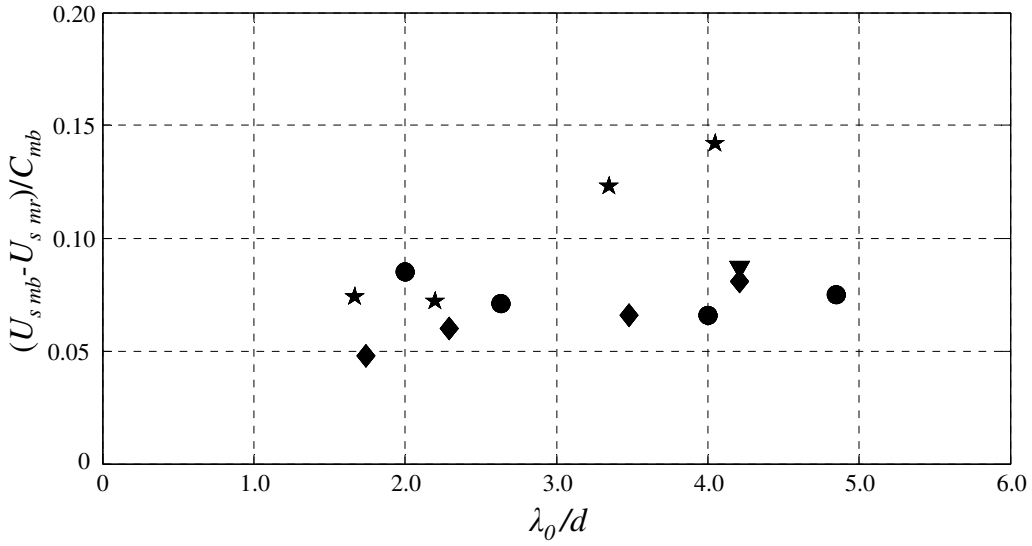

Figure 5.1- The deep water wavelength to water depth ratio versus the crest surface water velocities difference from maximum recurrence to marginal breaking over the marginal breaker crest point speeds for C2N3 (⧫), scaled C2N3 (▼), C2N5 (★) and C3N9 (●) wave packets from deep to shallow water.

The value of energy flux ratio $B_x = U_s/C$ was determined for each case and has been presented in Table 5.1. It was found that the threshold for the breaking onset is robust for different type of wave packets in different water depths. The local crest steepness versus energy flux ratio values at the lower bound and upper bound of the breaking threshold i.e. maximum recurrence and marginal breaking are illustrated in Figure 5.2. The threshold for wave breaking of transitional water waves can be determined as 0.835 ± 0.005 which is in agreement with the deep water two-dimensional wave breaking experiment described in Chapter 4 and is slightly lower than the value proposed numerically by Barthelemy *et al.* (arXiv:1508.06002v1, 2015).

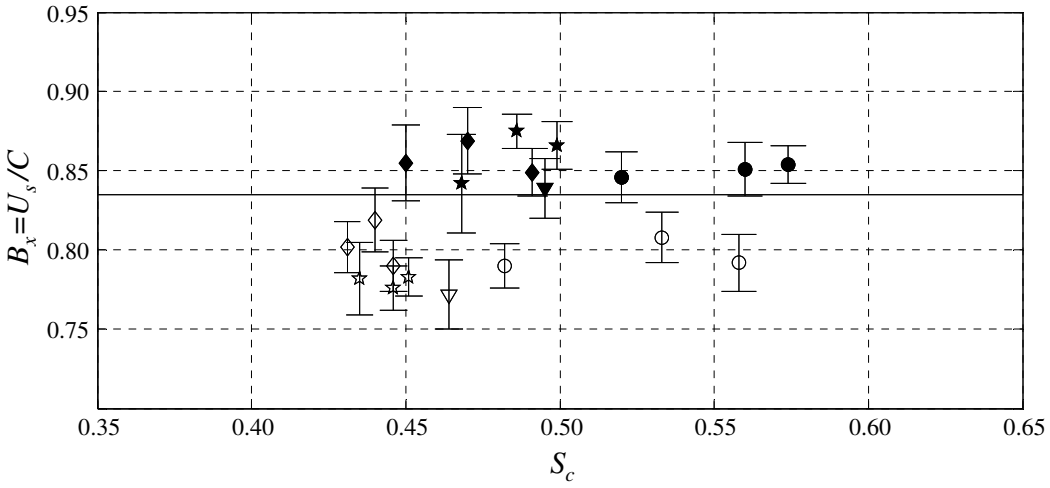

Figure 5.2- Local wave steepness S_c versus crest and surface speeds ratio at the wave crest point $B_x=U_s/C$, showing C2N3 (◇), scaled C2N3 (▽), C2N5 (☆), C3N9 (○), with maximum recurrence waves (hollow shapes) and marginal breaking waves (solid shapes). Error bars indicate the standard deviation of the repeat measurement set (6 to 8 replicates) and the horizontal line at B_x = 0.835 is the breaking threshold.

As shown in Figure 5.2 the threshold of wave breaking is independent of water depth and peak spectral wave numbers. Also, the investigation of the sensitivity of the threshold to the wave scaling revealed that the scaled C2N3 wave as shown in Table 5.1 and Figure 5.2, reduces the threshold by less than 1 %.

A non-dimensional parameter ($\lambda\, \rho^{0.5}\, g^{0.5}\, \sigma^{-0.5}$) was used to evaluate the dependency of the breaking threshold B_x on the wavelength, where λ is the wavelength (m), ρ is the density of water (kg m^{-3}), g is the gravity acceleration (m s^{-2}) and σ is the water surface tension (N m^{-1}). The water density and surface tension were determined using the water temperature measured during each experiment. This dimensionless parameter versus energy flux ratio values for maximum recurrence and marginal breaking waves in transitional water are shown in Figure 5.3. As seen, no dependency of the breaking threshold on the wavelength can be discerned.

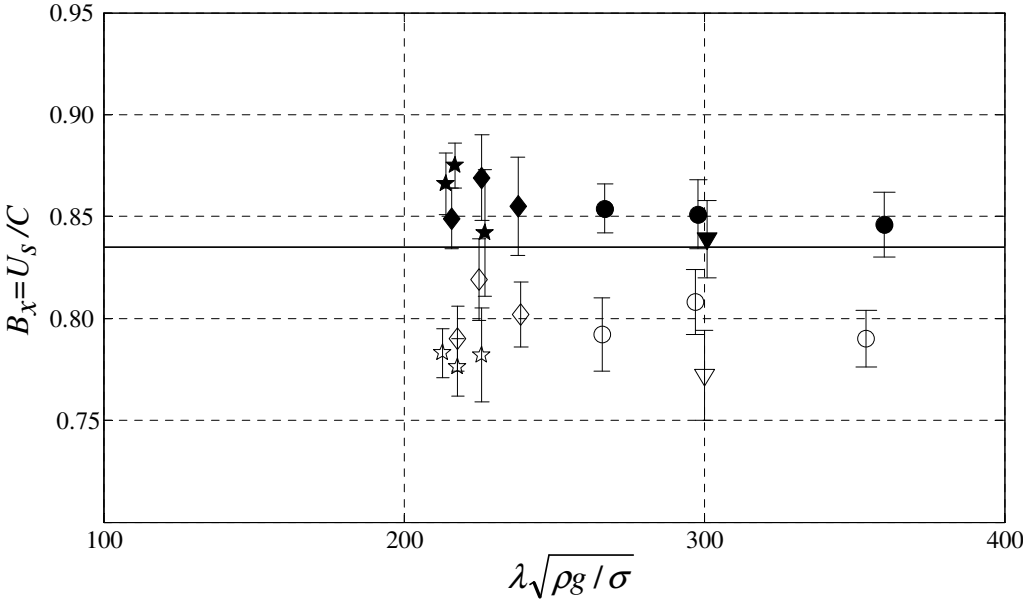

Figure 5.3- Non-dimensional parameter ($\lambda\sqrt{\rho g / \sigma}$) versus crest and surface speeds ratio at the wave crest point $B_x = U_s/C$. The shapes are as defined in Figure 5.2. Error bars indicate the standard deviation of the repeat measurement set (6 to 8 replicates) and the horizontal line at $B_x = 0.835$ is the breaking threshold.

5.3 Depth limited wave heights

This investigation has defined a threshold between non-breaking and breaking waves. Although this does not impose a limit on breaking wave height, the commencement of breaking does indicate the onset of significant wave dissipation.

Nelson (1994) developed empirically a parametric characterisation of the limiting wave heights of monochromatic waves on horizontal beds from deep to shallow water. In his study it was shown that the limiting wave height to water depth does not exceed 0.55. As presented in § 2.3, Nelson (1994) proposed a relationship to predict the limiting wave heights H/d (Equation (2-10)) using a non-dimensional parameter F_c which was adopted from Swart & Loubser (1979) and can be calculated using Equation (2-11). These parameters were determined for different types of wave groups from deep to transitional water and presented in Table 5.1 and Figure 5.4. The wave height

H in the present study was defined as the vertical distance between the crest and the average of the neighbouring troughs. In Figure 5.4, Nelson's characterisation is presented with data assembled from studies relating to breaking onset. The theoretical limit for transitional water depths shown in Figure 5.4 was determined using Equation (2-9) proposed by Miche (1944) and linear wave theory.

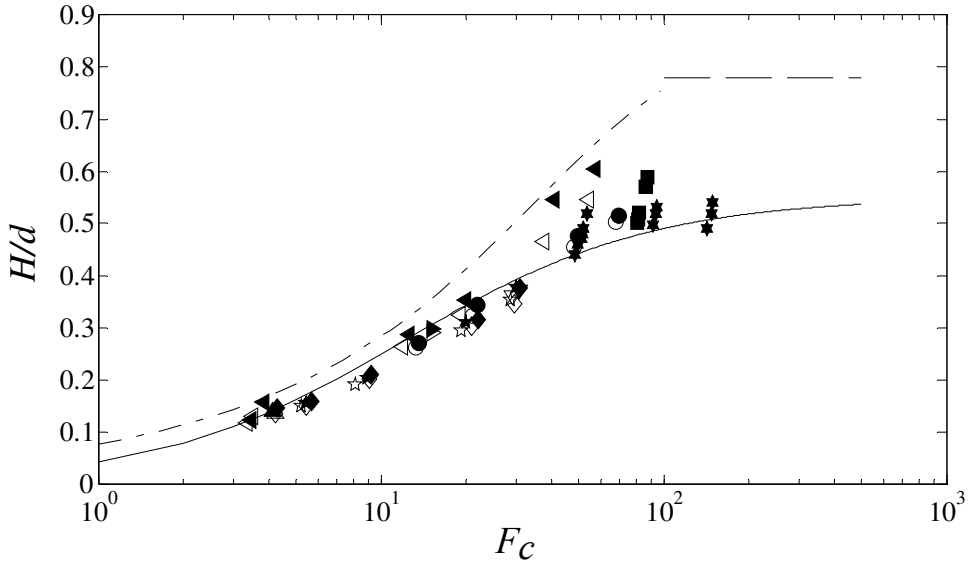

Figure 5.4- F_c versus H/d for waves on horizontal beds from deep to shallow water for C2N3 (◇), scaled C2N3 (▽), 3D C2N3 (△), C2N5 (☆), C3N9 (○), 3D C3N9 (▷) wave groups in the present study, Barthelemy *et al.* (Class 3 waves, 2013) (◁), Riedel & Byrnes (random waves, 1986) (✡), Dack & Peirson (Class 2 waves, 2005) (□) with maximum recurrence waves (hollow shapes) and breaking waves (solid shapes), Nelson's characterisation (monochromatic, 1994) (——), Miche (1944) theoretical limit (— - —) and McCowan (1894) theoretical limit of 0.78 (— — —).

As shown, up to a breaker index of approximately 0.45, the characteristics of the waves at the threshold of this present investigation track Nelson's curve closely. Marginally breaking waves of this present study remain with 10% of values specified by Nelson's curve. Consequently, there should be close correspondence between the surface velocities predicted by Nelson's characterisation and the threshold determined here.

The most developed method of computing crest surface velocities are the steady wave methods described by Fenton (1990). Fenton's spectral approach was applied to the Nelson's curve up to H/d = 0.5 (excluding values in the vicinity of 0.2 where the method did not converge) and yielded a ratio of U_s/C of 0.49 ± 0.04.

While the consistency of this ratio mirrors reasonably the finding of this present study, the mean value of the ratio determined is substantially less. There are two contributing factors. First, as shown by Banner *et al.* (2014) and Barthelemy *et al.* (arXiv:1508.06001v1, 2015, Figure 10), group waves go through a systematic leaning cycle that leads to a slowdown in largest waves within a group. Secondly, as shown by Barthelemy *et al*. (arXiv:1508.06001v1, 2015, Figure 15), the surface velocities of waves transitioning through a group maximum are substantially in excess of those predicted by higher order steady wave theories.

The findings of a sequence of studies over many years now call into question the limit of 0.55 determined empirically by Nelson (1994). The sequence of studies that are summarised in Figure 5.4 show that for shallower water, the effect of wave grouping can generate extreme waves that are at least 30% greater than the values determined by Nelson. The McCowan (1894) and Miche (1944) theoretical limits appear conservative and our present studies would support these as an appropriate basis for design with the curves as shown in Figure 5.4. However, it is important to note that this present study has only investigated marginally breaking waves. More strongly breaking, group waves may exceed the McCowan/Miche limits. This requires further investigation.

5.4 Conclusion

The experiment was conducted for steady transitional to shallow water wave groups in the laboratory. Three water depths were considered for the experiment. The crest surface velocity at the point of crest maximum was

measured for different wave group classes using the Thermal Image Velocimetry technique. Wave crest point speeds at the same instant as the crest point water velocity measurements and the wave characteristics were determined using the two arrays of wave gauges.

It was found that the threshold of breaking which distinguishes upper bound of breaking threshold from lower band of breaking remains robust in transition from deep to shallow water. The threshold for wave breaking of transitional water waves was found to be $B_x = 0.835 \pm 0.005$ which is in agreement with the deep water two-dimensional wave breaking outcomes.

The sensitivity of the threshold in relation to wave scale was investigated. No changes in the threshold for breaking could be discerned.

Finally, the breaker index of marginally breaking waves of the present study was compared with the limiting wave heights determined by Nelson (1985). It was shown that Nelson's characterisation gives a good estimation of the breakerindex to approximately 0.45 (F_c<40) but for higher F_c the effect of wave grouping can generate extreme waves that are significantly greater than the limiting wave heights determined by Nelson (1985) for shallow water.

In conclusion, we found a breaking threshold which is robust for different types of 2D wave groups with no dependence on peak spectral wave numbers and water depth condition.

Chapter 6

DIRECTIONAL DEEP WATER WAVES

In chapter 4 and chapter 5 it was confirmed that the breaking onset threshold B_x is robust for two-dimensional waves in deep and transitional water. In this chapter to investigate the effect of directionality on this onset threshold, different types of three-dimensional wave groups in deep water are examined in the wave basin. The experimental facilities in the wave basin were described in § 3.2.2 and as discussed in § 3.4.2 the TIV technique using the CO_2 laser was applied to measure the water surface and wave crest speeds. The detailed explanations of the methodology can be found in § 3.5.

6.1 Wave conditions

Two wave group structures i.e. Class 2 groups with N = 3 and Class 3 groups with N = 9 were selected for three-dimensional wave experiment in deep water. The water depth in the wave basin was 0.55 m and Class 3 wave parameters were scaled to provide the same depth to wavelength ratio as two-dimensional experiment. Class 2 wave parameters were not scaled as they could satisfy the deep water condition. For C3N9 wave packets, the paddle frequency was scaled to ω_p = 7.517 rad s^{-1} with the non-dimensional chirp rate was C_{t2} = 0.0101. In C2N3 wave groups, ω_{p0} was specified as 9.383 rad s^{-1} with ω_{p1} = 8.043 rad s^{-1}. The dimensionless amplitudes corresponding to the two frequency components were defined as a_0 = 0.473 and a_1 = 0.530.

Two theoretical focal distances x_f = 25 m and x_f = 10 m were considered during these present experiments to match the Allis (2013) experimental setup. One case i.e. C2N3 was selected to be tested for 2D waves and the focal length denoted by x_f = -1 as used by Allis (2013).

Before starting the experiment, the trolley was moved to the far end of the basin and by increasing the paddle amplitude incrementally, the conditions of maximum recurrence and marginal breaking were determined. Then the distance of the paddle to the wave crest points of the first marginal breaker X_{mb0} for each case was measured using the array of wave probes. The paddle amplitudes A_p at ram, the fetch of the crest points of maximum recurrence X_{mr0} and first marginal breaker X_{mb0} for each case are presented in Table 6.1. The distances to initial breaking which were measured in this study matched those of Allis (2013) for 3D C2N3 by better than 0.5 % and for 2D waves better than 3 %. The agreement between these two studies given that entire reconstruction of the experimental facilities is remarkable.

6.2 Threshold of the onset of breaking

It should be noted that, distinguishing the non-breaking from very marginal breaking waves in the wide basin was more difficult than the 2D wave flume. Therefore, the maximum recurrence was defined for the situation where there was no surface rupture anywhere on the water surface. The marginal breaking condition was defined as that at which the largest wave in every group broke at the identified point of initial breaking. Breaking onset for 3D wave packets was at the centre line of the wave basin with (typically) a total breaking width of less than 0.5 m. For 2D waves the breaking onset was across the whole basin width.

The measurements of the local wave crest speeds showed that wave crests slow down as they approach the crest point (maximum elevation) and reaccelerate after the crest maximum. The measured crest point speeds and the horizontal crest point water surface particle velocity for maximum

recurrence and marginal breaking waves are presented in Table 6.1 for each experimental case. Table 6.1 shows averaged values obtained from each data set, with uncertainty expressed as standard error. The experimental results both in 2D flume and in the wave basin show that the crest point and water surface speeds increase in the transition from non-breaking to marginally breaking. For 3D wave groups with two different focal lengths, it can be seen that the horizontal water surface velocities behaviour remains unchanged during this transition while the crest point speeds decrease in most of the cases. This effect of three-dimensionality on deep-water wave groups leads to significant difference between the ratio of the crest point and crest water surface speeds for maximum recurrence and marginal breaking waves.

Table 6.1- Summary of the results: geometric focal length (x_f), focal angle (θ_f), wave paddle amplitude (A_p), fetch of the crest point (X_0), the average and standard deviation of measured crest steepness (S_c), crest point speed (C), crest point water surface particle velocity (U_s), ratio of the velocities at the crest point U_s/C for maximum recurrence and marginal breaking waves.

			Maximum recurrence						Marginal breaking					
Case	X_f (m)	θ_f (°)	A_p (×10^{-2}m)	S_c ±0.005	X_0 (m) —	C (m/s) ±0.014	U_s (m/s) ±0.019	U_s/C ±0.017	A_p (×10^{-2}m)	S_c ±0.018	X_0 (m) —	C (m/s) ±0.013	U_s (m/s) ±0.017	U_s/C ±0.016
C2N3	-1	0	2.375	0.443	8.98	0.894	0.706	0.789	2.489	0.484	9.35	0.949	0.817	0.861
	25	17.6	1.822	0.428	10.86	0.984	0.741	0.753	1.931	0.495	11.02	0.969	0.832	0.859
	10	42.4	1.399	0.445	9.79	0.977	0.773	0.792	1.439	0.508	10.00	1.010	0.877	0.870
C3N9	25	17.6	4.521	0.504	7.98	1.497	1.119	0.747	4.623	0.529	8.14	1.470	1.252	0.852
	10	42.4	3.655	0.536	7.16	1.489	1.141	0.766	3.744	0.557	7.28	1.453	1.242	0.855

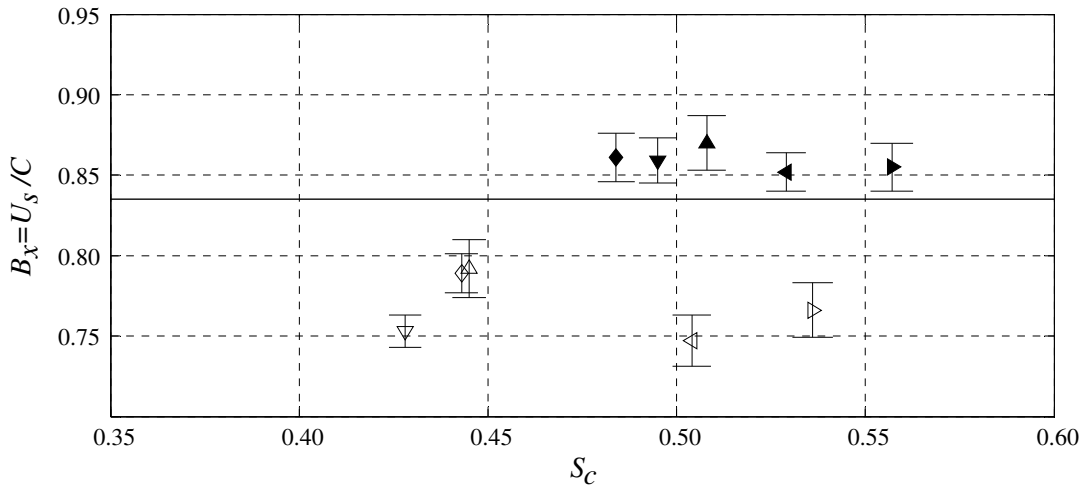

Figure 6.1- Local wave steepness S_c versus crest point to horizontal water surface speeds at the wave crest point ratio $B_x = U_s/C$ for two-dimensional C2N3 (◇) wave groups and three-dimensional wave groups, showing C2N3 $\theta_f = 17.6°$ (▽), C2N3 $\theta_f = 42.4°$ (△), C3N9 $\theta_f = 17.6°$ (◁) and C3N9 $\theta_f = 42.4°$ (▷) with maximum recurrence waves (hollow shapes) and marginal breaking waves (solid shapes). Error bars indicate the standard deviation of the repeat measurement set (6 to 8 replicates) and the horizontal line at $B_x = 0.835$ is the breaking threshold.

The crest point speed to horizontal water particle speed ratios B_x for each case are summarised in Table 6.1. Although, the crest point of directional waves in comparison with uni-directional waves shows a different behaviour, the threshold for the onset of breaking is robust for different type of wave groups and different focal lengths. The local wave steepness versus the crest point speed to the crest water surface speeds ratios at both maximum recurrence and marginal breaking are shown in Figure 6.1. The figure shows that the effect of three-dimensionality on the threshold for the onset of breaking is insignificant. The results of the study for directional waves confirm that the threshold of $B_x = 0.835 \pm 0.005$ can be used to distinguish between breaking and non-breaking waves.

6.3 Conclusion

The convergent tree-dimensional wave groups were generated in a wide wave basin to examine the effect of controlled directional forcing on the threshold for the onset of breaking of deep water waves. TIV technique was used to measure the crest point and horizontal crest water surface speeds for Class 2 and Class 3 wave groups. Two focal lengths (x_f = 10 m and x_f = 25 m) were chosen with the convergence at the centre line of the wave basin. In addition uni-directional C2N3 wave group was selected to be examined in the wave basin using the snack paddle system.

It was found that the crest point speed has different behaviour for 2D and 3D wave groups in the transition from non-breaking to marginal breaking. In 2D waves the crest speeds increase systematically while the crest speeds usually decrease for 3D waves in this transition.

In addition, it was revealed that directionality has insignificant impact on the threshold for the onset of wave breaking.

The threshold was found to be robust for different wave structure and is in a close agreement with two-dimensional wave group measurements and the results of Barthelemy *et al.* (arXiv:1508.06002v1, 2015). Therefore based on the experimental results, the threshold of $B_x = 0.835 \pm 0.005$ can accurately predict the onset of wave breaking for directional waves.

Chapter 7

CONCLUSIONS AND RECOMMENDATIONS

7.1 Overview

Over the past few decades, many criteria have been proposed to determine the onset of wave breaking but there remains a fundamental and long-standing gap as to how to predict the onset of wave breaking. An overview of the proposed criteria of wave breaking onset was presented in chapter 2. Recently, a new breaking onset threshold based on a local threshold of wave energy flux in the crest region of a steep wave has been proposed numerically by Barthelemy *et al*. (arXiv:1508.06002v1, 2015). In this thesis, the proposed threshold for the onset of breaking (B_x) has been explored systematically in the laboratory for different classes of two- and three-dimensional wave groups in deep and transitional water in the absence and presence of wind. The conclusions of the present study and the outlook for future research are presented in this chapter.

7.2 Methodology (chapter 3)

A state-of-the-art thermal Image velocimetry technique using infrared imagery was developed to measure the horizontal water surface velocity (U_s) at the wave crest point. The TIV technique was able to capture crest water velocities before and after a crest maximum event as well as crest surface water velocity for both unforced and wind-forced wave groups. The technique was validated using monochromatic wave trains and the measurements were in a good agreement (within 1 %) with the linear theory.

A linear array of closely-spaced capacitance wave probes was used to measure the wave crest point speed (C). This method was applied for different types of group waves in varied conditions to measure the threshold crest point surface energy flux ratio $B_x = U_s/C$ accurately.

Another linear array of wave gauges was used to measure the wave profiles and crest geometry. These wave probes were utilised for setting up the measurement apparatus at the required locations and also the geometric criteria of breaking for two-dimensional waves were accessed suing the measurements of wave profiles and local crest geometry.

7.3 2D deep water wave groups (chapter 4)

Two-dimensional deep water wave groups were critically examined in the 0.6 m wave flume. Two different wave structures i.e. bimodal (Class 2) and chirped (Class 3) wave groups were used to investigate the robustness of the energy flux ratio B_x with different spectral bandwidths. One of the Class 3 cases was selected to be explored under the different degrees of wind forcing.

It was shown that the threshold for the onset of breaking is $B_x = U_s/C = 0.835 \pm 0.005$ and robust for all cases. The results are approximately 2.0 % lower than the threshold proposed by Barthelemy *et al*. (arXiv:1508.06002v1, 2015).

The sensitivity of the threshold to the degree of wind forcing showed that increasing the wind forcing to $U_{\lambda/4}/C_0 = 1.42$, systematically increased the threshold by 2.0 %. This result is encouraging however further work is required to encompass the full range of open ocean conditions.

The sensitivity of the threshold in relation to group bandwidth showed that increasing the spectral bandwidth (decreasing the Benjamin-Feir index from 0.39 to 0.31), systematically reduced of the threshold by 1.5 %.

The local crest geometric criteria for each wave packet were compared with the breaking threshold of Kjeldsen & Myrhaug (1979) for different types of

breaking and showed that characterising wave steepness in this way does not yield a robust breaking criterion.

7.4 2D transitional water depth wave groups (chapter 5)

The onset of breaking in three different transitional water depths was investigated in 2D. The breaking parameter B_x was measured for three different cases for maximum recurrence and marginal breaking waves. The shallowest Class 2 waves were scaled to examine the potential scaling effects on the threshold.

The threshold was found to be robust for the transition from deep to shallow water for different cases and there was no dependence on peak spectral wave numbers or water depth. This threshold for transitional water depths was in a very good agreement with deep water waves and can be determined as $B_x = 0.835 \pm 0.005$.

Scale effects were investigated using the Class 2 wave with N = 3 showed that changing the linear wavenumber from 7.65 m^{-1} to 5.59 m^{-1} modified the threshold by less than 1 %. An assembly of all data showed no systematic change in the threshold with wave length.

The wave height to water depth ratio (H/d) was studied and compared with Nelson (1985) results. It was found that the effect of wave groups should be considered to find the breaker index as the effect of wave grouping can generate waves in shallower water at least 30 % greater than the limit proposed by Nelson. This present study has only investigated waves at the threshold of breaking. Consequently, a limit at least that of McCowan/ Miche is recommended for coastal engineering design in shallow/ transitional water until it is demonstrated that there is negligible risk of strongly breaking group waves achieving higher breaker indices.

7.5 3D deep water wave groups (chapter 6)

The influence of directionality on the breaking onset threshold was investigated in a wave basin using a snake paddle system for deep water Class 2 and Class 3 wave packets. The theoretical focal lengths for convergent tree-dimensional wave groups were selected at 10 m and 25 m from the paddle at the centre line of the wave basin.

The experimental results of directional waves showed insignificant effect on the threshold for breaking onset and confirmed the robustness of the threshold. The threshold of the onset of breaking for 3D waves was in agreement with the results of 2D waves in the present study and approximately 2.0 % lower than the value of the threshold proposed by Barthelemy *et al.* (arXiv:1508.06002v1, 2015).

Finally, it was found that for directional waves, there was deceleration in crest point speeds in the transition from non-breaking to marginally breaking for most of the cases. This phenomenon is in contrast with two-dimensional waves where the speed of the crest point at marginal breaking waves was always higher than the speeds at the maximum recurrence waves.

7.6 Closing remarks and recommendations

The present investigation has confirmed that a robust threshold exists for determining the onset of breaking for deep and shallow water waves in the presence and absence of wind. The breaking threshold is robust for different types of unidirectional and directional wave groups. The future studies are recommended to answer the following questions to advance the understanding of wave breaking:

- Can this work be extended to determine an appropriate characterisation of subsequent dissipation of wave energy?
- What is the effect of wave grouping on the breaker index in very shallow water depth?

- Can strongly breaking group waves exceed the McCowan/Miche limits?

These studies would be important for coastal engineering and safety community to develop more reliable and cost-effective marine structures design and safety criteria for ship stability.

Finally, the accurate state-of-the-art TIV technique which has been applied to measure horizontal water surface velocities on violently moving water surfaces can naturally be extended to study a range of surface behaviours. Specifically, this technique can be applied to open channel flows for the measurements of current velocities and the measurement of surface rupture.

REFERENCES

ALLIS, M. J. 2013 The speed, breaking onset and energy dissipation of 3D deep-water waves. Ph.D. thesis, UNSW Australia.

BANNER, M. L., BARTHELEMY, X., FEDELE, F., ALLIS, M., BENETAZZO, A., DIAS, F. & PEIRSON, W. L. 2014 Linking reduced breaking crest speeds to unsteady nonlinear water wave group behavior. *Phys. Rev. Lett*. **112**, 114502.

BANNER, M. L., GEMMRICH, J. R., FARMER, D. 2002 Multiscale Measurements of Ocean Wave Breaking Probability. *J. Phys. Oceanogr*. **32**, 3364–75.

BANNER, M. L. & PEIRSON, W. L. 2007 Wave breaking onset and strength for two-dimensional deep-water wave groups. *J. Fluid Mech*. **585**, 93–115.

BANNER, M. L. & PEREGRINE, D. H. 1993 Wave breaking in deep water. *Annu. Rev. Fluid Mech*. **25**, 373–97.

BANNER, M. L. & PHILLIPS O. M. 1974 On the incipient breaking of small scale waves. *J. Fluid Mech.* **65**, 647–56.

BANNER, M. L. & SONG, J. B. 2002 On determining the onset and strength of breaking for deep water waves. Part II: Influence of wind forcing and surface shear. *J. Phys. Oceanogr*. **32**, 2559–70.

BANNER, M. L. & TIAN, X. 1998 On the determination of the onset of breaking for modulating surface gravity water waves. *J. Fluid Mech.* **367,** 107–37.

BARTHELEMY, X., BANNER, M. L., PEIRSON, W. L., DIAS, F. & ALLIS, M. J. 2013 Numerical study of a breaker index in the transition from deep to shallow

water. *Australasian Coasts & Ports Conference: 21nd Australasian Coastal and Ocean Engineering Conference and the 14th Australasian Port and Harbour Conference.* 52–7.

BARTHELEMY, X., BANNER, M. L., PEIRSON, W. L., DIAS, F. & ALLIS, M. J. 2015 On the local properties of highly nonlinear unsteady gravity water waves. Part 1. Slowdown, kinematics and energetics. arXiv:1508.06001v1.

BARTHELEMY, X., BANNER, M. L., PEIRSON, W. L., FEDELE, F., ALLIS, M. & DIAS, F. 2015 On the local properties of highly nonlinear unsteady gravity water waves. Part 2. Dynamics and onset of breaking. arXiv:1508.06002v1.

BENJAMIN, T. B. & FEIR, J. E. 1967 The disintegration of wave trains in deep water. Part 1. Theory. *J. Fluid Mech*. **27**, 417–30.

BOETTCHER, E. J., FINEBERG, J. & LATHROP, D. P. 2000 Turbulence and wave breaking effects on air-water gas exchange, *Phys. Rev. Lett*. **85 (9)**, 2030–33.

BONMARIN, P. 1989 Geometric properties of deep water breaking waves. *J. Fluid Mech.* **209**, 405–33.

CERC (Coastal Engineering Research Centre) 1984 Shore protection manual. US Army Corps of Engineers, Washington, DC.

CHANG, K. A. & LIU, P. L. F. 1998 Velocity, acceleration and vorticity under a breaking wave. *Phys. Fluids.* **10**, 327–29.

DACK, D. A. J. & PEIRSON, W. L. 2005 Depth-limited wave heights associated with wave groups propagating onto horizontal beds. *Proc. Coasts and Ports Australasian Conference.* Adelaide, Australia. 197–202.

DERAKHTI, M. & KIRBY, J. T. 2016 Breaking-onset, energy and momentum flux in unsteady focused wave packets. *J. Fluid Mech.* **790**, 553–81.

DIORIO, J.D., LIU, X., DUNCAN, J. H. 2009 An experimental investigation of incipient spilling breakers. *J. Fluid Mech*. **633**, 271–83.

DOLD, J. W. & PEREGRINE, D. H. 1986 Water-wave modulations. *Proc. 20th Int. Conf. on Coastal Eng.* ASCE. **1**, 163–75.

DUNCAN, J. H. 1981 An Experimental Investigation of Breaking Waves Produced by a Towed Hydrofoil. *Proc. R. Soc. A Math. Phys. Eng. Sci.* **377**, 331–48.

DUNCAN, J. H. 1983 The breaking and non-breaking wave resistance of a two-dimensional hydrofoil. *J. Fluid Mech*. **126**, 507–20.

DUNCAN, J. H. 2001 Spilling breakers. *Annu. Rev. Fluid Mech*. **33**, 519–47.

DUNCAN, J. H., QIAO, H., PHILOMIN, V. & WENZ, A. 1999 Gentle spilling breakers: crest profile evolution. *J. Fluid Mech*. **379**, 191–222.

EASSON, W. J. 1997 Breaking waves. *Offshore Tech. Rep*. OTO-96-035, U.K. Health and Safety Executive, London.

FENTON, J. D. 1990 Nonlinear wave theories. Eds. MÉHAUTÉ, B. L. & HANES, D. M. John Wiley, New York. **9 A**, 3–26.

GALVIN, C. J. 1969 Breaker travel and choice of deign wave height, *J. Waterw. Harbours Div*. **95**, 175–200.

GARBE, C. S., DEGREIF, K. & JÄHNE, B. 2007 Estimating the viscous shear stress at the water surface from active thermography In: GARBE, C. S.,

HANDLER, R. A., JÄHNE, B. (eds.) *Transport at the Air–Sea Interface*, Springer, Heidelberg. 223–39.

GODA, Y. 1970 A synthesis of breaker indices. *Transactions of JSCE*. **2(2)**, 227–30.

GODA, Y. 2010 Reanalysis of regular and random breaking wave statistics. *Coastal Eng*. **52**, 71–106.

GOURLAY, M. R. 1994 Wave transformation on a coral reef. *Coastal Eng*. **23**, 17–42.

GRAY, C. & GREATED, C. A. 1998 The application of particle image velocimetry to the study of water waves *Opt. and Lasers in Eng.* **9**, 265–76.

GRUE, J., CLAMOND, D., HUSEBY, M. & JENSEN, A. 2003 Kinematics of extreme waves in deep water. *Appl. Ocean Res.* **25**, 355–66.

HOLTHUIJSEN, L. H. 2007 Waves in oceanic and coastal waters. CUP. ISBN 978-0-521-86028-4.

HSU, C. T. & HSU, Y. 1983 On the structure of the turbulent flow over a progressive water wave: theory and experiment in a transformed, wave-following coordinate system. Part 2. *J. Fluid Mech.* **131**, 123–153.

IVERSEN, H. W. 1952 Waves and breakers in shoaling water. *Proc. 5th Int. Conf. on Coastal Eng.* ASCE, 1–12.

JANSSEN, P. A. E. M. 2003 Nonlinear four-wave interaction and freak waves. *J. Phys. Oceanogr.* **33 (4)**, 863–84.

JENSEN, A., SVEEN, J. K., GRUE, J., RICHON, J. B. & GRAY. C. 2001 Accelerations in water waves by extended particle image velocimetry. *Exp. Fluids*. 30, 500–10.

JESSUP, A. T. & PHADNIS, K. R. 2005 Measurement of the geometric and kinematic properties of microscale breaking waves from infrared imagery using a PIV algorithm. *Meas. Sci. Techno*. **16**, 1961–69.

KINSMAN, B. 1965 Wind Waves: Their Generation and Propagation on the Ocean Surfaces. *Dover Phoenix Editions, Dover Publications*.

KJELDSEN, S. P. & MYRHAUG, D. 1979 Breaking waves in deep water and resulting wave forces. *Proc. Annu. Offshore Technol. Conf.* 2515–22. New York: Am. Inst. Min. Metall. Petrol. Eng.

KWAY, J. H. L., LOH, Y. S. & CHAN, E. S. 1998 Laboratory study of deep water breaking waves. *Ocean Eng*. 25, 657–76.

LONGUET-HIGGINS, M. S. 1963 The generation of capillary waves by steep gravity waves. *J. Fluid Mech*. **16**, 138–59.

LONGUET-HIGGINS, M. S. 1974 Breaking waves in deep or shallow water. *In Proc. 10th Conf. on Naval Hydrodynamics.* M.I.T., 597–605.

MASSEL, S. R. 1996 On the largest wave height in water of constant depth. *Ocean Eng.* **23(7)**, 553–73.

MASTENBROEK, C. 1996 Wind Wave Interaction. Ph.D. thesis, Delft Technical University.

MCCOWAN, J. 1894 On the highest wave of permanent type. *Philosophical Magazine*. **5 (38)**, 351–57.

MELVILLE, W. K. 1994 Energy dissipation by breaking waves. *J. Phys. Oceanogr*. **24**, 2041–49.

MELVILLE, W. K. 1996 The role of surface-wave breaking in air-sea interaction. *Annu. Rev. Fluid Mech*. **28**, 279–321.

MELVILLE, W. K. & MATUSOV, P. 2002 Distribution of breaking waves at the ocean surface. *Lett. Nature*. **417**, 58–63.

MELVILLE, W. K. & RAPP, R. J. 1988 The surface velocity field in steep and breaking waves. *J. Fluid Mech*. **189**, 1–22.

MICHE, M. 1944 Le pouvoir reflechissant des ouvrages maritimes exposes a l'action de la houle. *Ann. Ponts Chaussees.* **121,** 285–318.

MUSTE, M., SCHONE, J. & CREUTIN., J. D. 2005 Measurement of free-surface flow velocity using controlled surface waves. *Flow Measurement and Instrumentation.* **16**, 47–55.

NELSON, R. C. 1985 Wave heights in depth limited conditions. *Civil Eng. Trans. Inst. Eng. Aust.* **27,** 210–15.

NELSON, R. C. 1994 Depth limited design wave heights in very flat regions. *Coastal Eng.* **23**, 43–59.

NEPF, H. M., WU C. H. & CHAN, E. S. 1998 A comparison of two- and three-dimensional wave breaking. *J. Phys. Oceanogr*. **28**, 1496–510.

OH, S. H., MIZUTANI, N., SUH, K. D. & HASHIMOTO, N. 2005 Experimental investigation of breaking criteria of deepwater wind waves under strong wind action. *Appl. Ocean Res*. **27**, 235–50.

PEIRSON, W. L. 1997 Measurement of surface velocities and shears at a wavy air-water interface using particle image velocimetry. *Exp. Fluids.* **23**, 427–37.

PEIRSON, W. L. & BANNER, M. L. 2003 Aqueous surface layer flows induced by microscale breaking wind waves*. J. Fluid Mech*. **479**, 1–38.

PEIRSON, W. L., WALKER, J. W. & BANNER, M. L. 2014 On the microphysical behaviour of wind-forced water surfaces and consequent re-aeration. *J. Fluid Mech*. **743**, 399–447.

PERLIN, M., CHOI, W. & TIAN, Z. 2013 Breaking waves in deep and intermediate waters *Annu. Rev. Fluid Mech.* **45**, 115–45.

PERLIN, M., HE, J. & BERNAL, L. P. 1996 An experimental study of deep water plunging breakers. *Phys. Fluids*. **8**, 2365–74.

PERLIN, M. & SCHULTZ, W. W. 2000 Capillary effects on surface waves. *Annu. Rev. Fluid Mech*. **32**, 241–74.

PHILLIPS, O. M. 1977 The dynamics of the upper ocean. CUP ISBN 0 521 29801 6.

PHILLIPS, O. M. & BANNER, M. L. 1974 Wave breaking in the presence of wind drift and swell*. J. Fluid Mech*. **66,** 625–40.

QIAO, H & DUNCAN, J. H. 2001 Gentle spilling breakers: crest flow-field evolution. *J. Fluid Mech*. **439**, 57–85.

RAMBERG, S. E. & GRIFFIN, O. M. 1987 Laboratory study of steep and breaking deep water waves. *J. Water. Port Coastal Ocean Eng.* **113**, 493–507.

RANKINE, W. J. M. 1862 On the exact form and motion of waves at and near the surface of deep water. *Proc. R. Soc. London.* 275–77.

RAPP, R. J. & MELVILLE, W. K. 1990 Laboratory measurements of deep water breaking waves. *Phil. Trans. Roy. Soc. Lond.* **A 331**, 735–800.

RIEDEL, H. P. & BYRNE, A. P. 1986 Random breaking waves - horizontal seabed. *Proc. 12th ICCE*, ASCE. 903–8.

SAKET, A., PEIRSON, W. L., BANNER, M. L., BARTHELEMY, X. & ALLIS, M. J. 2017 On the threshold for wave breaking of two-dimensional deep water wave groups in the absence and presence of wind. *J. Fluid Mech.* **811**, 642–658.

SCHULTZ, W. W., HUH, J. & GRIFFIN, O. M. 1994 Potential energy in steep and breaking waves. *J. Fluid Mech*. **278**, 201–28.

SEIFFERT, B. R. & DUCROZET, G. 2016 Deep water wave-breaking in a high-order spectral model. *31th Int. Workshop on Water Waves and Floating Bodies*, Plymouth, MI, USA.

SHE, K., GREATED, C. A. & EASSON, W. J. 1994 Experimental study of three-dimensional wave breaking. *J. Waterw. Port Coast. Ocean Eng*. **120**, 20–36.

SHEMER, L. & LIBERZON, D. 2014 Lagrangian kinematics of steep waves up to the inception of a spilling breaker. *Phys. Fluids*. **26**, 016601.

SIDDIQUI, M. H. K., LOEWEN, M. R., RICHARDSON, C., ASHER, W. E. & JESSUP, A. T. 2001 Simultaneous particle image velocimetry and infrared imagery of microscale breaking waves. *Phys. Fluids.* **13**, 1891–903.

SONG, J. B. & BANNER, M. L. 2002 On determining the onset and strength of breaking for deep water waves. Part I: Unforced irrotational wave groups. *J. Phys. Oceanogr*. **32**, 2541–58.

STANSBERG, C. T. 1997 On the nonlinear behaviour of ocean wave groups. Ocean Wave Measurement and Analysis. *Proc. Third Int. Symposium WAVES 97*. Virginia, ASCE.

STANSELL, P. & MACFARLANE, C. 2002 Experimental investigation of wave breaking criteria based on wave phase speeds. *J. Phys. Oceanogr.* **32**, 1269–83.

STOKES, G. G. 1880 Appendices and supplement to a paper on the theory of oscillatory waves. *Math. Phys. Pap.* **1**, 219–29.

SVENDSEN, I. A. & VEERAMONY, J. 2001 Wave breaking in wave groups. *J. Water. Port Coastal Ocean Eng*. July/August, 200–12.

SWART, D. H. & LOUBSER, C. C. 1979 Vocoidal wave theory. Vol. 2: verification. *Research Report 360, NRIO, CSIR*.

TERRILL, E. J., MELVILLE, W. K. & STRAMSKI, D. 2001 Bubble entrainment by breaking waves and their influence on optical scattering in the upper ocean. J. *Geophys. Res*., **106 (C8)**, 16815–23.

THORPE, S. A. 1995 Dynamical process of transfer at the sea surface, *Prog. Oceanogr*., **35**, 315–52.

TIAN, Z., PERLIN, M. & CHOI, W. 2008 Evaluation of a deep-water wave breaking criterion. *Phys. Fluids.* **20**, 066604.

TIAN, Z., PERLIN, M. & CHOI, W. 2010 Energy dissipation in two-dimensional unsteady plunging breakers and an eddy viscosity model. *J. Fluid Mech*. **655,** 217–57.

TKALICH, P. & CHAN, E. S. 2002 Vertical mixing of oil droplets by breaking waves. *Mar. Pollut. Bull*. **44 (11)**, 1219–29.

TULIN, M. P. & WASEDA, T. 1999 Laboratory observations of wave group evolution, including breaking effects. *J. Fluid Mech*. **378**, 197–232.

VERON, F. & MELVILLE, W. K. 2001 Experiments on the stability and transition of wind driven water surfaces. *J. Fluid Mech.* **446**, 25–65.

VERON, F., MELVILLE, W. K. & LENAIN, L. 2008 Infrared techniques for measuring ocean surface processes. *J. Atmos. Oceanic Technol*. **25 (2)**, 307–26.

WEGGEL, J. R. 1972 Maximum Breaker Height. *J. Waterw., Harbours and Coastal Eng. Div.* **98**, 529–48.

WU, C. H. & NEPF, H. M. 2002 Breaking criteria and energy losses for three dimensional wave breaking. *J. Geophys. Res.* **107**, 3177.

Yamada, H., Kimura, G. & Okabe, J. 1968 Precise determination of the solitary waves of extreme height on water of a uniform depth. *Rep. Res. Inst. Applied Mech.* Kyushu Univ. **XVI (52)**, 15–32.

APPENDIX A

Copies of the publications during the course of this study

J. Fluid Mech. (2017), *vol.* 811, *pp.* 642–658.
doi:10.1017/jfm.2016.776

On the threshold for wave breaking of two-dimensional deep water wave groups in the absence and presence of wind

Arvin Saket[1,†], William L. Peirson[1], Michael L. Banner[2], Xavier Barthelemy[1,2] and Michael J. Allis[1,3]

[1]Water Research Laboratory, School of Civil and Environmental Engineering, UNSW Australia, 110 King St., Manly Vale, NSW 2093, Australia

[2]School of Mathematics and Statistics, UNSW Australia, Sydney 2052, Australia

[3]National Institute of Water and Atmospheric Research, Hamilton 3251, New Zealand

(Received 25 July 2015; revised 3 November 2016; accepted 14 November 2016)

The threshold for the onset of breaking proposed by Barthelemy *et al.* (arXiv:1508.06002v1, 2015) has been investigated in the laboratory for unidirectional wave groups in deep water and extended to include different classes of wave groups and moderate wind forcing. Thermal image velocimetry was used to compare measurements of the wave crest point (maximum elevation and also the point of maximum) surface water particle velocity (U_s) with the wave crest point speed (C) determined by an array of closely spaced wave gauges. The crest point surface energy flux ratio $B_x = U_s/C$ that distinguishes maximum recurrence from marginal breaking was found to be 0.840 ± 0.016. Increasing wind forcing from zero to $U_{\lambda/4}/C_0 = 1.42$ systematically increased this threshold by 2 %. Increasing the spectral bandwidth (decreasing the Benjamin–Feir index from 0.39 to 0.31) systematically reduced the threshold by 1.5 %.

Key words: surface gravity waves, waves/free-surface flows, wave breaking

1. Introduction

Water wave breaking is a dominant dynamical process of the upper ocean, inducing strong flow–turbulence–wave interactions and air–sea exchanges (Banner & Peregrine 1993; Melville 1996; Perlin & Schultz 2000; Perlin, Choi & Tian 2013; Peirson, Walker & Banner 2014). Phillips (1977, § 3.9) provides a very insightful characterisation of wave breaking and its historical developments at that time. The above references highlight the heightened interest in wave breaking and its consequences in the ensuing decades. However, as Holthuijsen (2007, p. 188) points out, 'A complicating factor is that there is no generally accepted, precise definition of breaking'. Despite the high visibility of whitecaps at sea and wave breaking at coastlines and beaches, there remains a fundamental and long-standing gap as to how to characterise and predict the onset of wave breaking.

Historically, Stokes (1880) developed his theoretical approach culminating in his steady irrotational wave of maximum steepness, beyond which breaking was assumed

† Email address for correspondence: a.saket@wrl.unsw.edu.au

to occur. During subsequent decades, a number of other strategies have been proposed for determining a robust threshold for breaking of freely propagating water waves, involving geometric, kinematic and dynamic criteria. For example, Banner & Phillips (1974) refined Stokes' approach to account for the effects of wind drift, investigating its impact via the kinematic criterion in which breaking onset is linked directly to fluid at the crest point exceeding the speed of the crest. Other criteria based on a limiting fluid particle acceleration for stability of the crest point have also been proposed and investigated (e.g. Longuet-Higgins 1963, appendix).

Perlin *et al.* (2013) also describe a more recent genre of breaking onset criteria based on energy flux rates at steep crests, which appear to provide a more robust basis for quantifying breaking onset (Song & Banner 2002; Banner & Peirson 2007; Tian, Perlin & Choi 2008). A significant refinement of this approach was published very recently by Derakhti & Kirby (2016). In this context, our perspective is that the critical transition in energy convergence rate from maximum recurrence to the weakest spilling breaking defines a breaking threshold. Above this threshold, the wave will break. Apart from this latest work, the interested reader is referred to Perlin *et al.* (2013) for a comprehensive overview of the status of the various proposed breaking onset criteria.

In the present paper, we examine critically the threshold proposed by Barthelemy *et al.* (2015). Through an ensemble of boundary element numerical simulations of fully nonlinear two- and three-dimensional wave packets in deep and finite depth water, these authors proposed a breaking onset threshold based on a local threshold of wave energy flux in the crest region of a steep wave. They found that predicting the subsequent local onset of breaking can be described with reference to energy flux considerations. For nonlinear wave groups, the local energy flux vector $\boldsymbol{F} = \boldsymbol{U}(P + \rho g z + 0.5\rho U^2)$, where $\boldsymbol{U}$ is velocity and $U = |\boldsymbol{U}|$, P is pressure, ρ is the fluid density and z is the elevation, when normalised by the local energy density $E = \rho g z + 0.5\rho U^2$, can be considered as a local energy flux velocity. At the wave surface and under the *specific conditions* of zero surface pressure, this local energy flux velocity reduces to the water surface particle velocity, which maximises at the wave crest point. At the wave crest point (used interchangeably with the 'crest maximum elevation' throughout this paper), the water surface particle velocity is denoted by U_s. Based on the local energy flux velocity $(\boldsymbol{F}/E)$ and the local (horizontal) crest point speed (C), Barthelemy *et al.* (2015) define a new breaking onset variable $\boldsymbol{B} = (\boldsymbol{F}/E)/C$, which is the ratio of the local energy flux velocity and the local crest point speed. In the wave propagation direction (taken as the x direction), this reduces to $B_x = (U_s/C)$. They found that the onset of breaking occurs once the water surface particle speed at the wave crest point exceeds a critical proportion of the speed of the slowing crest point as it passes through the maximum of a wave group. The critical threshold was observed to be robust, for both long-crested and short-crested waves.

Using thermal image velocimetry (TIV) techniques to measure water surface particle speeds (Veron & Melville 2001; Veron, Melville & Lenain 2008) at the crests of waves transitioning through a group maximum (the spatial and temporal instant at which group energy density is at a maximum), we critically examine the robustness of this breaking threshold for grouped waves in the laboratory with different group classes, spectral bandwidths and degrees of wind forcing.

To avoid the uncertainty associated with capturing wave breaking onset events with their attendant very short time scales (Duncan *et al.* 1999), this present study identified the threshold for wave breaking as follows. Using the approach of Rapp &

Melville (1990) and Banner & Peirson (2007), the rate of energy convergence at the point of initial wave breaking was systematically increased. Repeat observations of the wave groups transitioning through the point of initial breaking revealed that two conditions could be clearly defined.

Up to a certain wave paddle forcing level, dominant waves of successive groups were observed to progress through the group envelope maximum with no observable residual disturbance of the water surface. This condition was termed the maximum recurrent or maximum non-breaking threshold, and indicated a lower bound to the breaking threshold. Further slight but sufficient augmentation of paddle forcing level triggered a significant change in dominant wave behaviour at the initial break point. For each successive group, a disturbance in the wave surface was observed to occur at the same fetch, characterised by a visible bulge just ahead of the wave crest (Duncan *et al.* 1999), accompanied by surface irregularity and trailing patches of capillary ripples. This condition was termed the marginal breaking condition and used to identify the upper bound of the breaking threshold. Based on this definition of the breaking threshold, this present contribution critically examines the proposal of Barthelemy *et al.* (2015).

As discussed above, for zero wind forcing, the energy flux criterion on the wave surface simplifies to the ratio of fluid speed to crest point speed, which gives it the character of a kinematic breaking criterion, which has been investigated by previous investigators. Although, Melville & Rapp (1988) did not measure crest point speeds, they did highlight the significant changes in crest surface current structure associated with initiation of breaking. Perlin, He & Bernal (1996) capture velocity fields within the crest of a single wave transitioning from a pre-breaking to plunging state. Qiao & Duncan (2001) show that, at the transition to spilling breaking, the maximum water velocity in the crest of the wave shifts to the forward face of the wave. They also show a systematic increase in the maximum water velocity in the crest as a proportion of the crest point speed when expressed as a function of crest propagation distance. Oh *et al.* (2005) found that breaking of strongly forced wind waves is observed when the crest point surface velocities are substantially less than the crest point speed. However, their observations do not distinguish whether individual waves were actually breaking. Consequently, their data do not permit a robust assessment of whether there is a systematic difference between crest water speed to crest speed ratios of non-breaking waves in comparison with those of breaking waves.

Of specific relevance to the present investigation is the incisive work of Stansell & MacFarlane (2002), who investigated the kinematic breaking criterion experimentally. From their measurements, they concluded that wave breaking was initiated at a ratio of crest water speed to crest point speed significantly less than unity, which is the value implied by the kinematic breaking criterion. Their findings are compared with present measurements later in this paper.

2. Experimental facilities and methods

2.1. *Laboratory facilities*

The experiments were conducted in the two-dimensional wind–wave tank located at UNSW Australia, Water Research Laboratory, Manly Vale. The flume was 30 m long, 0.6 m wide and 0.6 m deep with glass sidewalls and a solid floor. Waves were generated using a computer-controlled, flexible cantilevered wave paddle located at one end of the flume. A flexible reticulated polyester–urethane foam absorbent beach was installed at the other end of the tank to minimise reflections of the generated

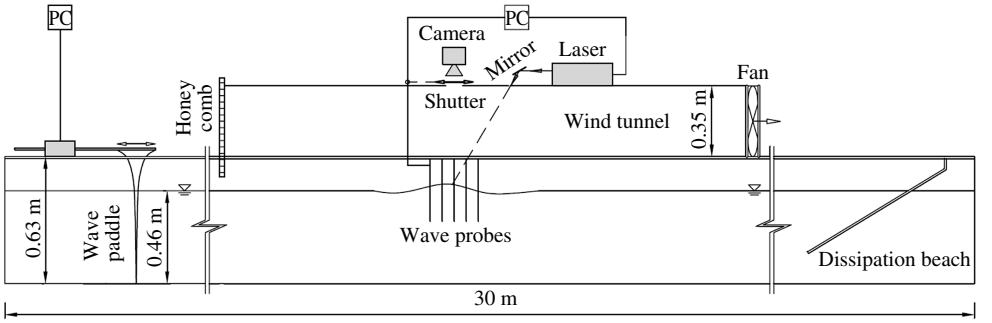

FIGURE 1. Sketch of the experimental set-up (not to scale) used in the present study. The details of the dimensions and distances are given in the text.

waves (figure 1). The water depth during these present experiments was 0.46 m and the waves propagating along the tank were two-dimensional.

The tank configuration was identical to that used by Banner & Peirson (2007), except that a movable wind tunnel of length of 7.5 m was mounted on the tank, with the roof of the tunnel 0.5 m above the still water surface. At the upwind end of the tunnel, an adjustable honeycomb flow guide of 50 mm thickness and composed of 8 mm diameter tubes was installed to establish a uniform air flow within the wind tunnel when air was drawn through the tunnel by a fan at its downstream end. Wind intensity was controlled by varying the fan input voltage using a metered Variac. The wind speed was measured on the centreline of the tunnel approximately 4.8 m downwind of the inlet and 0.25 m above the still water level (SWL) using a pre-calibrated hot probe air velocity meter (Velocicalc model 8347).

A thermal camera (Flir T420) was mounted looking down at the centre of the wind tunnel roof to observe the tank water surface through a shuttered window 3.6 m downwind of its inlet. The movable wind tunnel could be positioned so that the camera observed the water surface at the location of the group maximum (the locations at which a repetitive wave group has its extreme amplitude). TIV was used to measure the horizontal water particle velocities at the crests of waves transitioning through the group maximum. The entire TIV system consisted of an irradiating source, a computer-controlled shutter, the thermal imaging camera and a computer controlling the system components.

Surface irradiation was provided by a pulsed CO_2 laser (Firestar T100) mounted at the centre of the wind tunnel roof and aligned using an adjustable infrared range flat mirror. Pulses triggered by the controlling computer were timed to create a sequence of circular heat patches of approximately 4 mm diameter at locations just upstream of the group maximum location.

Surface reflections could potentially damage the thermal imaging camera used to acquire images of the moving heat patches. Consequently, the computer-controlled shutter remained closed during surface irradiation.

After irradiation, the shutter was opened and the thermal imaging camera was able to observe the water surface vertically from above, capturing 320 pixel $\times$ 240 pixel images of the surface at 30 frames per second. The physical resolution of the thermal imager was approximately 0.66 mm per pixel at the water surface, determined using calibration grids placed within the field of view.

Wave paddle amplitudes corresponding to maximum group recurrence and marginal group breaking were determined by illuminating the tunnel and observing waves

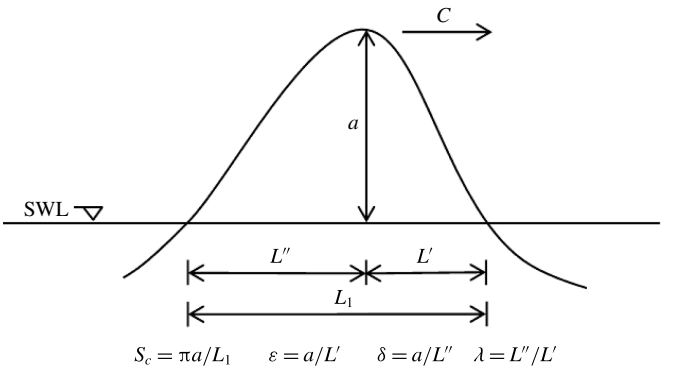

FIGURE 2. Definitions of the local crest geometry: S_c is the local steepness, ε and δ are the crest-front and crest-rear steepness, respectively, and λ is the vertical asymmetry parameter (Kjeldsen & Myrhaug 1979).

through the glass walls. Wave motion was monitored by two linear arrays of capacitance wave probes mounted 50 mm in from each of the tank sidewalls. To minimise any effect of the probes on the wind flow, the wave probe signal conditioning boxes were mounted outside of the tunnel with 6 mm diameter cables connecting the boxes to the 3 mm diameter, 250 mm long probe frames.

The central probe of each set of wave probes was positioned at the same fetch as the centre of the thermal imaging area. The fetch is the horizontal distance from the wave generator to the observation point. Each probe was fitted with a 200 mm long, 0.2 mm diameter wire element. The wave data were captured using a National Instruments PCI-6225 data acquisition at 1000 Hz sample rate per channel. The probe resolution was 0.1 mm with the linearity of ± 0.2 mm over their length.

To measure the local crest point speeds, five wave probes were installed along one tank wall with a spacing of 6 mm. Using the time series recorded by wave probes, the time of the dominant crest arrival at each wave probe was determined and thereby the crest point speed at the central probe was calculated.

To measure the geometry of the crests, seven wave probes were located at the other side of the tank with the spacing of 100 mm. The water level time series captured by the wave probes were interpolated in space to obtain the zero-crossing locations at the time of the wave group maximum and, thereby, crest geometry (figure 2). The geometric characterisations of Kjeldsen & Myrhaug (1979), i.e. local steepness S_c, crest-front steepness ε, crest-rear steepness δ and vertical asymmetry λ, were determined at the instant of the wave group maximum using the equations presented in figure 2.

Fast Fourier transforms were used to obtain the single-sided wave frequency spectra, the peak frequency (f_0), the frequencies associated with the half-peak energy (f_{min} and f_{max}) and frequency bandwidth ($\Delta f = (f_{max} - f_{min})/2$). The Benjamin–Feir index ($BFI = (k_0^2\langle\eta^2\rangle)^{1/2}\sqrt{2}/(\Delta f/f_0)$) was used for comparison with other studies (e.g. Janssen 2003) where k_0 is the characteristic wavenumber associated with the peak frequency and $\langle\eta^2\rangle$ is the variance of the average surface elevation. Linear wave theory was used to calculate the corresponding wavenumber k_0 and linear phase speed C_0 for each wave group.

2.2. *Initial wave group conditions*

Concomitant crest point water particle velocities and the crest point speeds were measured for both monochromatic and group waves. To validate the TIV technique, the monochromatic waves were generated using

$$x_p(t) = A_p \sin(\omega_p t), \tag{2.1}$$

where x_p is the wave paddle motion, A_p is proportional to the piston amplitude, ω_p is the paddle angular frequency and t is time.

The wave packets generated by the paddle were selected to correspond to the cases used by Banner & Peirson (2007). Both a bimodal spectrum with developing sideband instabilities (called here class 2; Benjamin & Feir 1967) and chirped wave packets (class 3; Longuet-Higgins 1974) were considered in the present study.

The bimodal initial spectrum was defined by two superimposed frequency components as follows:

$$x_p(t) = A_p \left(a_0 \cos(\omega_{p0} t) + a_1 \cos\left(\omega_{p1} t - \frac{\pi}{18} \right) \right), \tag{2.2}$$

where $a_0 = 0.473$ and $a_1 = 0.530$ are dimensionless amplitudes corresponding to the two frequency components. For the two class 2 cases, ω_{p0} was specified as 9.383 rad s^{-1} with ω_{p1} taking values of 8.043 rad s^{-1} and 8.530 rad s^{-1} for $N = 3$ (C2N3) and $N = 5$ (C2N5) waves, respectively.

The chirped (class 3) wave packets were generated using

$$x_p = -0.25 A_p \left(1 + \tanh \frac{4\omega_p t}{N\pi} \right) \left(1 - \tanh \frac{4(\omega_p t - 2N\pi)}{N\pi} \right) \sin(\omega_p (t - \omega_p C_{t2} t^2/2)), \tag{2.3}$$

where C_{t2} is the chirp rate of the linear modulation. The paddle frequency ω_p of 8.18 rad s^{-1} and the non-dimensional chirp rate of $C_{t2} = 0.0101$ were used for three class 3 wave packets with $N = 5$, 7 and 9 (denoted hereafter as C3N5, C3N7 and C3N9).

2.3. *Method*

Prior to each experiment, the tank water surface was cleaned by generating waves for approximately 1 h at the beginning of each day. Any surface slick material was transported to the dissipating beach at the far end from the wave generator. Once the water surface had been cleaned, the wave probes were immersed into the tank for approximately 1 h to ensure that their signals were stable. The tank surface was inspected regularly to ensure that it was not contaminated with any slick material. Tank water temperatures were recorded before and after each experiment.

The threshold amplitudes for breaking for the five different wave packets described above were determined in the absence of wind. In addition, the thresholds for the C3N7 wave packet were determined with wind forcing applied.

The wind conditions were selected as a perturbation on the no-wind condition. To minimise possible wind-induced growth or attenuation effects, the wind speeds were selected to match the wave speeds as closely as possible (Mastenbroek 1996, figure 4.5).

In each case, paddle amplitudes were incrementally increased to determine the conditions of maximum recurrence (that is, the maximum paddle amplitude at which

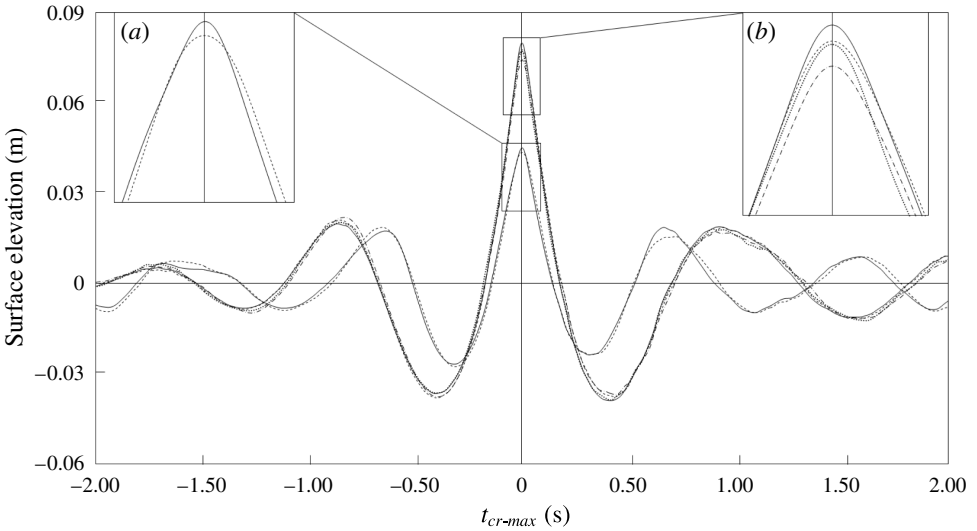

FIGURE 3. Surface elevation time series at the location of group maximum for unforced non-breaking (- - -) and marginal breaking (——) C2N3 and C3N7 waves and wind-forced non-breaking (— · —) and marginal breaking (· · · · · ·) C3N7U2.0 waves. C2N3 are of smaller amplitudes and the crest detail is shown by the left inset; C3N7 crest detail is shown in the right inset. Time (t) is referenced to the instant of the crest maximum elevation. Note the implied steeper forward face of the marginally breaking wave in comparison with its corresponding maximally recurrent wave and the differences of the mean steepness at breaking onset between the two classes of waves.

no surface rupture was observed anywhere on the water surface) and marginal breaking (the minimum paddle amplitude at which consistent breaking was observed at the point of maximum wave group amplitude) in each case. The paddle amplitudes (A_p) for the different group classes and wind forcing conditions are presented in table 1. The fetches of the group maximum were carefully recorded. Group maximum fetches (and therefore the fetch of marginal breaking) increased systematically with the number of waves in each group. Once the group maximum fetch had been determined, the entire wind tunnel assembly was located over this point and measurement of the local wave characteristics and surface current proceeded. The time series of surface elevation at the location of the group maximum for maximum recurrence and marginal breaking C2N3 and C3N7 wave packets in the absence of wind as well as wind-forced C3N7 wave packets are shown in figure 3. Figure 3 shows the differences of the mean steepness at breaking onset between the two classes of waves. As can be seen, only small differences can be observed in the time water level records obtained at the location of the crest maximum elevation. As shown in the insets, the implied forward face steepnesses of the marginally breaking waves are significantly higher than their corresponding maximally recurrent waves.

The measured geometric parameters for the different group classes and wind forcing conditions are summarised in table 1. Table 1 shows the averaged values obtained from each dataset, with uncertainty expressed as standard error. The degree of the asymmetry of the crest for each wave packet in the present study has been compared with the breaking threshold of Kjeldsen & Myrhaug (1979) for different types of breaking waves in table 1. As shown in table 1, characterising wave steepness in this way does not yield a robust breaking criterion.

Class	$U_{\lambda/4}$ (m s^{-1})	Maximum recurrence					Marginal breaking				
		$A_{p(SWL)}$ ($\times 10^{-2}$ m)	S_c ± 0.016	ε ± 0.010	δ ± 0.010	λ ± 0.012	$A_{p(SWL)}$ ($\times 10^{-2}$ m)	S_c ± 0.014	ε ± 0.011	δ ± 0.010	λ ± 0.031
C2N3	—	1.032	0.402	0.261	0.252	1.037	1.067	0.422	0.287	0.252	1.136
C2N5	—	0.846	0.431	0.271	0.288	0.977	0.863	0.451	0.303	0.273	1.110
C3N5	—	1.763	0.481	0.341	0.278	1.228	1.784	0.492	0.353	0.281	1.253
C3N7	—	1.744	0.469	0.324	0.277	1.171	1.773	0.480	0.327	0.287	1.142
C3N9	—	1.733	0.478	0.328	0.284	1.154	1.756	0.486	0.333	0.288	1.158
C3N7	1.4	1.680	0.460	0.286	0.299	0.957	1.740	0.476	0.304	0.301	1.011
C3N7	2.0	1.611	0.449	0.282	0.288	0.977	1.663	0.467	0.300	0.295	1.018
Kjeldsen & Myrhaug (1979)	—	—	—	<0.320	<0.260	<0.900	—	—	>0.320	>0.260	>0.900

TABLE 1. Wind speed at the elevation of one quarter of the dominant wavelength above SWL ($U_{\lambda/4}$), wave paddle amplitude at SWL ($A_{p(SWL)}$), the average and standard deviation of measured crest steepness (S_c), crest-front steepness (ε), crest-rear steepness (δ) and horizontal asymmetry parameter (λ) for maximum recurrence and marginal breaking wave groups. The last row indicates the Kjeldsen & Myrhaug (1979) breaking threshold for each geometric parameter.

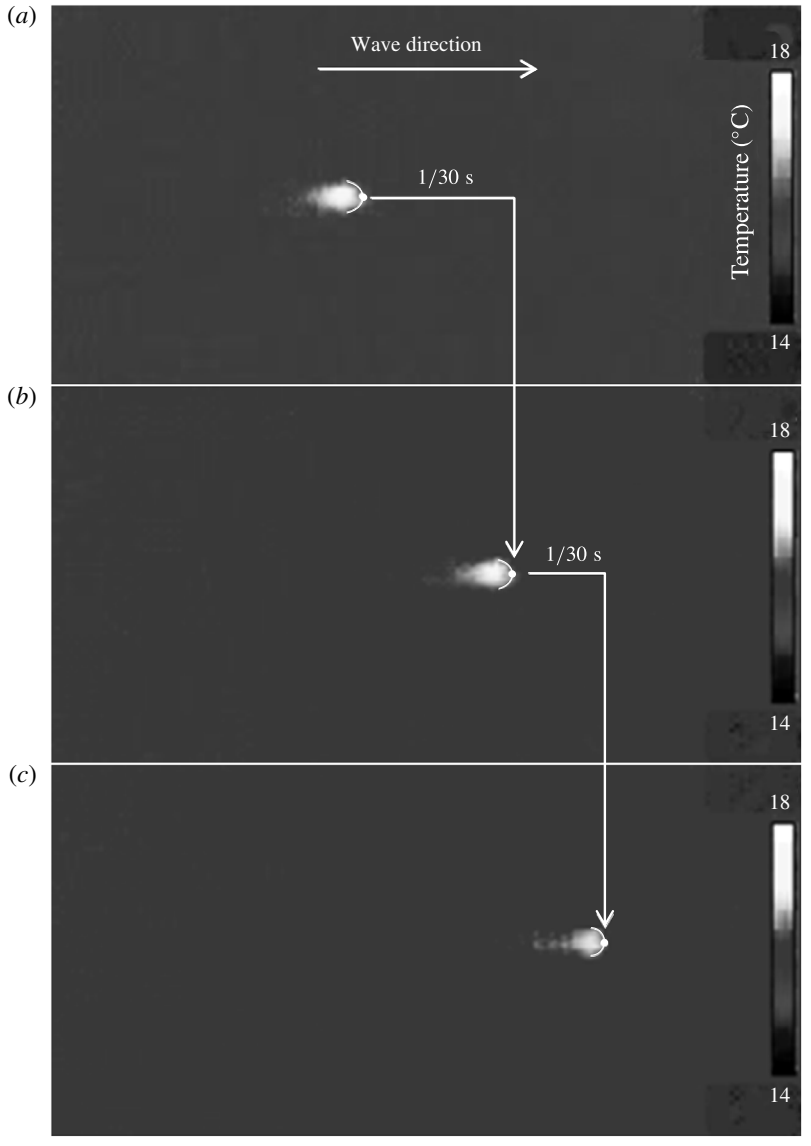

FIGURE 4. Tracking the hot spot on the wave crest at the location of crest maximum elevation for three successive frames. The camera is stationary.

The most challenging measurements were determining the crest surface velocities at the crest points. This required ensuring that the position of heat patches coincided with the crest maximum concomitant with group maximum occurrence. Consequently, the sequence of heat patches had to be initially positioned on the surface, allowing for their subsequent wave orbital transport to the immediately vicinity of group maximum. Trial and error was used to achieve this.

Also, the temperature of the heat patches decreased with time. This required careful minimisation of the measurement duty cycle and careful selection of those thermal image sequences in which the thermal patches remained clearly defined (figure 4).

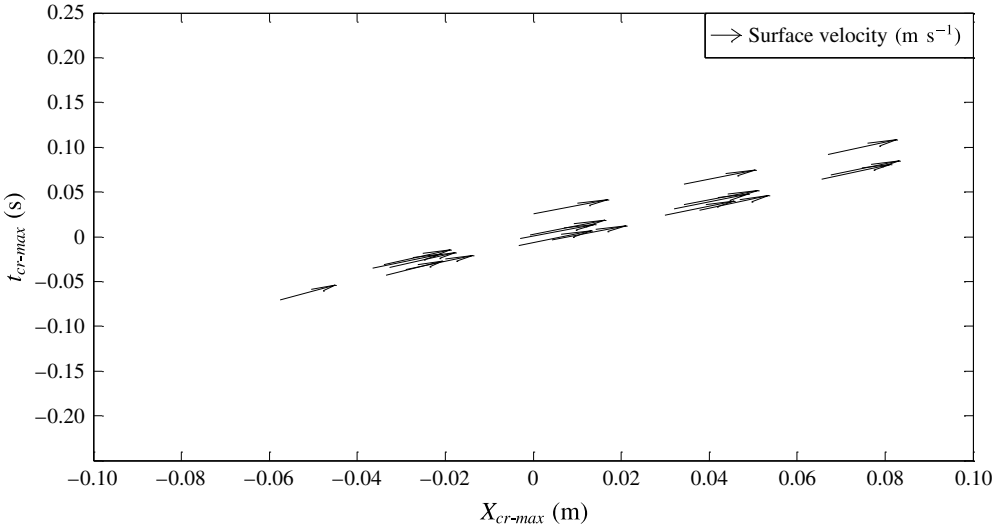

FIGURE 5. Surface water velocity (m s^{-1}) for marginal breaking C3N7 wave group. The arrows represent the surface water velocity; $X_{cr\text{-}max}$ is the position of each point referenced to the location of crest maximum elevation of the transiting group.

By differentiating the heat patch positions with time, a sequence of surface water velocities in the vicinity of the group maximum could be determined. An exemplary sequence for C3N7 in the absence of wind is shown in figure 5. In figure 5, X is the position of each point referenced to the location of crest maximum elevation (the centre of the image) and t is time, referenced to the crest maximum elevation event.

In figure 5, the arrows show an ensemble of surface velocity measurements obtained from thermal image records obtained in the vicinity of a sequence of crest maximum elevation events for five wave groups.

To obtain a measurement of velocity localised at the time and location of a crest maximum elevation event, the synchronised thermal imagery and wave probe records were processed as follows. First, thermal patch velocities in immediate spatial proximity of the crest maximum elevation were determined at the time of the crest maximum elevation event. It was found that the duty cycle of the coupled laser–shutter–camera–wave probe system could be synchronised to achieve five velocity measurements surrounding the crest maximum elevation location at the time of the crest maximum elevation.

These five velocities were plotted as a function of distance referenced to the crest maximum elevation position as shown in figure 6. The results indicated that the maximum surface velocity coincided with the location of crest maxima in each case. A polynomial curve was fitted as shown in figure 6 to determine the maximum water velocity U_s.

Owing to the framing rate, the absolute time reference of the thermal imagery can only be synchronised with the wave probes with an accuracy of ± 17 ms. This uncertainty in synchronisation determines an uncertainty in the wave crest point velocity determined by this process. This uncertainty was evaluated using polynomial fits to the data obtained in the vicinity of crest maximum elevation events and is indicated in figure 6.

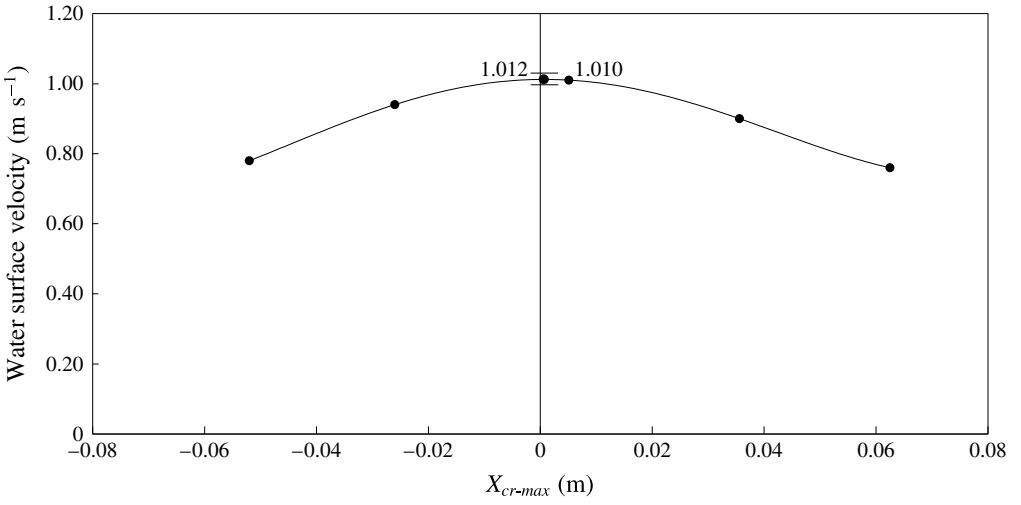

FIGURE 6. Polynomial curve fitted to water surface velocities and the interpolated velocity at the crest maximum elevation for a marginal breaking C3N7 wave group. The error bars indicate the uncertainty arising from synchronisation of the TIV measurements with the wave probes. Note that the maximum velocity occurs at the wave crest point.

The influence of wind on the onset of wave breaking was investigated for the C3N7 case and followed an identical method. The maximum wind speed investigated was 2.0 m s^{-1}. Above this speed, the thermal patches created by the laser could no longer be clearly identified and tracked within five thermal image frames captured through a group maximum occurrence event. Measurements were also undertaken at a wind speed of 1.4 m s^{-1} to verify that any observed trends were consistent. In the absence of forced waves, the TIV technique was used to measure the water surface velocities at a fetch of 3.6 m. These water surface velocities were found to be 0.065 m s^{-1} and 0.078 m s^{-1} at the wind speeds of 1.4 m s^{-1} and 2.0 m s^{-1}, respectively.

Validation was undertaken by applying the TIV technique to monochromatic waves of modest steepness and frequency 10.472 rad s^{-1}. The water depth and the paddle amplitude for the validation case were $d = 0.23$ m and $A_p = 0.0052$ m. Measured wave characteristics were compared with linear wave theory predictions of the surface water velocity (u_{sL}) at the wave crest and crest speed (C_L) obtained based on the wave frequency. The comparison is presented in table 2. As shown, the measurements and linear theory agree within 1 %.

3. Results and discussion

The measurements of group waves showed that the wave crest points systematically slow down as they approach their crest maximum and subsequently reaccelerate thereafter, as described by Banner *et al.* (2014).

The measured crest point speeds and crest surface water velocities at the instant of the wave group maximum are summarised in table 3 for each experimental case. Sample values at both maximum recurrence and marginal breaking define the bounds on the onset threshold and are shown in figure 7. Table 3 shows averaged values obtained from each dataset, with uncertainty expressed as standard error.

The results show a robust global threshold for the onset of wave breaking of $B_x = U_s/C = 0.840 \pm 0.016$. None of the recurrent groups reach the threshold, while all

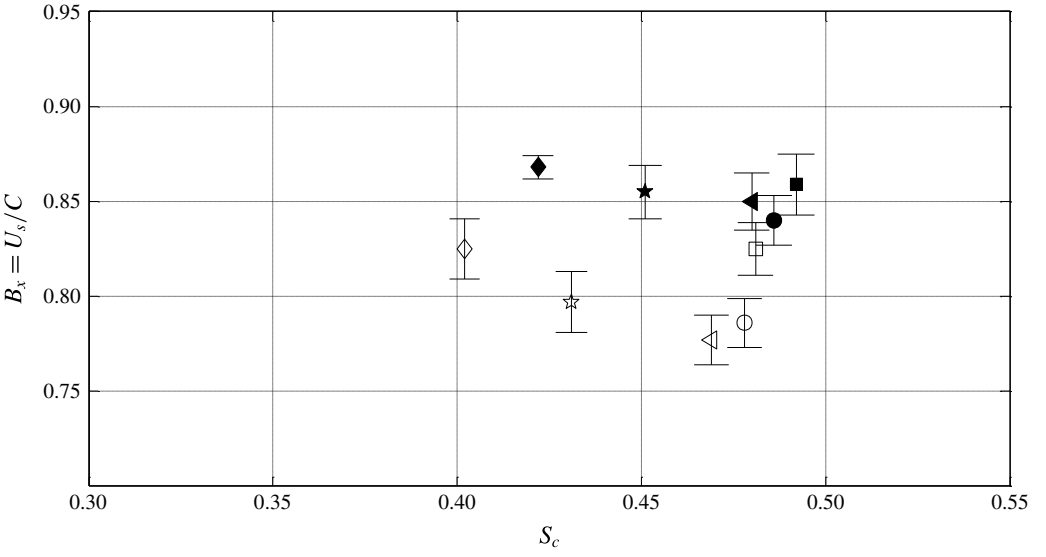

FIGURE 7. Local wave steepness S_c versus crest and surface speeds ratio at the wave crest point $B_x = U_s/C$ for unforced waves, showing C2N3 (◇), C2N5 (☆), C3N5 (□), C3N7 (◁) and C3N9 (○), with maximum recurrence waves (hollow symbols) and marginal breaking waves (solid symbols). Error bars indicate the standard deviation of the repeat measurement set (6–8 replicates).

	ak	C (m s^{-1})	C_L (m s^{-1})	u_{sL} (m s^{-1})	U_s (m s^{-1})
Average	0.1337	0.9235	0.9265	0.1430	0.1440
Standard deviation	0.0034	0.0104	—	0.0041	0.0033

TABLE 2. Measurements verifying the TIV technique. Using a monochromatic paddle frequency $\omega_p = 10.472$ rad s^{-1} and locally measuring a, the local wave steepness (ak), linear wave crest speed (C_L) and water surface velocity (u_{sL}) were estimated using linear wave theory. These are compared with the water surface velocity (U_s) measured using the TIV technique and crest speed (C) obtained from the wave probe records. Note that the differences between theory and measurement are less than 1 %.

marginal breaking cases exceed the threshold. This threshold is robust for different types of wave groups and shows no dependence on peak spectral wavenumbers. As shown in figure 7, the characteristic local steepness levels at the threshold of breaking between the class 2 and class 3 groups are distinct.

In each case, it is the crest surface water velocity that plays the dominant role in determining the overall value of this parameter. For all wave groups, across the threshold the crest point speed remained almost unchanged between the recurrent to marginal breaking wave condition. In contrast, the surface water velocity increased significantly across the threshold.

Stansell & MacFarlane (2002) gathered similar data but without a direct method of measuring the surface velocity. They used particle image velocimetry to capture the near-surface velocity profiles beneath waves approaching breaking onset. Smooth

Class	$U_{\lambda/4}$ (m s^{-1})	$U_{\lambda/4}/C_0$	Maximum recurrence							Marginal breaking						
			C (m s^{-1}) ±0.014	U_s (m s^{-1}) ±0.017	U_s/C ±0.014	f_0 (Hz) ±0.001	Δf (Hz) ±0.004	$\Delta f/f_0$ ±0.003	*BFI* ±0.004	C (m s^{-1}) ±0.014	U_s (m s^{-1}) ±0.019	U_s/C ±0.016	f_0 (Hz) ±0.002	Δf (Hz) ±0.004	$\Delta f/f_0$ ±0.003	*BFI* ±0.004
C2N3	—	—	0.959	0.791	0.825	1.375	0.482	0.351	0.379	0.964	0.837	0.868	1.382	0.518	0.375	0.388
C2N5	—	—	0.944	0.753	0.797	1.431	0.545	0.381	0.320	0.963	0.824	0.855	1.445	0.580	0.402	0.347
C3N5	—	—	1.098	0.906	0.825	1.164	0.425	0.365	0.358	1.145	0.983	0.859	1.179	0.436	0.370	0.362
C3N7	—	—	1.187	0.922	0.777	1.106	0.412	0.373	0.347	1.224	1.040	0.850	1.108	0.433	0.390	0.350
C3N9	—	—	1.191	0.936	0.786	1.041	0.414	0.398	0.298	1.240	1.041	0.840	1.047	0.441	0.421	0.302
C3N7	1.4	0.99	1.237	0.959	0.775	—	—	—	—	1.239	1.056	0.852	—	—	—	—
C3N7	2.0	1.42	1.255	1.011	0.806	—	—	—	—	1.254	1.085	0.865	—	—	—	—

TABLE 3. Wind forcing ($U_{\lambda/4}/C_0$) and the average and standard deviation of measured crest point speed (C), crest point water surface particle velocity (U_s), energy flux ratio at the crest point U_s/C, peak frequency (f_0), frequency bandwidth (Δf) and Benjamin–Feir index (*BFI*) for maximum recurrence and marginal breaking waves.

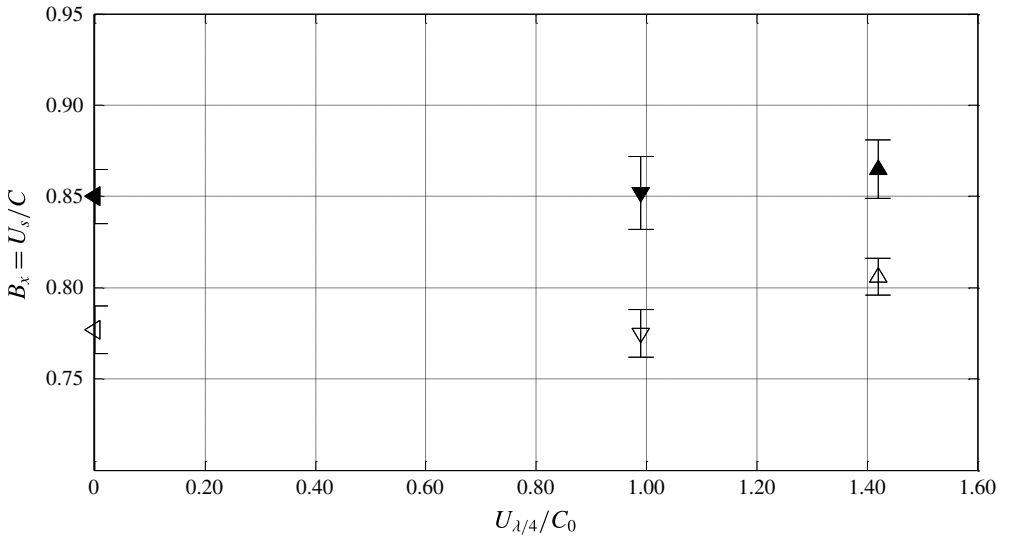

FIGURE 8. Wind forcing $U_{\lambda/4}/C_0$ versus crest and surface speeds ratio at the crest point $B_x = U_s/C$ for wind-forced waves, showing C3N7 (◁), C3N7U1.4 (▽) and C3N7U2.0 (△), with maximum recurrence waves (hollow symbols) and marginal breaking waves (solid symbols). Error bars indicate the standard deviation of the repeat measurement set (6–8 replicates).

extrapolations of 10 points of data gathered at 5 mm grid points below the surface were used to estimate the surface velocity.

The findings of their study support this present investigation except in one aspect. Stansell & MacFarlane (2002) found that for a single case of a wave (their wave 1) captured just before the onset of plunging breaking, the ratio of crest point water speed to crest point speed was 0.81. This is 5 % less than the breaking onset threshold found during this present study.

Figure 3 in Stansell & MacFarlane (2002) illustrates their surface velocity extrapolation technique using another experimental case (wave 3). If the two velocity measurements most proximate to the surface of wave 3 are linearly extrapolated to the surface, the estimated surface velocity would be 1.66 m s^{-1}, as opposed to the value of 1.51 m s^{-1} determined by their extrapolation technique. Consequently, an extrapolation technique using the data in closest proximity to the surface may yield values more than 10 % higher than they report. If a similar correction is applicable to their more extreme plunging case (case 1, referred to above), their data would be entirely consistent with the finding of this present investigation.

Returning to these present results, their sensitivity has also been investigated in relation to two factors: wind forcing and group bandwidth.

As shown in table 3, the degree of wind forcing has been characterised in terms of the wind speed at an elevation of one quarter of the dominant wavelength ($U_{\lambda/4}$) above the mean water surface. For wind forcing $U_{\lambda/4}/C_0$ less than 1.42, the determined breaking threshold remains robust as shown in figure 8.

However, more careful examination of the C3N7 data presented in figure 8 and table 3 shows that, as $U_{\lambda/4}/C_0$ increases from zero to 1.42, there is a slight systematic increase in the threshold in U_s/C of approximately 2.0 %. Consequently, wind has a slightly stabilising effect on the underlying wave field.

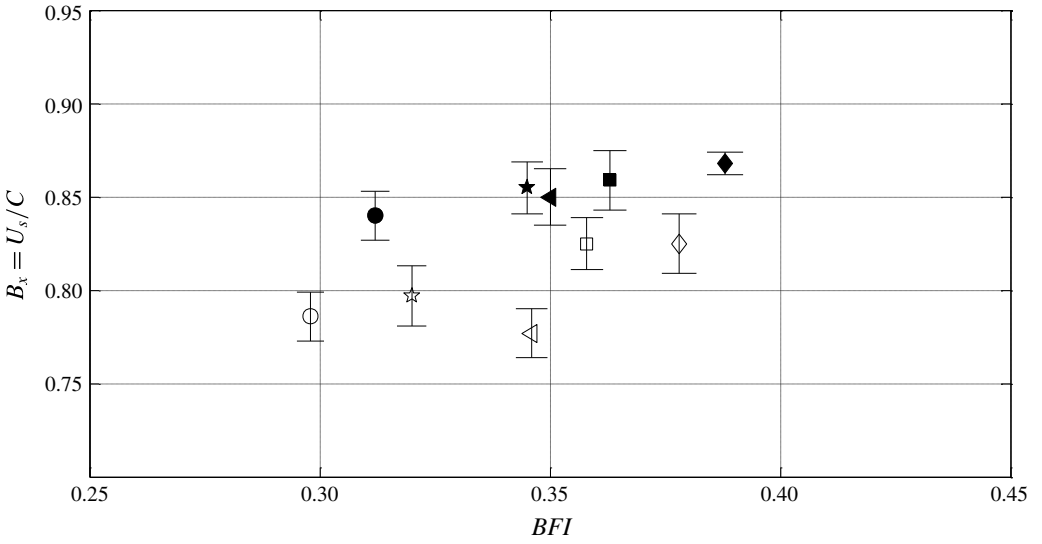

FIGURE 9. Benjamin–Feir index BFI versus crest and surface speeds ratio at the wave crest point $B_x = U_s/C$ for unforced waves. The shapes are as defined in figure 7. Error bars indicate the standard deviation of the repeat measurement set (6–8 replicates).

The local energy density has no contribution from any change in the surface pressure. In view of this systematic response to wind, it is useful to review the relative contributions of the three energy flux components: pressure, elevation and water speed.

As shown in Mastenbroek (1996, figure 4.7), a wave of crest steepness $S_c = 0.48$ with $U_\lambda/C = 2$ has an estimated wind-induced crest surface pressure perturbation less than $15ak\rho_a u_*^2$, where ak is the mean wave steepness, ρ_a is the density of air and u_* is the friction velocity in the air. No measurements of friction velocity were taken during this present investigation, but by referring to the similar conditions investigated by Hsu & Hsu (1983), friction velocities will remain less than 0.08 m s^{-1}. Consequently, the pressure perturbation due to the imposition of wind is estimated as less than 0.05 Pa. This is less than 0.03 % of the other contributions to the energy flux.

As shown in table 3, the imposition of wind perturbs the elevation contribution to the flux by approximately 6 % and the water speed component by over 10 %. The dominant perturbation to the flux ratio arises from changes in the crest water speed due to the wind. Perturbations by the wind-induced pressure itself are negligible.

Group bandwidth has been proposed as an important factor in determining the occurrence of extreme waves, and so we have assessed its influence on the threshold. We note that spectral bandwidth can change appreciably with fetch and therefore is not a robust means of characterising group wave fields. In the context of these experiments, spectral bandwidth changed by less than ± 5 % within a distance of $\pm 3\lambda_0$ around the group maximum location.

As discussed earlier, the fetch to initial breaking increases as the bandwidth increases. Consequently, there is also a correlation between bandwidth and the envelope growth rate immediately prior to breaking inception (Banner & Peirson 2007, figure 5).

The most systematic relationship between breaking onset threshold and spectral bandwidth that emerged from the measurements is shown in figure 9. As shown, the

threshold systematically increases with the *BFI*. Over the range of group bandwidths considered here, the change in the threshold is only a few per cent.

4. Conclusions and recommendations

Thermal image velocimetry has been used to measure the crest surface water velocity at the crest maximum elevation of freely propagating, unsteady deep water wave groups in the laboratory. Wave crest point speeds were determined using an array of closely spaced wave gauges at the same instant as the crest point water velocity measurements.

Barthelemy *et al.* (2015) proposed an energy flux ratio $B_x = U_s/C$ to define a threshold that distinguishes maximum recurrence from marginal breaking. The threshold value B_x was determined to be 0.840 ± 0.016 during this present experimental study. This present study encompassed different classes of wave groups exhibiting distinct characteristic steepnesses in the vicinity of the breaking threshold.

Increasing wind forcing from zero to $U_{\lambda/4}/C_0 = 1.42$ increased the threshold systematically by 2.0 %.

Increasing the spectral bandwidth (decreasing the Benjamin–Feir index from 0.39 to 0.31) systematically reduced of the threshold by 1.5 %.

These encouraging results motivate extension of this present work to shallow waters, three-dimensional breaking and field conditions.

Acknowledgements

Funding for this investigation was provided by the Australian Research Council under Discovery Project DP120101701. The expert technical assistance provided by Mr L. Paice and Mr R. Jenkins are gratefully acknowledged.

REFERENCES

BANNER, M. L., BARTHELEMY, X., FEDELE, F., ALLIS, M., BENETAZZO, A., DIAS, F. & PEIRSON, W. L. 2014 Linking reduced breaking crest speeds to unsteady nonlinear water wave group behavior. *Phys. Rev. Lett.* **112**, 114502.

BANNER, M. L. & PEIRSON, W. L. 2007 Wave breaking onset and strength for two-dimensional deep-water wave groups. *J. Fluid Mech.* **585**, 93–115.

BANNER, M. L. & PEREGRINE, D. H. 1993 Wave breaking in deep water. *Annu. Rev. Fluid Mech.* **25**, 373–397.

BANNER, M. L. & PHILLIPS, O. M. 1974 On the incipient breaking of small scale waves. *J. Fluid Mech.* **65**, 647–656.

BARTHELEMY, X., BANNER, M. L., PEIRSON, W. L., FEDELE, F., ALLIS, M. & DIAS, F. 2015 On the local properties of highly nonlinear unsteady gravity water waves. Part 2. Dynamics and onset of breaking. arXiv:1508.06002v1.

BENJAMIN, T. B. & FEIR, J. E. 1967 The disintegration of wave trains in deep water. Part 1. Theory. *J. Fluid Mech.* **27**, 417–430.

DERAKHTI, M. & KIRBY, J. T. 2016 Breaking-onset, energy and momentum flux in unsteady focused wave packets. *J. Fluid Mech.* **790**, 553–581.

DUNCAN, J. H., QIAO, H., PHILOMIN, V. & WENZ, A. 1999 Gentle spilling breakers: crest profile evolution. *J. Fluid Mech.* **379**, 191–222.

HOLTHUIJSEN, L. H. 2007 Waves in oceanic and coastal waters. CUP. ISBN 978-0-521-86028-4.

HSU, C. T. & HSU, Y. 1983 On the structure of the turbulent flow over a progressive water wave: theory and experiment in a transformed, wave-following coordinate system. Part 2. *J. Fluid Mech.* **131**, 123–153.

JANSSEN, P. A. E. M. 2003 Nonlinear four-wave interaction and freak waves. *J. Phys. Oceanogr.* **33** (4), 863–884.

KJELDSEN, S. P. & MYRHAUG, D. 1979 Breaking waves in deep water and resulting wave forces. In *Proc. Annu. Offshore Technol. Conf.*, pp. 2515–2522. Am. Inst. Min. Metall. Petrol. Eng.

LONGUET-HIGGINS, M. S. 1963 The generation of capillary waves by steep gravity waves. *J. Fluid Mech.* **16**, 138–159.

LONGUET-HIGGINS, M. S. 1974 Breaking waves in deep or shallow water. In *Proc. 10th Conf. on Naval Hydrodynamics*, pp. 597–605. MIT.

MASTENBROEK, C. 1996 Wind wave interaction. PhD thesis, Delft Technical University.

MELVILLE, W. K. 1996 The role of surface-wave breaking in air-sea interaction. *Annu. Rev. Fluid Mech.* **28**, 279–321.

MELVILLE, W. K. & RAPP, R. J. 1988 The surface velocity field in steep and breaking waves. *J. Fluid Mech.* **189**, 1–22.

OH, S. H., MIZUTANI, N., SUH, K. D. & HASHIMOTO, N. 2005 Experimental investigation of breaking criteria of deepwater wind waves under strong wind action. *Appl. Ocean Res.* **27**, 235–250.

PEIRSON, W. L., WALKER, J. W. & BANNER, M. L. 2014 On the microphysical behaviour of wind-forced water surfaces and consequent re-aeration. *J. Fluid Mech.* **743**, 399–447.

PERLIN, M., CHOI, W. & TIAN, Z. 2013 Breaking waves in deep and intermediate waters. *Annu. Rev. Fluid Mech.* **45**, 115–145.

PERLIN, M., HE, J. & BERNAL, L. P. 1996 An experimental study of deep water plunging breakers. *Phys. Fluids* **8**, 2365–2374.

PERLIN, M. & SCHULTZ, W. W. 2000 Capillary effects on surface waves. *Annu. Rev. Fluid Mech.* **32**, 241–274.

PHILLIPS, O. M. 1977 *The Dynamics of the Upper Ocean*. Cambridge University Press.

QIAO, H. & DUNCAN, J. H. 2001 Gentle spilling breakers: crest flow-field evolution. *J. Fluid Mech.* **439**, 57–85.

RAPP, R. J. & MELVILLE, W. K. 1990 Laboratory measurements of deep water breaking waves. *Phil. Trans. R. Soc. Lond.* A **331**, 735–800.

SONG, J. B. & BANNER, M. L. 2002 On determining the onset and strength of breaking for deep water waves. Part I. Unforced irrotational wave groups. *J. Phys. Oceanogr.* **32**, 2541–2558.

STANSELL, P. & MACFARLANE, C. 2002 Experimental investigation of wave breaking criteria based on wave phase speeds. *J. Phys. Oceanogr.* **32**, 1269–1283.

STOKES, G. G. 1880 Appendices and supplement to a paper on the theory of oscillatory waves. *Math. Phys. Pap.* **1**, 219–229.

TIAN, Z., PERLIN, M. & CHOI, W. 2008 Evaluation of a deep-water wave breaking criterion. *Phys. Fluids* **20**, 066604.

VERON, F. & MELVILLE, W. K. 2001 Experiments on the stability and transition of wind driven water surfaces. *J. Fluid Mech.* **446**, 25–65.

VERON, F., MELVILLE, W. K. & LENAIN, L. 2008 Infrared techniques for measuring ocean surface processes. *J. Atmos. Ocean. Technol.* **25** (2), 307–326.

Development of thermal image velocimetry techniques to measure the water surface velocity

A Saket[1], W L Peirson[1], M L Banner[2] and X Barthelemy[1,2]
[1] Water Research Laboratory, School of Civil and Environmental Engineering, UNSW Australia, 110 King Street, Manly Vale, NSW 2093, Australia
[2] School of Mathematics and Statistics, UNSW Australia, Sydney, NSW 2052, Australia

Email: a.saket@wrl.unsw.edu.au, w.peirson@unsw.edu.au, m.banner@unsw.edu.au, and x.barthelemy@wrl.unsw.edu.au

Abstract. Particle image velocimetry (PIV) is a state-of-the-art non-intrusive technique for velocity and fluid flow measurements. Due to ongoing improvements in image hardware and processing techniques, the diversity of applications of the PIV method continues to increase. This study presents an accurate thermal image velocimetry (TIV) technique using a CO_2 laser source to measure the surface wave particle velocity using infrared imagery. Experiments were carried out in a 2-D wind wave flume with glass side walls for deep-water monochromatic and group waves. It was shown that the TIV technique is robust for both unforced and wind-forced group wave studies. Surface wave particles attain their highest velocity at the group crest maximum and slow down thereafter. As previously observed, each wave crest slows down as it approaches its crest maximum but this study demonstrates that the minimum crest speed coincides with maximum water velocity at the wave crest. Present results indicate that breaking is initiated once the water surface particle velocity at the wave crest exceeds a set proportion of the velocity of the slowing crest as it passes through the maximum of a wave group.

1. Introduction

Visualisation techniques play a central role in fluid mechanics in quantifying the behaviour of a flow field. One of the main non-intrusive techniques for velocity and fluid flow measurements is particle image velocimetry (PIV). Due to ongoing improvements in image hardware and processing techniques, the diversity of applications of the PIV method continues to increase. Advances in PIV techniques have led to experimental investigations of complex problems providing a foundation for development of more accurate numerical models. During the last two decades, the PIV technique has been widely used in the field of wave mechanics [1–7].

Understanding of velocities and accelerations of waves is essential for calculating forces on marine structures. For breaking waves this force is potentially much larger than for non-breaking waves. Therefore, reliable characterisation of the wave hydrodynamics particularly for breaking waves is important to improve the design of ocean and coastal structures.

A fundamental and long-standing gap in our understanding of deep-water wave breaking is how to characterise and predict the breaking onset. The kinematic breaking criterion based on surface particle and wave crest velocities is often suggested to predict the onset of breaking. The surface kinematics

associated with wave breaking has been studied using a suite of imaging techniques during the last two decades [1, 8–13]. Because measuring the surface particle velocity and the defining the crest speed are difficult, evaluation of this criterion remains nontrivial.

Banner *et al*. [14] studied deep water wave kinematics numerically, both in the laboratory and the field and have shown that the dominant waves in a group systematically slow down as they pass through the group maximum by between 10 and 30%. Barthelemy *et al*. [15] show numerically that the onset of breaking occurs once the water surface particle velocity at the wave crest exceeds a set proportion of the velocity of the slowing crest as it passes through the maximum of a wave group.

This contribution presents evaluation of a thermal image velocimetry (TIV) technique to measure the surface wave velocity using infrared imagery. Experiments were carried out in a 2D wave flume with glass side walls. Hot water droplets and a CO2 laser were used to create localised thermal signatures on the water surface, which were tracked and analysed.

2. The experiment

2.1. Experimental facilities

The experiments were conducted in the two-dimensional wind-wave tank at the Water Research Laboratory used previously by Banner and Peirson [16] (figure 1). The wave tank is 30 m long, 0.6 m wide and 0.6 m high with glass side walls and was filled with water to the depth of 0.46 m. Waves were generated using a computer-controlled, flexible bottom-cantilevered wave paddle located at one end of the flume. At the other end, a flexible reticulated polyester-urethane foam absorbent beach was installed to minimise reflections of the generated waves.

A movable wind tunnel with the length of 7.5 m and the roof of 0.5 m above the still water surface was mounted on the flume. A fan installed at the downstream of the tunnel generated wind flow and an adjustable honeycomb flow provided a uniform air flow within the wind tunnel. The wind speed was measured at the centre of the tunnel approximately 4.8 m downwind of the inlet and 0.25 m above the still water level using a pre-calibrated hot probe air velocity meter (Velocicalc model 8347).

For generating wind-forced waves, wind intensity was controlled by varying the fan input voltage using a metered Variac. Paddle-generated waves under wind forcing were investigated for different wind speeds in the range of 1.0 to 2.2 m/s.

To find the paddle amplitude corresponding to the transition between maximum (non-breaking) recurrence and marginal breaking, light was projected inside the tunnel and the transitional condition was determined visually. The paddle amplitude was increased systematically until the location of initial breaking was detected.

Two linear arrays of capacitance wave probes with 200 mm wire elements were located at each side of the flume to record the water elevation using a National Instruments PCI-6225 data acquisition system at 1000 Hz sample rate per channel. The probe resolution was 0.1 mm with a linearity of ±0.2 mm over their 200 mm length. To minimise any effect of the probes on the wind flow, the wave probe signal conditioning boxes were mounted outside the tunnel, with probes connected to the boxes via 6 mm diameter cables.

Five wave probes were installed along the one side of the tank with the spacing of 60 mm to measure the crest speed. At the other side of the tank, seven wave probes with the spacing of 100 mm were installed to measure the wave length. The water level time series captured by the wave probes were interpolated in space to obtain the zero-crossing locations at the time of the wave group maximum and, thereby, the length of the crest in the direction of propagation and crest elevation. The local steepness S_c was calculated using the length of the crest in the direction of propagation and the maximum crest elevation for each wave group.

2.2. Wave conditions

To measure the wave crest speed and water particle velocity, monochromatic and group waves were generated by the paddle. The initial conditions for generating wave packets were based on Banner and Peirson [2007].

Bimodal spectrum (Class 2) and chirped (Class 3) initial wave packets were investigated in the current study. The form of the bimodal initial spectrum was taken as:

$$\eta = a_0 \cos(k_0 x) + \varepsilon a_0 \cos\left(\frac{N+1}{N} k_0 x - \frac{\pi}{18}\right) \quad (1)$$

where η is the water surface elevation, a_0 is the initial amplitude, k_0 is the wave number, N is the number of waves in the group and ε=0.1.

The chirped wave packet was taken to have the form:

$$x_p = a - 0.25A_p\left(1 + \tanh\frac{4\omega_p t}{N\pi}\right)\left(1 - \tanh\frac{4(\omega_p t - 2N\pi)}{N\pi}\right)\sin\left(\omega_p(t - \omega_p C_{t2} t^2/2)\right) \quad (2)$$

where x_p represents the wave paddle motion, A_p is proportional to the piston amplitude, t is time, ω_p is the paddle angular frequency and C_{t2} is the chirp rate of the linear modulation.

3. TIV system

In this study, two TIV methods were used to measure the horizontal water particle velocities. The system consisted of heat sources, an infrared imaging camera, a computer-controlled shutter, an acoustic sensor, synchroniser and a computer controlling the system components.

3.1. Localised thermal signatures on the water surface

Initially a thermos flask was used to deposit hot water droplets on the water surface with low (<10) Weber number ($W = \varrho u^2 d/\sigma$), where ϱ is the droplet density, u is the mean droplet impact velocity, d is the droplet diameter and σ is the surface tension. The thermos was mounted at the centre line of the flume with two linear arrays of wave probes just inside each of the tank side walls on a trolley (figure 1a). To adjust the time interval between droplets and the dimension of the droplets, a valve and nozzle were installed on the thermos. For group waves, hot droplets were laid down upstream of the group maximum location.

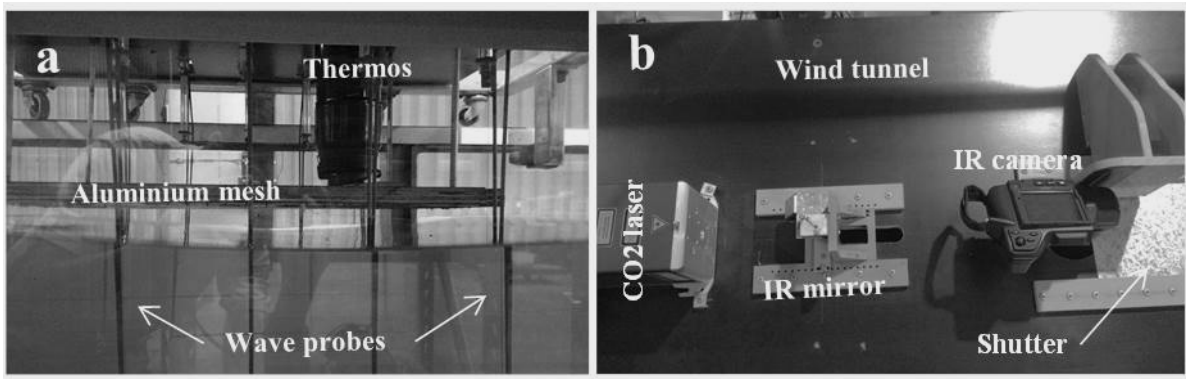

Figure 1. Laboratory deployment of instrumentation: (a) Side view showing positioning of the Thermos, wave probes and an aluminium calibration mesh installed on a trolley. (b) View from above showing the wind tunnel, CO_2 laser system, adjustable IR mirror, infrared imaging camera and computer-controlled shutter. Note that the Thermos and calibration mesh were removed once the laser system was deployed.

In order to improve the localisation of hot spot formation on the water surface, a CO_2 laser (Firestar ti100) system was developed to irradiate the water surface. The laser was mounted at the centre of the wind tunnel roof to produce heated circular patches with a diameter of approximately 4 mm upstream of the group maximum location (figure 1b).

As CO_2 lasers produce a beam of infrared light with 10.6 μm wavelength, an IR flat mirror was installed on an adjustable holder in front of the laser head to reflect the laser light on to the water surface. To minimise the diameter of the heated patches, the duty cycles were set as small as possible. The range of laser duty cycles for different wave packets was selected between 5 to 10 ms.

3.2. Infrared imaging camera

The TIV system used an infrared imaging camera (Flir T420) to acquire images of surface displacements from above, capturing 320×240 pixel images of the surface with the 25º×19º field of view at 30 frames per second (figure 1b). The physical resolution of the thermal imager was approximately 0.66 mm per pixel at the water surface, determined using calibration grids placed within the field of view.

For the TIV system using hot water, the camera was mounted on the trolley at the centre line of the tank and central to the wave probe arrays. An aluminium mesh was installed in the field of view of the camera. To adjust the level of the grids for calibrating the images, the mesh frame was connected to the trolley using four adjustable bars. In the CO_2 system, the thermal camera was mounted at the centre of the wave probe arrays on the wind tunnel roof to observe the tank water surface through a shuttered window 3.6 m downwind of the wind tunnel inlet. Because the laser reflections could potentially damage the camera's image sensor, a computer-controlled shutter was installed beneath the camera and the shutter remained closed during surface irradiation.

3.3. Synchronisation

In the TIV system, one of the wave probes was applied as a trigger to synchronise the wave signals, laser pulses and the shutter using a National Instrument PCI-6221 data acquisition system. At a selected water surface level, laser pulsing commenced with a defined duty cycle. After surface irradiation, the shutter was opened and the thermal camera monitored the motion of the heated patches on the water surface. An acoustic sensor was installed on the shutter to synchronise the shutter motion, wave probes and camera image capture. The absolute time reference between the thermal imagery and the wave probes was ±17 ms, determined by the camera framing rate.

3.4. Experiments

To validate the technique, the present experimental study was conducted to measure the water surface particle velocities and wave crest speeds for deep-water non-breaking and breaking waves with and without wind forcing. The TIV techniques were applied for monochromatic, C2N5 and C3N7 where C is the wave class and N is the number of waves in each temporal wave packet. A Class 3 wave packet (N=7) was selected to analyse under wind forcing. Before starting each experiment, the water surface was cleaned by generating waves to transport all slick material along the surface of the tank water to the beach. Once the water surface had been cleaned, the wave probes were immersed in the tank for approximately 1 hour to ensure their signal stability. To determine the conditions of maximum recurrence and marginal breaking for each group, paddle amplitudes were incrementally increased. The fetches of the group maximum were found carefully and the TIV system was sited over each location for subsequent measurement of the local wave characteristics and surface current. Initially, hot water droplets were used to generate hot spots on the water surface. As the droplets lost their thermal signatures quickly, it was necessary to deposit each droplet just before arrival of the wave crest.

Subsequently, the CO_2 laser system was synchronised to apply the heated patches to the water surface. The maximum wind speed at which traceable and sufficiently-localised heat patches could be tracked on the water surface was approximately 2.0 m/s. For wind speeds between 1.5 m/s and 2.0

m/s, hot spots rapidly expanded on the surface but they were still recognisable. Heated patches on wave crests for wind speeds higher than 2.0 m/s were not easy to track as they disappeared very quickly. Therefore, the maximum wind speed used for the present study was approximately 2.0 m/s.

4. Results and discussion

The TIV system was applied to non-breaking monochromatic and group waves. The displacement of heated patches at the crest of monochromatic and Class 3 waves are shown in figure 2. The water surface velocity was determined by tracking the leading edge of the heated patch in successive video frames and the wave crest speed was measured using the array of wave probes. The average and standard deviation from five measurements of water surface velocity (U_s), wave crest speed (C), wave amplitude (a) and wave number (k) for monochromatic waves (T = 0.7 sec) has been presented in table 1. The wave parameters were measured using the two arrays of wave probes.

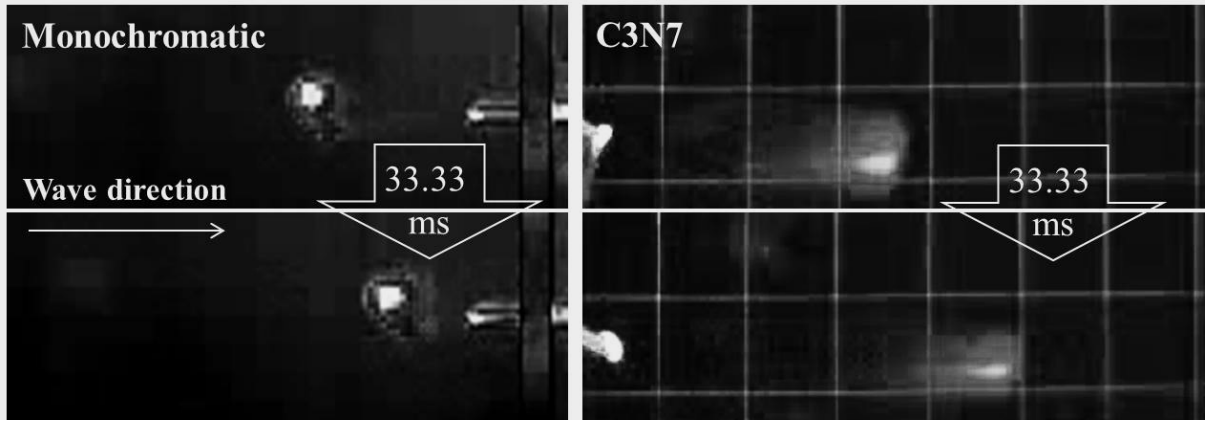

Figure 2. Tracking the hot spot on the wave crests of a monochromatic wave and a C3N7 wave packet for two successive frames using infrared imagery to measure the surface particle velocity.

The most challenging measurements required capturing crest surface velocities at the point of the group maximum. This required ensuring that the position of heat patches coincided with the crest concomitant with occurrence of the group maximum. Because the TIV method using the Thermos was not able to synchronise the droplets with the wave probes, it was not possible to have a precise measurement of the crest surface velocities for grouped waves. In addition, the experiment was conducted for breaking waves and it was found that the hot spots disappeared quickly and it was not possible to track those spots on the water surface. For wind-forced waves, the hot droplets were not trackable as they had lost their heat before reaching the water surface.

Table 1. The results of wave crest speed (C), wave amplitude (a), wave number (k), and water surface velocity (U_s) for a single case of monochromatic non-breaking waves (T = 0.7 s).

	C (m/s)	a (m)	k (m^{-1})	$a.k.C$	U_s (m/s)
Average	1.12	0.0092	7.84	0.081	0.085
Standard Deviation	0.014	0.00005	0.02	0.001	0.002

The TIV technique using the CO_2 laser improved the technique significantly for both breaking waves and wind-forced waves. Nonetheless, trial and error iteration was required to ensure that the position of heat patches coincided with a crest maximum event. The heated patches produced by the laser remained on the water surface longer than the droplets and were much more compact

(approximately 4 mm in diameter). This allowed us to measure the water surface velocities before and after a crest maximum event as well as crest surface water velocity. The movement of a single heated patch on a C3N7 breaking wave is presented in figure 3. The location of the crest maximum is at the centre of the image. The first image shows the heated patch just before the breaking onset. Images (b) and (c) present the patch 33.33 ms and 66.66 ms thereafter. By digitising the front of the patches in successive frames and having the time between each frame, the water surface velocities could be calculated.

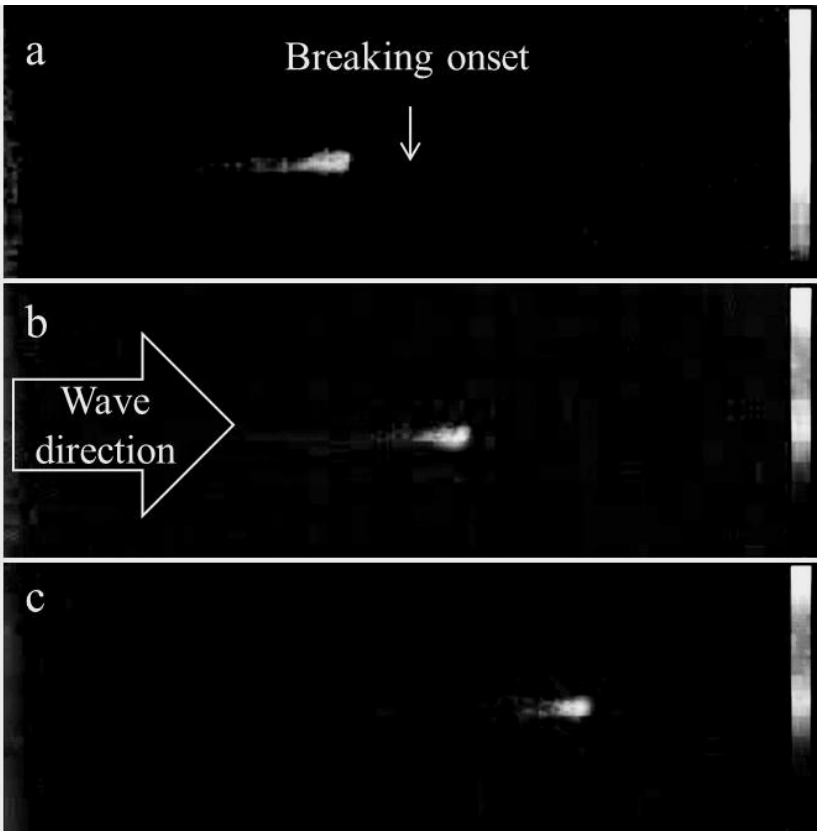

Figure 3. A heated patch generated by the CO_2 laser on a C3N7 wave packet (a) before the breaking onset, (b) and (c) on the breaking wave. The time between each frame is 33.33 ms.

After measuring the fluid velocities at the wave surface during the transit of a crest maximum event, these velocities could be interpolated in time to obtain a velocity at the crest that was immediately local in space to the crest maximum location. A polynomial curve was fitted to a sequence of such measurements (figure 4) to interpolate in space to obtain a single measurement of velocity at the crest group maximum. This entire sequence was repeated 7–10 times to quantify measurement repeatability. In each case, it was found that the water surface wave particle velocity increases to a maximum at the crest. The surface velocity for a marginal breaking C3N7 and C2N5 wave groups with the polynomial curve fitted to the velocities are illustrated in figure 4a. Distance in this figure indicates location relative to the crest maximum. As shown, the maximum water velocity occurs at a crest maximum event.

Further, the wave crest speeds were measured during transit of a crest maximum event. In contrast with surface velocity, the wave crest itself systematically slows down to a minimum speed at the crest maximum. The result of the crest speed measurement for the C3N7 wave group case shown in figure 3 and C2N5 wave groups with the polynomial curve fitted to the speeds are presented in figure 4b.

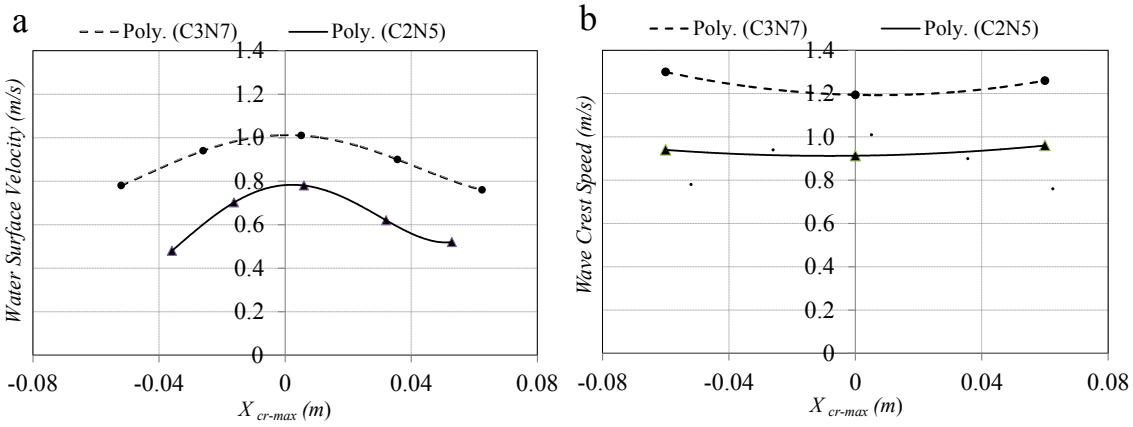

Figure 4. (a) Surface water particle velocities (m/s) and (b) wave crest speeds (m/s) in the vicinity of the crest maximum for marginal breaking C3N7 (dashed curve) and C2N5 (solid curve) wave groups. Horizontal axis is the distance relative to the location of crest maximum (m).

5. Summary and conclusions

In the present study a thermal image velocimetry technique using infrared imagery was developed to measure the water surface velocity. Heated droplets and a CO_2 laser were used to generate heated patches on the water surface. Unidirectional deep-water waves were generated in a 2D wind wave flume. Three wave types, i.e. monochromatic waves, bimodal spectrum (Class 2) and chirped wave packet (Class 3), were used for evaluation of wave breaking criteria.

It was shown that the TIV technique using heated water droplets can quantify the surface velocity for monochromatic, non-breaking waves without wind forcing.

A CO_2 laser system was developed to irradiate the water surface so as to improve the localisation of hot spot formation on the water surface. With this enhancement, the TIV technique can capture crest water velocities for unforced and wind-forced grouped waves.

These results show that the surface fluid velocity increases to a maximum at the crest maxima. At the same time, the wave profile crest speeds take on their minimum values at the crest maxima. The present results show that at the crest maximum location, the ratio of the water velocity U_s at the crest maximum to the wave profile speed C for marginal breaking waves is consistently less than unity.

References

[1] Peirson W L 1997 *Exp. Fluids* **23** 427
[2] Gray C and Greated C A 1998 *Opt. Lasers Eng.* **9** 265
[3] Siddiqui M H K *et al* 2001 *Phys. Fluids* **13** 1891
[4] Jensen A *et al* 2001 *Exp. Fluids* **30** 500
[5] Jessup A T and Phadnis K R 2005 *Meas. Sci. Technol.* **16** 1961
[6] Muste M *et al* 2005 *Flow Meas. Instru.* **16** 47
[7] Garbe C S *et al* 2007 *Transport at the Air–Sea Interface* eds Garbe C S *et al* (Heidelberg: Springer) 223-39
[8] Jessup A T *et al* 1997 *Nature* **385** 52
[9] Banner M L and Peirson W L 1998 *J. Fluid Mech.* **364** 115
[10] Zappa C J *et al* 2001 *J. Geophys. Res.* **106** 9385
[11] Stansell P and Macfarlane C 2002 *J. Phys. Oceanogr.* **32** 1269
[12] Peirson W L and Banner M L 2003 *J. Fluid Mech.* **479** 1
[13] Peirson W L *et al* 2014 *J. Fluid Mech.* **743** 399
[14] Banner M L *et al* 2014 *Phys. Rev. Lett.*, **112** 114502
[15] Barthelemy X *et al* 2015 *J. Fluid Mech.* under review
[16] Banner M L and Peirson W L 2007 *J. Fluid Mech.* **585** 93

An Experimental Investigation of Extreme Water Velocities and Deep Water Wave Breaking

A. Saket[1], W. L. Peirson[1,2], M. L. Banner[3] and X. Barthelemy[1,3]
[1] Water Research Laboratory, School of Civil & Environmental Engineering, UNSW Australia, Sydney, Australia
a.saket@wrl.unsw.edu.au, bill.peirson@wrl.unsw.edu.au, x.barthelemy@wrl.unsw.edu.au
[2] New College, UNSW Australia, Sydney, Australia
[3] School of Mathematics and Statistics, UNSW Australia, Sydney, Australia
m.banner@unsw.edu.au

Keywords: Wind waves, Wave breaking, IR imagery, Droplet kinetics.

Abstract
Wave breaking plays a crucial role in the dynamics of the upper ocean: air-sea exchanges and turbulence-wave interaction processes. Wave breaking is one of the key factors in oil slick dispersal and transport of oil droplets into upper layers of the water column. Moreover, understanding the hydrodynamics of breaking is important in improvement of the design of offshore and coastal structures. The present study describes a new experimental investigation of water surface velocity of wind waves using heat as a surface tracer. The experiment was conducted in a two dimensional wave flume and revealed the changes in the surface velocity structure which occur at the onset of wave breaking. The infrared imagery showed that materials on the water surface were subducted and surfed at the breaking front which can cause mixing or transport of buoyant particles. In addition, an accurate Thermal Image Velocimetry technique was developed to find a new parameterisation which identifies the transition from non-breaking to breaking waves. Using this technique, it was revealed that the surface wave velocity increases before the onset of breaking and has its maximum value at the crest maximum. In contrast with the surface fluid velocity, wave crests slow down as they approach their crest maximum and have their minimum speed at the crest maximum.

1. Introduction

Due to the importance of wave breaking in the dynamics of the upper ocean, air-sea mass and scalar exchange and turbulence-wave interactions, wave breaking has received increased attention in recent decades [1-4]. As water velocities and accelerations associated with breaking waves are far larger than for non-breaking waves with the same height [5], breaking wave can impose large impulsive forces on marine structures. Therefore, understanding the hydrodynamics of wave breaking plays a significant role in improvement of the design of offshore and coastal structures. In addition, velocities in steep waves are required for subsequent analysis of loads on, e.g. ships, offshore platforms, tension legs and risers [6], the description of the kinematics during steep wave events at sea is important for the offshore and ocean engineering industry.

Moreover, wave breaking is one of the key factors in oil slick dispersant and transport of oil droplets into upper layers of the water column [7]. Surface particle transport is a combination of wave [8] and wind drift [9, 10] imposed on the underlying, large-scale circulation. Breaking waves inject bubbles and turbulence into the water column and have significant impact on dispersing of oil spilled on the sea surface. The turbulence generated by breaking waves is able to mix the water surface and transport bubbles to depth [11-13]. Banner and Phillips [14] originally examined the role of the wind drift layer in the onset of deep water wave breaking. The surface kinematical behaviour of small-scale wave breaking has been studied using a suite of imaging techniques during the last two decades [10,15-19]. Particle Image Velocimetry (PIV) is a state-of-the-art non-intrusive technique for velocity and fluid flow measurements. For microscale wind-wave breaking, measurements using PIV confirm a crucial role of the transport of fluid from the surface to the turbulent domain below.

Zappa et al. [18] investigated the mechanism of microscale wave breaking using IR techniques and reported a linear correlation between the fraction of the water surface covered by microscale wave breaking and gas transfer velocity. Peirson and Banner [10] studied the intricate and complex processes which occur immediately beneath open water surfaces covered with microscale breaking waves. Their PIV observations of near-surface velocity structure showed that a wind drift velocity is approximately 28% of the wind friction velocity and the aqueous diffusion sublayer can be regularly subducted at the onset of microscale breaking. Their results were confirmed by Peirson et al. [19]. In addition, Banner et al. [20] studied deep water wave kinematics numerically, both in the laboratory and the field. They showed that each dominant wave crest approaching its maximum height slows down systematically by between 10 and 30%, reaccelerating thereafter.

In the present study, the extreme surface velocities and the impact of wave breaking on the surface of the water was investigated experimentally. The experiment was carried out in a 2D wave flume. Hot water droplets and CO2 laser system were used to heat the water surface. An accurate PIV

technique using an infrared imagery was developed to acquire visual images of water surface at the onset of wave breaking. In addition, surface wave velocity and wave crest speed at breaking onset were investigated using the Thermal Image Velocimetry.

2. Laboratory facilities

Experiments were conducted in a two dimensional wind-wave flume with glass side walls at Water Research Laboratory, UNSW Australia, Manly Vale. The flume was 30 m in length, 0.6 m in width and 0.6 m in depth filled with dam water to a depth of 0.46 m. Waves were generated using a computer controlled flexible wave paddle located on the front side of the flume. To minimise the reflections of the generated waves, a flexible polyester-urethane foam absorbent beach was installed at the far end of the tank. Capacitance wave probes mounted approximately 0.1 m from the near flume sidewalls recorded wave profiles. An infrared video camera with the frame rate of 30 Hz acquired visual images of surface motion. The laboratory facilities are shown in Figure 1.

3. Methodology

This investigation was carried out based on class 2 and class 3 wave groups, i.e. bimodal initial spectrum and chirped wave packets [21] in deep-water conditions. The water depth was 0.46 m and the angular frequency of the paddle (ω_p) was 8.18 rad.s^{-1} for the class 3 wave packets. The paddle amplitude for maximum recurrence and marginal breaking waves was determined carefully for each wave packet. Since waves have their maximum amplitude at the onset of breaking, wave data at the determined location of the marginal breaking, and also at one crest maximum before and after were recorded using two arrays of wave probes. The wave profiles were recorded using a National Instrument PCI-6225 data acquisition at 1000 Hz sample rate. By comparing the wave amplitudes, the exact location of breaking and paddle amplitude were determined for each case.

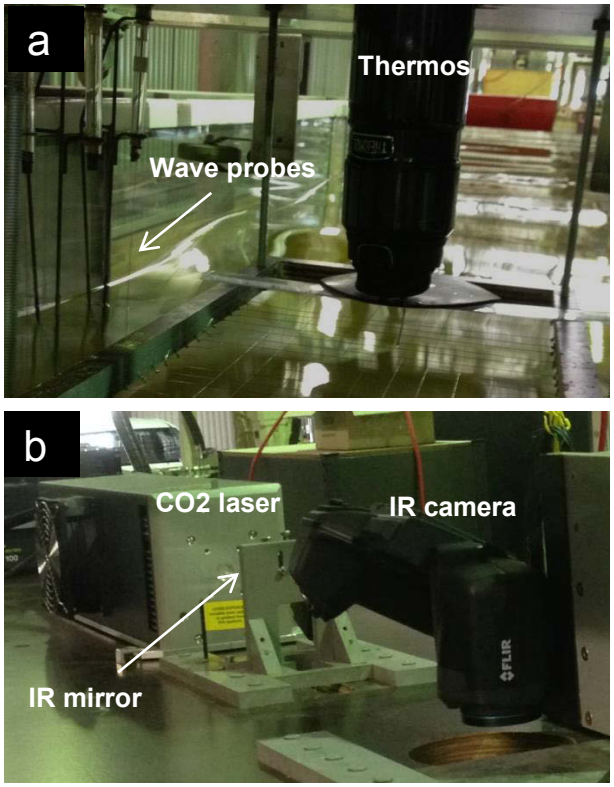

Figure 1 Laboratory deployment of instrumentation: (a) Thermos, wave probes and an aluminium mesh to calibrate camera images, and (b) CO2 laser system, adjustable IR mirror and infrared video camera looking down at the centre line of the flume and central to the wave probe array.

The infrared video camera was set up at the location of crest maximum to record the horizontal surface motion at the onset of breaking. A thermos was applied to make localised hot water spots on the waves' surface and a CO2 laser was used to produce heated circular patches on the top layer of water surface. The measurement results are discussed in section 4.

Initially for heating the area at the onset of breaking, the thermos was mounted downstream of crest maximum (Figure 1). Hot droplets with low (<10) Weber number ($W = \rho u^2 d/\sigma$) were deposited on to the water surface where ρ is the droplet density, u is the mean droplet impact velocity, d is the droplet diameter and σ is the surface tension. A valve was installed on the thermos to control the droplet flow rate and the downward-looking infrared camera recorded the impact of wave breaking on the heated surface fluid. Successive IR images were analysed during wave breaking and the rate of the disappearance of the heated area was calculated to measure the water surface subduction. In order to calibrate the images, a very thin metal mesh was placed within the field of view in the wave flume. Subsequently, a CO2 laser system was developed to irradiate the water surface. As CO2 lasers produce a beam of infrared light with 10.6 μm wavelength, the absorption depth in water for the CO2 laser is approximately 10 μm. Therefore, the total energy of the laser was not absorbed by the water and a substantial proportion of its energy was reflected from the water surface. The laser was able to make heated patches on the wave surface with a diameter less than 5 mm.

Since the laser beam reflections angle were not predictable, a shutter was installed beneath the camera to protect its lens during the irradiation process and an acoustic sensor was mounted in front of the shutter to track the shutter motion. A wave probe was used to synchronise the wave signals, laser pulses, the shutter and the sensor using a National Instrument PCI-6221 data acquisition system. At an adjustable water surface

level, the laser started to pulse on the water surface and after opening the shutter, the camera was able to track the hot spots on the water surface.
Moreover, this Thermal Image Velocimetry (TIV) technique was conducted to find the horizontal surface wave velocity before and after crest maximum to determine the maximum velocity for maximum recurrence and marginal breaking waves. In addition, wave crest velocity was measured using the array of wave probes for maximum recurrence and marginal breaking waves.

4. Results and Discussion

These techniques were applied for three different deep water wave packets i.e. C2N3, C2N5 and C3N5 where C represents the wave class and N is the number of waves in each wave packet. The impact of wave breaking on a surface heated patch for a class 2 wave packet is shown in Figure 2. This figure illustrates five successive frames of the heated area on the water surface before and after wave breaking onset. Wave direction is from left to right. In Figure 2-c, the breaking wave has reached the heated area and eliminated a part of the heat. Figure 2-d and 2-e show the impact of breaking wave on the heated patch after 33 ms and 66 ms, respectively.
The movement of a single hot patch on a second breaking wave is presented in Figure 3. The first image in the figure shows the heated patch at breaking onset. Images (b) and (c) show the patch 33 ms and 66 ms thereafter.
The observations and measurements in this experiment indicated that surface fluid was subducted predominantly beneath the breaking wave. The results of this experiment for class 2 and class 3 wave groups are presented in Table 1. In the table, the average percentage for the elimination of the heat patch due to wave breaking is presented for different cases. As the temperature of the heat patches decreased with time, in some cases there was an uncertainty for the percentage of the subduction. This uncertainty has been presented in Table 1.

Table 1 The average percentage of the subducted and surfed materials due to wave breaking for different deep water wave groups. The last column shows the proportion of those cases where distinctive subduction or surfing was not observed.

Case	Subducted %	Surfed %	Uncertain %
C2N3	65	22	13
C2N5	71	19	10
C3N5	76	16	8

The results indicated that for both wave classes, the probability of subduction at the onset of breaking is approximately 75%±10%. After subduction, the surface water was rapidly dispersed by the turbulent flow beneath the breaking crest.
As the experiment revealed, the heated patches could surf on the breaking wave and we were able to track their motion using the thermal imagery. By digitising the location of patches in successive frames and knowing the camera frame rate, the velocity at the wave surface was measurable. In the present study the surface wave velocity was measured for maximum recurrence and marginal

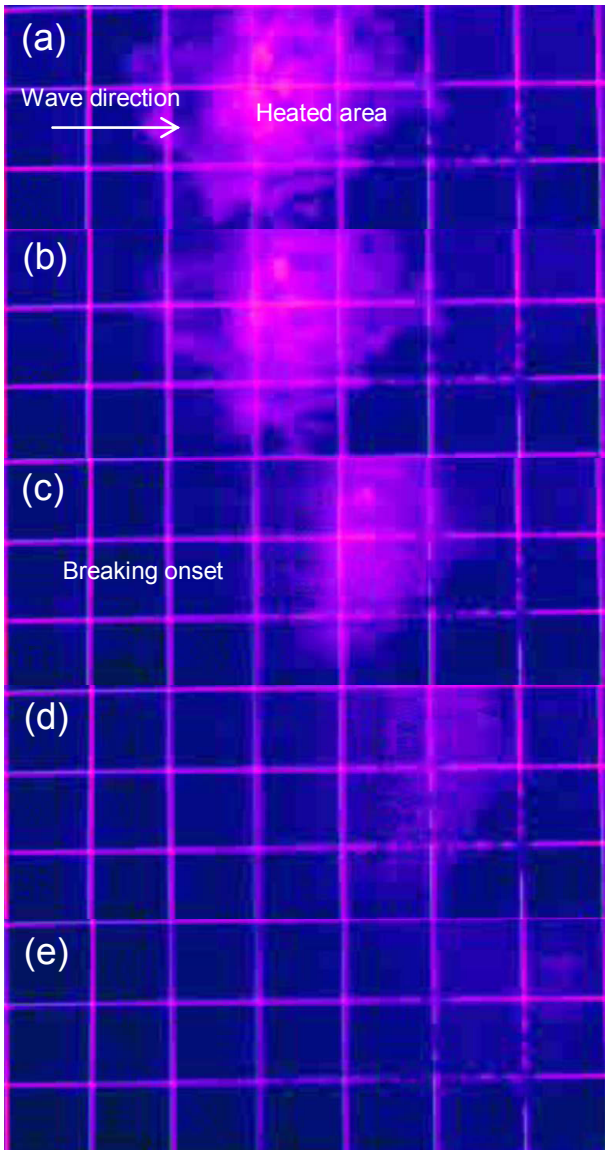

Figure 2 Tracking the surface movement by heating the area in front of the onset of breaking for a class 2 wave packet. (a) and (b) image of water surface before the onset of breaking, (c) water surface at breaking onset, (d) and (e) impact of wave breaking on the water surface 33 ms and 66 ms after breaking onset.

breaking waves. The result of this measurement for one case is shown in Figure 4. The figure illustrates the surface velocity and crest velocity before, after and at the location of crest maximum for a breaking wave. In the figure, X_{cr} is the distance of each point to the location of crest maximum and a polynomial curve was fitted to the successive velocities. The figure shows that the surface velocity is increased by reaching the crest maximum location. In addition, the maximum surface velocity is occurred at the crest maxima. In contrast with surface velocity, wave crest slows down as it approaches the crest maximum and its velocity is minimum speed at the crest maximum.

5. Summary and Conclusions

In the current study, a new experimental approach to measure water surface velocities of wind-waves using heat as a surface tracer was conducted. An infrared imaging technique was used to visualise the freely-propagating deep water waves in the laboratory. The result of this investigation showed that at the breaking onset approximately 75%±10% of surface materials beneath the breaking wave was subducted through the turbulent breaking. The remainder were observed to surf at the breaking front.

In addition, Thermal Image Velocimetry indicated that surface wave velocities speed up as they reach to the crest maximum and slow down thereafter. In contrast with surface velocity, the wave crests slow down before the crest maximum and reaccelerate after passing the crest maximum.

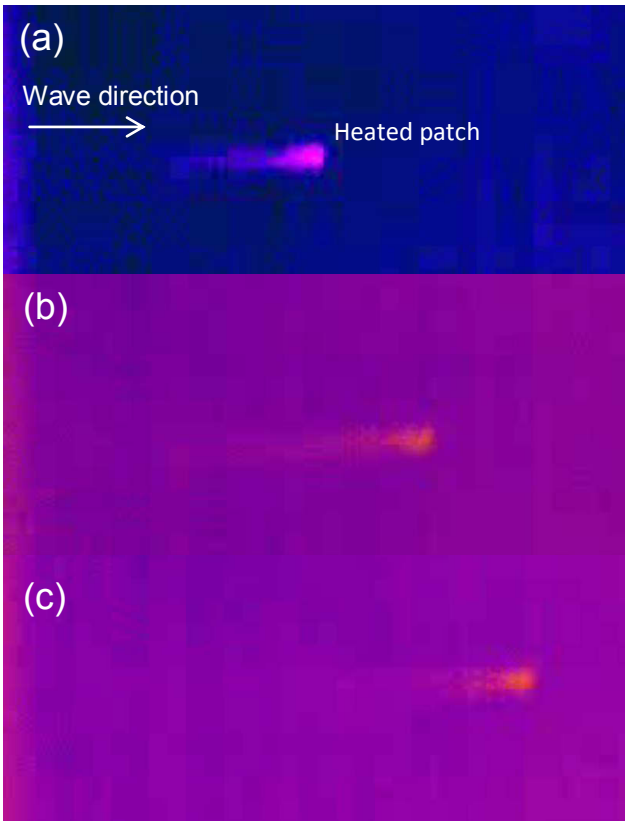

Figure 3 Tracking a single heated patch generated by the CO2 laser on the water surface in front of a class 3 wave packet. (a) The patch on the crest of the breaking wave. (b) and (c) The motion of heated patch on the breaking wave with the velocity of approximately 1.0 m/s and 0.9 m/s, 33 ms and 66 ms after the breaking onset respectively.

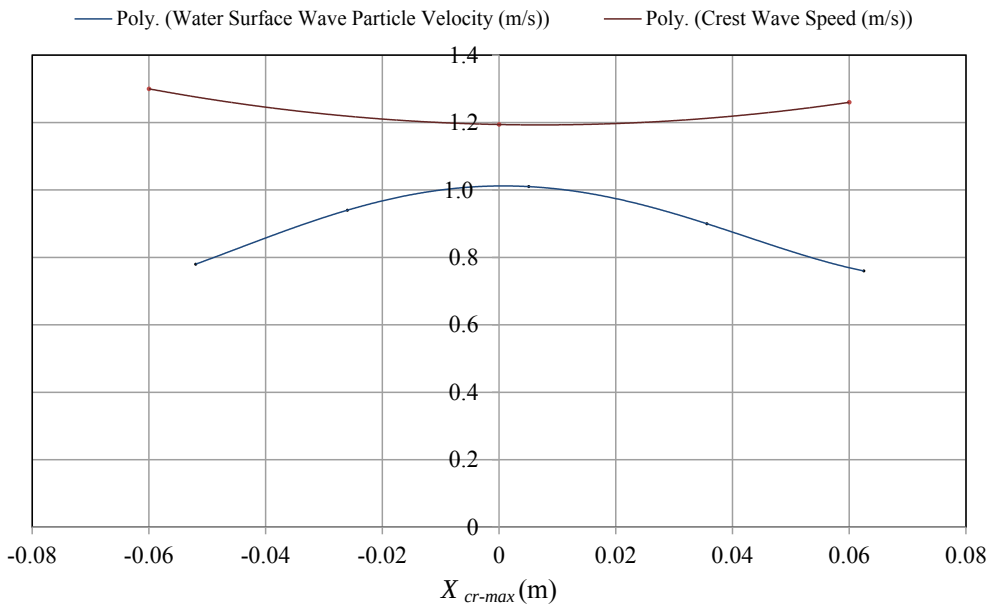

Figure 4 Surface water particle (solid curve) and wave crest (dashed curve) velocities (m/s) in the vicinity of a crest maximum for a marginal breaking wave. *Xcr* presents the distance relative to the location of the crest maximum.

6. References

[1] Banner, M. L. and Peregrine, D. H. (1993). Wave breaking in deep water. Annu. Rev. Fluid Mech, Vol. 25, pp. 373-97.

[2] Melville, W. K. (1996). The role of surface-wave breaking in air-sea interation. Annu. Rev. Fluid Mech, Vol. 28, pp. 279-21.

[3] Perlin, M. and Schultz, W. W. (2000). Capillary effects on surface waves. Annu. Rev. Fluid Mech, Vol. 32, pp. 241-74.

[4] Perlin M., Choi W. and Tian Z. (2013). Breaking waves in deep and intermediate waters Annu. Rev. Fluid Mech., Vol. 45, pp. 115-45.

[5] Melville, W. K. and Rapp, R. J. (1998). The surface velocity field in steep and breaking waves. J. Fluid Mech., Vol. 189, pp. 1-22.

[6] Grue, J. Clamond, D. Huseby, M., Jensen, A. (2003). Kinematics of extreme waves in deep water, Applied Ocean Research, Vol. 25, pp. 355-66.

[7] P. Tkalich, E.S. Chan (2002). Vertical mixing of oil droplets by breaking waves Mar. Pollut. Bull, Vol. 44, No. 11, pp. 1219-29.

[8] Phillips, O. M. (1977). The dynamics of the upper ocean. Cambridge University Press, Page 44.

[9] Phillips, O. M and Banner, M. L. (1974). Wave breaking in the presence of wind drift and swell. J. Fluid Mech., Vol. 66, part 4, pp. 625-40.

[10] Peirson, W. L. and Banner, M. L. (2003). Aqueous surface layer flows induced by microscale breaking wind waves. J. Fluid Mech., Vol. 479, pp.1-38.

[11] Boettcher, E. J., Fineberg, J., and Lathrop, D. P. (2000). Turbulence and Wave Breaking Effects on Air-Water Gas Exchange, Phys. Rev. Lett., Vol. 85, No. 9, 2030-33.

[12] Terrill, E. J., Melville, W. K., and Stramski, D. (2001). Bubble entrainment by breaking waves and their influence on optical scattering in the upper ocean, J. Geophys. Res., Vol. 106, C8, pp. 16 815-23.

[13] Melville, W. K. and Matusov, P. (2002). Distribution of breaking waves at the ocean surface, Lett. Nature, Vol. 417, pp. 58-63.

[14] Banner, M. L. and Phillips, O. M. (1974). On small scale breaking waves. J. Fluid Mech., Vol. 65, pp. 647-57.

[15] Peirson W. L. (1997). Measurement of surface velocities and shears at a wavy air-water interface using particle image velocimetry, Experiments in Fluids: experimental methods and their applications to fluid flow, Vol. 23, No. 5, pp.427-437.

[16] Jessup, A. T., Zappa, C. J. M., Loewen, R. and Hesany, V. (1997). Infrared remote sensing of breaking waves, Nature, Vol. 385 (6611), pp. 52-55.

[17] Banner, M. L. & Peirson, W. L. (1998). Tangential stress beneath wind-driven air-water interfaces. J. Fluid Mech., Vol. 364, pp. 115-145.

[18] Zappa, C. J., Asher, W. E. and Jessup, A. T. (2001). Microscale wave breaking and air-water gas transfer, Journal of Geophysical Research, Vol. 106, No. 5, pp. 9385-91.

[19] Peirson, W. L., Walker, J. W. and Banner, M. L. (2014). On the microphysical behaviour of wind-forced water surfaces and consequent re-aeration J. Fluid Mech., Vol. 743, pp. 399-447.

[20] Banner, M. L., Barthelemy, X., Fedele, F., Allis, M., Benetazzo, A., Dias, F. and Peirson, W. L. (2014). Linking reduced breaking crest speeds to unsteady nonlinear water wave group behavior. Phys. Rev. Lett., Vol. 112, No. 11, pp. 114502.

[21] Banner, M. L. & Peirson, W. L. (2007). Wave breaking onset and strength for two-dimensional deep-water wave groups. J. Fluid Mech., Vol. 585, pp. 93-115.